Compatible-strain mixed finite element methods for incompressible nonlinear elasticity

Mostafa Faghih Shojaei [a], Arash Yavari [b],*

[a] *School of Civil and Environmental Engineering, Georgia Institute of Technology, Atlanta, GA 30332, United States*
[b] *School of Civil and Environmental Engineering & The George W. Woodruff School of Mechanical Engineering, Georgia Institute of Technology, Atlanta, GA 30332, United States*

A R T I C L E   I N F O

A B S T R A C T

We introduce a new family of mixed finite elements for incompressible nonlinear elasticity – *compatible-strain mixed finite element methods* (CSFEMs). Based on a Hu–Washizu-type functional, we write a four-field mixed formulation with the displacement, the displacement gradient, the first Piola–Kirchhoff stress, and a pressure-like field as the four independent unknowns. Using the Hilbert complexes of nonlinear elasticity, which describe the kinematics and the kinetics of motion, we identify the solution spaces of the independent unknown fields. In particular, we define the displacement in H^1, the displacement gradient in $H(\mathrm{curl})$, the stress in $H(\mathrm{div})$, and the pressure field in L^2. The test spaces of the mixed formulations are chosen to be the same as the corresponding solution spaces. Next, in a conforming setting, we approximate the solution and the test spaces with some piecewise polynomial subspaces of them. Among these approximation spaces are the tensorial analogues of the Nédélec and Raviart–Thomas finite element spaces of vector fields. This approach results in *compatible-strain* mixed finite element methods that satisfy both the Hadamard compatibility condition and the continuity of traction at the discrete level independently of the refinement level of the mesh. By considering several numerical examples, we demonstrate that CSFEMs have a good performance for bending problems and for bodies with complex geometries. CSFEMs are capable of capturing very large strains and accurately approximating stress and pressure fields. Using CSFEMs, we do not observe any numerical artifacts, e.g., checkerboarding of pressure, hourglass instability, or locking in our numerical examples. Moreover, CSFEMs provide an efficient framework for modeling heterogeneous solids.

© 2018 Elsevier Inc. All rights reserved.

1. Introduction

It has been known for quite some time in the finite element literature that internal constraints, and in particular, incompressibility constraint should be treated very carefully to avoid numerical artifacts and instabilities. One path for developing efficient and robust numerical schemes for incompressible elasticity is the use of mixed finite elements.

For incompressible solids, addition of the incompressibility constraint and the pressure as an extra independent unknown results in a saddle-point problem. The well-posedness of a saddle-point problem requires that the two independent

---

* Corresponding author.
  E-mail addresses: mfsh@gatech.edu (M. Faghih Shojaei), arash.yavari@ce.gatech.edu (A. Yavari).

unknowns, which are the displacement and pressure in this context, are defined in some compatible spaces. This requirement is commonly represented by an inf-sup condition referred to as the LBB condition after the celebrated works of Ladyzhenskaya [1], Babuška [2], and Brezzi [3]. Satisfaction of this condition at the discrete level is a necessary condition for the stability of the finite element method and causes some complications for constructing the finite element spaces of displacement and pressure. There are different approaches for constructing finite elements that satisfy the LBB conditions, among which are enriching the space of displacement with some bubble functions in each element, e.g., mini element (triangular with $\mathbb{P}1 \bigoplus b3 - \mathbb{P}1$) [4], using quadratic or higher-order shape functions, e.g., quadrilateral Taylor–Hood element ($\mathbb{Q}2 - \mathbb{Q}1$) [5] or its triangular variant ($\mathbb{P}2 - \mathbb{P}1$) [6], with the proof of stability given for both by Bercovier and Pironneau [7], pairing a composite displacement element with a piecewise constant pressure element, e.g., [7], and using non-conforming displacement elements, e.g., Crouzeix and Raviart [8]. All these well-known methods are mainly developed for the Stokes saddle-point problem and the proofs of their stability are given for linear two-field mixed formulations. Although, these elements can be used for modeling incompressible linear solids, they may not perform well in nonlinear problems, especially in capturing large strains. It is shown in [9] that some of the above elements may exhibit some numerical artifacts when used in incompressible nonlinear elasticity. It is further highlighted that increasing the amplitude of the external loads and the way the incompressibility constraint is imposed may affect the performance of the above elements in nonlinear problems. As another example, see the result given in [10, §5.2] obtained by the modified quadratic displacement-linear pressure with hourglass control (CPE6MH) in ABAQUS, which shows the shortcomings of the above approaches in capturing large strains in incompressible nonlinear elasticity problems.

Over the years different approaches have been presented to avoid the difficulties associated with a saddle-point problem, among which are choosing different trial and test spaces (Petrov–Galerkin method), statically condensing out the pressure from the corresponding matrix formulations, and stabilizing the system by adding some extra terms to the mixed formulations to alter the saddle-point problem. These approaches may be implemented individually or a combination of more than one approach may be used. Another common saddle-point problem in elasticity is the stress-displacement mixed formulation associated with the Hellinger–Reissner principle, which has mostly been implemented for linear elasticity. In this method, spaces of stress and displacement must be defined carefully. Inspired by the work of Hughes et al. [11] for the Stokes problem, Franca et al. [12] developed a mixed Petrov–Galerkin finite element method for nearly incompressible linear elastic solids. The method is based on the modification of the weak formulation associated with the critical point of the Hellinger–Reissner principle by adding some additional terms to improve stability without compromising consistency. The goal in such methods is an equal-order conforming approximation of the displacement and the Cauchy stress.

For the (nearly) incompressible nonlinear elasticity problems, Simo et al. [13] proposed a kinematic splitting of the volumetric and volume-preserving parts of the deformation gradient and used it in a three-field form of the Hu–Washizu variational principle. For compressible and near incompressible nonlinear solids, Simo and Armero [14] used an additive decomposition of the displacement gradient into a compatible part and an enhanced part. For a continuum problem the enhanced part vanishes pointwise. However, they observed that at the discrete level using mixed finite elements the enhanced part does not vanish and leads to a better representation of strain. For transversely isotropic incompressible solids, Weiss et al. [15] exploited Simo et al. [13]'s idea of splitting the deformation gradient and used the deformation mapping, dilation, and pressure as independent variables in their mixed finite element formulation of incompressible transversely isotropic solids. For imposing the incompressibility constraint, they used an augmented Lagrangian method. Lamichhane [16] developed a displacement-pressure mixed finite element method for 2D nearly incompressible nonlinear elasticity. Both the trial and test spaces of displacement are discretized using linear Lagrange finite elements enriched with standard cubic bubble functions so that the inf-sup condition is satisfied. In addition, using a Petrov–Galerkin approach, the trial space of pressure is discretized by linear Lagrange finite elements, but the shape functions of the test space of pressure are obtained by assuming a biorthogonality condition between the trial and test spaces of pressure. Using this setting, one can statically condense out the pressure from the corresponding algebraic system and solve a displacement-based problem. Chi et al. [10] used polygonal finite elements to discretize a two-field mixed formulation of 2D (nearly) incompressible nonlinear elasticity. The displacements are interpolated by choosing the barycentric coordinates over each polygon as the shape functions and the values of displacements at the polygon vertices as the degrees of freedom, which results in a C^0 approximation over the entire domain. The pressure is approximated by a piecewise constant scalar over each polygon. Their numerical studies showed that the method is stable and is able to capture very large stretches.

The present work is an extension of [17] to incompressible nonlinear elasticity. We write a four-field mixed formulation of incompressible nonlinear elastostatics in terms of the displacement, the displacement gradient, the first Piola–Kirchhoff stress, and a pressure-like field by extremizing a Hu–Washizu-type functional. Comparing with [17], in this work, we use a symmetric mixed formulation, which is computationally more efficient. Eliminating the pressure and the incompressibility constraint from the four-field mixed formulation reduces it to a symmetric version of the three-field mixed formulation of compressible solids given in [17]. In addition, based on our observation of the numerical examples of both this work and [17], we have concluded that the treatment of the boundary conditions in this work improves the accuracy and robustness of the mixed FEMs and is also easier to implement. Here, we impose the displacement boundary conditions strongly and the traction boundary conditions weakly. More specifically, only the displacement boundary condition is imposed by the standard elimination approach in the system of algebraic equations; the traction boundary condition is built into the governing equations, and hence, there is no need to directly compute the degrees of freedom of stress on the boundary. Furthermore, we provide a clearer description of finite element approximations that is easier to implement and is computationally more

efficient. In this work, we prove why some of the combinations of the finite element spaces do not result in solvable mixed finite element methods, which was also observed in [17] but was not discussed in detail.

We use the Hilbert complexes of nonlinear elasticity [18,19] to identify the spaces of the independent field variables. In particular, we define the displacement in H^1, the displacement gradient in $H(\text{curl})$, and the stress in $H(\text{div})$. This setting is different from the ones that are commonly used for the mixed formulation of linear elasticity written based on the Hellinger–Reissner principle, where the Cauchy stress and the displacement are defined in a symmetric $H(\text{div})$ space and L^2, respectively, e.g., see [20,21]. Other variants of the mixed stress-displacement method for linear elasticity were introduced in [22] and [23]. In [22], the displacement is assumed in H^1 and stress in a symmetric L^2 space, while in [23] the displacement is assumed in $H(\text{curl})$ and stress is approximated by a symmetric non-conforming $H(\text{div})$ space. Although in some aspects the above-mentioned formulations are similar to our work, they cannot be used in drawing any conclusion on the convergence or stability; linear and nonlinear elasticity are quite different and the mixed formulation of the present work is based on a Hu–Washizu-type functional, which is not directly related to the Hellinger–Reissner principle. The mixed finite element methods presented in this work can be considered structure preserving in the sense that the differential complex structure of nonlinear elasticity [18] is preserved at the discrete level. In particular, in our mixed finite element methods for incompressible nonlinear elasticity both the Hadamard compatibility condition and the continuity of traction are satisfied at the discrete level independently of the refinement level of the mesh.

This paper is organized as follows. In §2, we discuss the mixed formulation that we will later use for introducing CSFEMs. In §2.1, we first discuss some preliminaries and definitions, and then review the Hilbert complexes that describe the kinematics and the kinetics of 2D nonlinear elasticity. In §2.2, we derive a four-field mixed formulation for 2D incompressible elastostatics by extremizing a Hu–Washizu-type energy functional. In §3, we discuss the finite element approximation of the four-field mixed formulation of §2.2. In §3.1, we define some reference finite elements (shape functions and degrees of freedom) for the displacement, displacement gradient, stress, and pressure. Next, we discuss some linear bijective mappings and use them to generate the finite elements of an arbitrary element from their reference counterparts. This provides the relations necessary for mapping of the shape functions. In §3.2, we define the finite element approximation spaces and use them as the trial and test spaces of the four-field mixed formulation of §2.2 to introduce CSFEMs in §3.3. The matrix formulation of CSFEMs is the subject of §3.4. In §3.5, we discuss the solvability and stability of CSFEMs for different combinations of trial and test spaces. To assess the performance of CSFEMs, we consider several numerical examples in §4. Some concluding remarks and future work are discussed in §5.

2. A mixed formulation for incompressible nonlinear elasticity

In this section, we present a four-field mixed formulation for 2D incompressible nonlinear elasticity, which we will use for our mixed finite element methods.

2.1. Preliminaries

We first tersely review some definitions and notation, and then discuss the relations between some Hilbert complexes and the kinematics and kinetics of motion in nonlinear elasticity. Next based on these relationships, we define the spaces of definition of displacement, displacement gradient, stress, and pressure, the four field variables that we use in our mixed formulations.

Let $\mathbf{X} = (\mathrm{X}^1, \mathrm{X}^2) \in \mathbb{R}^2$ be the position of a particle in the reference configuration $\mathcal{B}$, where $\mathcal{B} \subset \mathbb{R}^2$ is a bounded domain with boundary $\partial\mathcal{B}$. For any vector field $\boldsymbol{U}$ and any $\binom{2}{0}$-tensor field $\boldsymbol{T}$ on $\mathcal{B}$, we define the following four operators:

$$
\begin{aligned}
(\mathbf{grad}(\boldsymbol{U}))^{IJ} &:= \partial U^I / \partial \mathrm{X}^J, \\
(\mathbf{div}(\boldsymbol{T}))^I &:= \partial T^{IJ} / \partial \mathrm{X}^J, \\
(\mathbf{c}(\boldsymbol{T}))^I &:= \partial T^{I2} / \partial \mathrm{X}^1 - T^{I1} / \partial \mathrm{X}^2, \\
(\mathbf{s}(\boldsymbol{U}))^{IJ} &:= (\partial U^I / \partial \mathrm{X}^2) \delta^{1J} - (\partial U^I / \partial \mathrm{X}^1) \delta^{2J},
\end{aligned}
\tag{2.1}
$$

where δ^{IJ} is the Kronecker delta, and we use the summation convention on repeated indices. Note that $\mathbf{c}$ is also known as the 2D curl operator. Let $L^2(\mathcal{B})$, $L^2(T\mathcal{B})$, and $L^2(\otimes^2 T\mathcal{B})$ be the spaces of square integrable scalar fields, vector fields, and $\binom{2}{0}$-tensor fields on $\mathcal{B}$, respectively. Consider the following spaces:

$$
\begin{aligned}
H^1(T\mathcal{B}) &:= \left\{ \boldsymbol{U} \in L^2(T\mathcal{B}) : \partial U^I / \partial \mathrm{X}^J \in L^2(\mathcal{B}),\ I, J = 1, 2 \right\}, \\
H^{\mathbf{c}}(\mathcal{B}) &:= \left\{ \boldsymbol{T} \in L^2(\otimes^2 T\mathcal{B}) : (\mathbf{c}(\boldsymbol{T}))^I \in L^2(\mathcal{B}),\ I = 1, 2 \right\}, \\
H^{\mathbf{d}}(\mathcal{B}) &:= \left\{ \boldsymbol{T} \in L^2(\otimes^2 T\mathcal{B}) : (\mathbf{div}(\boldsymbol{T}))^I \in L^2(\mathcal{B}),\ I = 1, 2 \right\}.
\end{aligned}
$$

In general, H^1 is a subset of both $H^{\mathbf{c}}$ and $H^{\mathbf{d}}$. Note that the partial derivatives and operators in the above spaces are defined in the distributional sense (weak sense). For any distribution f one extends the notion of derivative to a linear

mapping $\frac{\partial f}{\partial X^I} : \mathcal{D}(\mathcal{B}) \ni \phi \longmapsto \int_{\mathcal{B}} \frac{\partial f}{\partial X^I} \phi \, dA = -\int_{\mathcal{B}} f \frac{\partial \phi}{\partial X^I} \, dA \in \mathbb{R}$, where $\mathcal{D}(\mathcal{B})$ is the vector space of smooth functions with compact support in $\mathcal{B}$. In the same context, we similarly extend the operators defined in (2.1), e.g., the distributional (or weak) divergence is defined as $\int_{\mathcal{B}} \mathbf{div}\, \mathbf{v}\, \phi \, dA = -\int_{\mathcal{B}} \langle \mathbf{v}, \mathbf{grad}\, \phi \rangle \, dA$, where $\langle , \rangle$ is the standard inner product in $\mathbb{R}^2$.

For any vector field $\mathbf{V}$ in $H^1(T\mathcal{B})$, one can show that

$$\mathbf{c}(\mathbf{grad}(\mathbf{V})) = \mathbf{0} \quad \text{and} \quad \mathbf{div}(\mathbf{s}(\mathbf{V})) = \mathbf{0}. \tag{2.2}$$

Owing to the above relations and the definition of the above spaces, one can extend the linear operators of (2.1) to the following mappings:

$$\mathbf{grad} : H^1(T\mathcal{B}) \to H^{\mathbf{c}}(\mathcal{B}), \qquad \mathbf{c} : H^{\mathbf{c}}(\mathcal{B}) \to L^2(T\mathcal{B}),$$
$$\mathbf{s} : H^1(T\mathcal{B}) \to H^{\mathbf{d}}(\mathcal{B}), \quad \mathbf{div} : H^{\mathbf{d}}(\mathcal{B}) \to L^2(T\mathcal{B}). \tag{2.3}$$

One can concisely rewrite (2.2) and (2.3) using the following Hilbert complexes [18,19]:

$$0 \longrightarrow H^1(T\mathcal{B}) \xrightarrow{\mathbf{grad}} H^{\mathbf{c}}(\mathcal{B}) \xrightarrow{\mathbf{c}} L^2(T\mathcal{B}) \longrightarrow 0, \tag{2.4a}$$

$$0 \longrightarrow H^1(T\mathcal{B}) \xrightarrow{\mathbf{s}} H^{\mathbf{c}}(\mathcal{B}) \xrightarrow{-\mathbf{div}} L^2(T\mathcal{B}) \longrightarrow 0, \tag{2.4b}$$

where the first arrows on the left are trivial operators, which send zero to zero, and the last arrows on the right indicate the zero operator, which maps the L^2-space to zero. We use $-\mathbf{div}$ instead of $\mathbf{div}$ in the second complex, so that (2.4b) is the dual complex of (2.4a).

Let $\mathbf{U}$, $\mathbf{K}$, and $\mathbf{P}$ be the displacement vector, the displacement gradient tensor, and the first Piola–Kirchhoff stress tensor, respectively. We choose these fields to be the primary variables in our description of nonlinear elasticity. This mixed formulation allows one to impose compatibility of displacement gradient and to accurately compute stresses by approximating them in some proper spaces that are given in (2.4). Note that both $\mathbf{K}$ and $\mathbf{P}$ are two-point tensors, and hence, it does not even make sense to ask if they are symmetric. Therefore, the difficulties associated with imposing the symmetry of a tensor in finite element approximation will not be encountered. See [20,21] for the symmetry imposing issues encountered in finite element approximation of linear elasticity.

Given a motion of $\mathcal{B}$ in 2D, for the displacement field $\mathbf{U}(\mathbf{X}) := \varphi(\mathbf{X}) - \mathbf{X}$ at $\mathbf{X} \in \mathcal{B}$, one has $\mathbf{K} = \mathbf{grad}\, \mathbf{U}$, and $\mathbf{c}(\mathbf{K}) = \mathbf{0}$ is a necessary condition for the compatibility of $\mathbf{K}$. Therefore, $\mathbf{U}$ belongs to the domain of the operator $\mathbf{grad}$ and $\mathbf{K}$ belongs to the kernel of the operator $\mathbf{c}$. According to the Hilbert complex (2.4a), this is the case whenever $\mathbf{U} \in H^1(T\mathcal{B})$ and $\mathbf{K} \in \ker(\mathbf{c}) \subset H^{\mathbf{c}}(\mathcal{B})$. Moreover, in the absence of body force, the static equilibrium equation $\mathbf{div}\, \mathbf{P} = \mathbf{0}$ is the necessary condition for the existence of a stress function $\mathbf{\Psi}$ such that $\mathbf{P} = \mathbf{s}(\mathbf{\Psi})$. Therefore, $\mathbf{P}$ belongs to the kernel of the operator $\mathbf{div}$, which gives $\mathbf{P} \in \ker(\mathbf{d}) \subset H^{\mathbf{d}}(\mathcal{B})$, based on (2.4b). Note that the Hilbert complex (2.4a) is related to the kinematics of motion, while the Hilbert complex (2.4b) is related to the kinetics of motion.

Note that the deformation gradient is written as $\mathbf{F} = \mathbf{I} + \mathbf{K}$, where $\mathbf{I}$ is the identity tensor, and $J = \det \mathbf{F}$ relates the volume elements of the undeformed and deformed configurations as $dv = J dV$. For incompressible solids, we need to consider a pressure-like variable p as one more primary field variable, which acts as a Lagrange multiplier to weakly impose the incompressibility condition $J = 1$. In a discrete setting, J assigns a scalar to each element, and hence, it is natural to assume that the discrete p is defined on each element as well and has no interelement continuity. In general, pressure is a discontinuous scalar-valued field, and thus $p \in L^2(\mathcal{B})$.

2.2. A four-field mixed formulation for incompressible nonlinear elasticity

Assume that the mass density of the body $\mathcal{B}$ is ρ_0 and let $\mathbf{B}$ be the body force per unit mass. For the sake of simplicity, we assume that $\partial \mathcal{B}$ is a disjoint union of subsets Γ_d and Γ_t such that the boundary displacement $\overline{\mathbf{U}}$ is imposed on Γ_d and the boundary traction $\overline{\mathbf{T}}$ is imposed on Γ_t. Let $\mathbf{N}$ be the unit outward normal vector field of $\partial \mathcal{B}$ in the reference configuration. We consider a formulation of nonlinear elasticity in which displacement $\mathbf{U} \in H^1(T\mathcal{B})$, displacement gradient $\mathbf{K} \in H^{\mathbf{c}}(\mathcal{B})$, and the first Piola–Kirchhoff stress $\mathbf{P} \in H^{\mathbf{d}}(\mathcal{B})$ are the primary variables. We build the displacement boundary condition $\mathbf{U}\big|_{\Gamma_d} = \overline{\mathbf{U}}$ directly into the space of definition of $\mathbf{U}$, and define

$$H^1(T\mathcal{B}, \Gamma_d, \overline{\mathbf{U}}) := \left\{ \mathbf{U} \in H^1(T\mathcal{B}) : \mathbf{U}|_{\Gamma_d} = \overline{\mathbf{U}} \right\} \quad \text{and} \quad H^1(T\mathcal{B}, \Gamma_d) := H^1(T\mathcal{B}, \Gamma_d, \mathbf{0}),$$

where $\overline{\mathbf{U}}$ is of $H^{1/2}$-class. Now, we set $\mathbf{U} \in H^1(T\mathcal{B}, \Gamma_d, \overline{\mathbf{U}})$, $\mathbf{K} \in H^{\mathbf{c}}(\mathcal{B})$, and $\mathbf{P} \in H^{\mathbf{d}}(\mathcal{B})$ and define a Hu–Washizu functional. The traction boundary condition $(\mathbf{PN})\big|_{\Gamma_t} = \overline{\mathbf{T}}$ will be built into the functional. Let $\langle , \rangle$ be the standard inner product of $\mathbb{R}^2$. Also, suppose $\langle\langle , \rangle\rangle$ denotes the L^2-inner products of scalar, vector, and tensor fields, which are defined as $\langle\langle f, g \rangle\rangle := \int_{\mathcal{B}} f g \, dA$, $\langle\langle \mathbf{Y}, \mathbf{Z} \rangle\rangle := \int_{\mathcal{B}} Y^I Z^I dA$, and $\langle\langle \mathbf{S}, \mathbf{T} \rangle\rangle := \int_{\mathcal{B}} S^{IJ} T^{IJ} dA$, respectively. Let $\mathcal{D} := H^1(T\mathcal{B}, \Gamma_d, \overline{\mathbf{U}}) \times H^{\mathbf{c}}(\mathcal{B}) \times H^{\mathbf{d}}(\mathcal{B})$ and define a Hu–Washizu-type functional $\mathcal{I} : \mathcal{D} \to \mathbb{R}$ as

$$\mathcal{I}(\mathbf{U}, \mathbf{K}, \mathbf{P}) = \int_{\mathcal{B}} W(\mathbf{X}, \mathbf{K}) dA - \langle\langle \mathbf{P}, \mathbf{K} - \mathbf{grad}\, \mathbf{U} \rangle\rangle - \langle\langle \rho_0 \mathbf{B}, \mathbf{U} \rangle\rangle - \int_{\Gamma_t} \langle \overline{\mathbf{T}}, \mathbf{U} \rangle ds, \tag{2.5}$$

where $W(\mathbf{X}, \mathbf{K})$ is the stored energy function of a hyperelastic material. In 2D, the energy function of an isotropic solid has the form $W = \widehat{W}(\mathbf{X}, I_1, I_2)$, where $I_1 = \operatorname{tr} \mathbf{C}$ and $I_2 = \det \mathbf{C}$ are the invariants of the right Cauchy–Green deformation tensor $\mathbf{C} = \mathbf{F}^\mathsf{T} \mathbf{F}$. Our formulation is not restricted to isotropic solids, however, in all our numerical examples we assume isotropic solids. Note that $J = \sqrt{I_2}$. If the material is incompressible, there is no volume change, i.e., $J = 1$. Accordingly, we modify (2.5) by defining

$$\overline{\mathcal{I}}(\mathbf{U}, \mathbf{K}, \mathbf{P}, p) = \mathcal{I}(\mathbf{U}, \mathbf{K}, \mathbf{P})\Big|_{J(\mathbf{K})=1} + \int_{\mathcal{B}} p\, C\big(J(\mathbf{K})\big) dA, \tag{2.6}$$

where $p \in L^2(\mathcal{B})$ is a pressure-like scalar field that acts as a Lagrange multiplier in (2.6), to which we may refer simply as pressure, and $C : \mathbb{R}^+ \to \mathbb{R}$ is a smooth function such that $C(J) = 0$ if and only if $J = 1$. Two examples that have been used in the literature are $C(J) = J - 1$, and $C(J) = \ln J$.

Remark 1. One may define a pseudo energy function $\overline{W}(\mathbf{X}, \mathbf{K}, p) := \widehat{W}(\mathbf{X}, I_1, I_2)\big|_{I_2=1} + p\, C(J)$, and replace W in (2.5) with $\overline{W}$ to obtain the same $\overline{\mathcal{I}}$ in (2.6).

Remark 2. One may be tempted to think that an incompressible nonlinear elasticity problem can be numerically solved using a scheme for compressible nonlinear elasticity. This is not the case; a general constitutive equation for incompressible elasticity cannot be recovered from any compressible constitutive equation when some parameter(s) becomes larger and larger (or smaller and smaller). Instead, one must enforce the constraint $J = 1$ and this requires introducing a pressure field p.

To find the critical points of $\overline{\mathcal{I}}$ we proceed as follows. Let $(\mathbf{U} + \epsilon_1 \mathbf{\Upsilon}, \mathbf{K} + \epsilon_2 \boldsymbol{\kappa}, \mathbf{P} + \epsilon_3 \boldsymbol{\pi}, p + \epsilon_4 q) \in \mathcal{D} \times L^2(\mathcal{B})$ such that $(\mathbf{U}, \mathbf{K}, \mathbf{P}, p) \in \mathcal{D} \times L^2(\mathcal{B})$, $\epsilon_i \in \mathbb{R}$ for $i = 1, ..., 4$, and $(\mathbf{\Upsilon}, \boldsymbol{\kappa}, \boldsymbol{\pi}, q) \in H^1(T\mathcal{B}, \Gamma_d) \times H^\mathbf{c}(\mathcal{B}) \times H^\mathbf{d}(\mathcal{B}) \times L^2(\mathcal{B})$ are arbitrary. Next, define

$$\widehat{\mathcal{I}}(\epsilon_1, \epsilon_2, \epsilon_3, \epsilon_4) := \overline{\mathcal{I}}(\mathbf{U} + \epsilon_1 \mathbf{\Upsilon}, \mathbf{K} + \epsilon_2 \boldsymbol{\kappa}, \mathbf{P} + \epsilon_3 \boldsymbol{\pi}, p + \epsilon_4 q). \tag{2.7}$$

Note that

$$\frac{\partial}{\partial \epsilon_2} \int_{\mathcal{B}} \widetilde{W}\big(\mathbf{X}, I_1(\mathbf{K} + \epsilon_2 \boldsymbol{\kappa})\big) dA \Big|_{\epsilon_2 = 0} = \langle\!\langle \widetilde{\mathbf{P}}(\mathbf{K}), \boldsymbol{\kappa} \rangle\!\rangle, \qquad \frac{\partial}{\partial \epsilon_2} \int_{\mathcal{B}} p\, C\big(J(\mathbf{K} + \epsilon_2 \boldsymbol{\kappa})\big) dA \Big|_{\epsilon_2 = 0} = \langle\!\langle p\, \mathbf{Q}(\mathbf{K}), \boldsymbol{\kappa} \rangle\!\rangle,$$

where $\widetilde{W} = \widehat{W}(\mathbf{X}, I_1, I_2)\big|_{I_2=1}$, $\widetilde{\mathbf{P}}(\mathbf{K}) = \partial \widetilde{W} / \partial \mathbf{K}$ is the constitutive part of the stress, and $\mathbf{Q}(\mathbf{K}) = \partial C / \partial \mathbf{K} = C'(J)(\mathbf{F}^{-1})^\mathsf{T}$ comes from enforcing the incompressibility condition $J = 1$. Extremizing the Hu–Washizu functional requires that

$$\left(\frac{\partial \widehat{\mathcal{I}}}{\partial \epsilon_1}, \frac{\partial \widehat{\mathcal{I}}}{\partial \epsilon_2}, \frac{\partial \widehat{\mathcal{I}}}{\partial \epsilon_3}, \frac{\partial \widehat{\mathcal{I}}}{\partial \epsilon_4} \right)\Bigg|_{\epsilon_i = 0} = (0, 0, 0, 0).$$

The result is the following weak formulation of the boundary-value problem for incompressible nonlinear elastostatics:

Given a body force $\mathbf{B}$ of L^2-class, a boundary displacement $\overline{\mathbf{U}}$ on Γ_d of $H^{1/2}$-class, and a boundary traction $\overline{\mathbf{T}}$ on Γ_t of L^2-class, find $(\mathbf{U}, \mathbf{K}, \mathbf{P}, p) \in H^1(T\mathcal{B}, \Gamma_d, \overline{\mathbf{U}}) \times H^\mathbf{c}(\mathcal{B}) \times H^\mathbf{d}(\mathcal{B}) \times L^2(\mathcal{B})$ such that

$$\langle\!\langle \mathbf{P}, \mathbf{grad}\, \mathbf{\Upsilon} \rangle\!\rangle = \langle\!\langle \rho_0 \mathbf{B}, \mathbf{\Upsilon} \rangle\!\rangle + \int_{\Gamma_t} \langle \overline{\mathbf{T}}, \mathbf{\Upsilon} \rangle ds, \quad \forall \mathbf{\Upsilon} \in H^1(T\mathcal{B}, \Gamma_d),$$

$$\langle\!\langle \widetilde{\mathbf{P}}(\mathbf{K}), \boldsymbol{\kappa} \rangle\!\rangle - \langle\!\langle \mathbf{P}, \boldsymbol{\kappa} \rangle\!\rangle + \langle\!\langle p\, \mathbf{Q}(\mathbf{K}), \boldsymbol{\kappa} \rangle\!\rangle = 0, \qquad \forall \boldsymbol{\kappa} \in H^\mathbf{c}(\mathcal{B}), \tag{2.8}$$

$$\langle\!\langle \mathbf{grad}\, \mathbf{U}, \boldsymbol{\pi} \rangle\!\rangle - \langle\!\langle \mathbf{K}, \boldsymbol{\pi} \rangle\!\rangle = 0, \qquad \forall \boldsymbol{\pi} \in H^\mathbf{d}(\mathcal{B}),$$

$$\langle\!\langle C(J), q \rangle\!\rangle = 0, \qquad \forall q \in L^2(\mathcal{B}).$$

Note that the solution of the above problem is the critical point of the Hu–Washizu-type functional (2.6). In (2.8), the displacement (essential) boundary condition $\mathbf{U}\big|_{\Gamma_d} = \overline{\mathbf{U}}$ is imposed strongly in the solution space $H^1(T\mathcal{B}, \Gamma_d, \overline{\mathbf{U}})$ while the traction (natural) boundary condition $(\mathbf{PN})\big|_{\Gamma_t} = \overline{\mathbf{T}}$ is imposed weakly in (2.8)$_1$.

Remark 3. It is possible to reduce the size of the solution and the test spaces by considering an extra boundary condition $(\mathbf{KT})\big|_{\Gamma_d} = (\mathbf{grad}\, \overline{\mathbf{U}})\mathbf{T}$, where $\mathbf{T}$ is the unit tangent vector field of $\partial \mathcal{B}$ in the reference configuration. Then, we define $H^\mathbf{c}(\mathcal{B}, \Gamma_d, \overline{\mathbf{U}}) := \left\{ \mathbf{K} \in H^\mathbf{c}(\mathcal{B}) : (\mathbf{KT})\big|_{\Gamma_d} = (\mathbf{grad}\, \overline{\mathbf{U}})\mathbf{T} \right\}$ and $H^\mathbf{c}(\mathcal{B}, \Gamma_d) := H^\mathbf{c}(\mathcal{B}, \Gamma_d, \mathbf{0})$, and seek the solution $(\mathbf{U}, \mathbf{K}, \mathbf{P}, p) \in$

$H^1(T\mathcal{B}, \Gamma_d, \overline{\boldsymbol{U}}) \times H^{\mathbf{c}}(\mathcal{B}, \Gamma_d, \overline{\boldsymbol{U}}) \times H^{\mathbf{d}}(\mathcal{B}) \times L^2(\mathcal{B})$ with arbitrary $(\boldsymbol{\Upsilon}, \boldsymbol{\kappa}, \boldsymbol{\pi}, q) \in H^1(T\mathcal{B}, \Gamma_d) \times H^{\mathbf{c}}(\mathcal{B}, \Gamma_d) \times H^{\mathbf{d}}(\mathcal{B}) \times L^2(\mathcal{B})$. This results in a slightly smaller discrete system. We have observed in our numerical examples that this approach may improve the stability of the method at very large strains.

Remark 4. The weak formulation (2.8) corresponds to a saddle point of the Hu–Washizu-type functional (2.6). To see this, one needs to calculate the 4×4 matrix $\boldsymbol{H} = \left[\frac{\partial^2 \widehat{\mathcal{I}}}{\partial \epsilon_i \partial \epsilon_j} \right]$ at $\epsilon_i, \epsilon_j = 0$. It is straightforward to show that $\boldsymbol{H}$ is symmetric and has a non-negative determinant. Also, if $\boldsymbol{H}$ is invertible, it has two positive and two negative eigenvalues.

Green's formula allows one to write

$$\langle\!\langle \mathbf{div}\boldsymbol{P}, \boldsymbol{\Upsilon} \rangle\!\rangle = -\langle\!\langle \boldsymbol{P}, \mathbf{grad}\,\boldsymbol{\Upsilon} \rangle\!\rangle + \int_{\partial\mathcal{B}} \langle \boldsymbol{P}\boldsymbol{N}, \boldsymbol{\Upsilon} \rangle ds, \quad \forall \boldsymbol{\Upsilon} \in H^1(T\mathcal{B}, \Gamma_d). \tag{2.9}$$

We assume the following weak statement of the traction boundary condition:

$$\int_{\partial\mathcal{B}} \langle \boldsymbol{P}\boldsymbol{N}, \boldsymbol{\Upsilon} \rangle ds = \int_{\Gamma_t} \langle \overline{\boldsymbol{T}}, \boldsymbol{\Upsilon} \rangle ds, \quad \forall \boldsymbol{\Upsilon} \in H^1(T\mathcal{B}, \Gamma_d). \tag{2.10}$$

Then, it is straightforward to show that (2.8) results in the following set of governing equations for incompressible nonlinear elastostatics:

$$
\left.
\begin{array}{lll}
\text{(a)} & \mathbf{div}\boldsymbol{P} + \rho_0 \boldsymbol{B} = \boldsymbol{0}, & \\
\text{(b)} & \boldsymbol{P} = \widetilde{\boldsymbol{P}}(\boldsymbol{K}) + p\,\boldsymbol{Q}\,(\boldsymbol{K}), & \\
\text{(c)} & \boldsymbol{K} = \mathbf{grad}\,\boldsymbol{U}, & \\
\text{(d)} & J = 1, &
\end{array}
\right\} \quad \text{on } \mathcal{B},
\tag{2.11}
$$
$$
\begin{array}{lll}
\text{(e)} & \boldsymbol{U} = \overline{\boldsymbol{U}}, & \text{on } \Gamma_d, \\
\text{(f)} & \boldsymbol{P}\boldsymbol{N} = \overline{\boldsymbol{T}}, & \text{on } \Gamma_t.
\end{array}
$$

Conversely, one can show that (2.11) results in (2.8), see [17, §2.2]. Note that (2.11b) is the constitutive equation of an incompressible solid. In the current configuration it reads $\boldsymbol{\sigma} = \widetilde{\boldsymbol{P}}(\boldsymbol{K})\boldsymbol{F}^{\mathsf{T}} + \bar{p}\boldsymbol{I}$, where $\bar{p} = p\,C'(J)$ and $\boldsymbol{\sigma}$ is the Cauchy stress tensor.

Remark 5. For a neo-Hookean solid with $\widetilde{W} = \frac{\mu}{2}(I_1 - 2)$, where μ is the shear modulus at the ground state, one has the constitutive equation $\boldsymbol{P} = \mu\boldsymbol{F} + pC'(J)(\boldsymbol{F}^{-1})^{\mathsf{T}}$. In the absence of residual stresses, the body is stress free when there are no external forces. Hence, if $\boldsymbol{F} = \boldsymbol{I}$, then $\boldsymbol{P} = \boldsymbol{0}$. This gives us $(\mu + pC'(1))\boldsymbol{I} = \boldsymbol{0}$, which implies that $p = -\mu/C'(1)$ in the absence of external forces. Therefore, one should be careful to choose C such that $C'(1) \neq 0$. Also, the choice of the function $C(J)$ may affect the solution of the discrete system and may cause numerical instabilities at large deformations [9]. Our numerical examples indicate that our mixed FEMs work well with both $C(J) = J - 1$ and $C(J) = \ln J$.

Remark 6. Assume that the reference configuration of the body $\mathcal{B}$ is a non-simply-connected domain. More specifically, it is a connected 2D domain that contains n_h holes. In this setting, $\mathbf{c}(\boldsymbol{K}) = \boldsymbol{0}$ is necessary for the compatibility of $\boldsymbol{K}$ but is not sufficient; in addition to $\mathbf{c}(\boldsymbol{K}) = \boldsymbol{0}$ the following auxiliary compatibility equations must hold [24]:

$$\int_{\partial\mathcal{H}_i} \boldsymbol{K}\boldsymbol{T}_{\partial\mathcal{H}_i} ds = \boldsymbol{0}, \quad \text{for } i = 1, 2, ..., n_h, \tag{2.12}$$

where $\partial\mathcal{H}_i$ is the boundary of the i-th hole and $\boldsymbol{T}_{\partial\mathcal{H}_i}$ denotes the unit tangent vector field of $\partial\mathcal{H}_i$ in the reference configuration. Note that $\partial\mathcal{H}_i$ is chosen for convenience; the above integral for each hole can be taken over an arbitrary closed-path within the domain that encloses only that hole, i.e., any closed path that is homologous to $\partial\mathcal{H}_i$ [24]. Note that in our mixed formulation we weakly impose $\boldsymbol{K} = \mathbf{grad}\,\boldsymbol{U}$, and hence, one does not need to impose compatibility.

3. Finite element approximations

3.1. Finite elements

Following [25], we define a finite element as a triplet $(\mathcal{T}, \mathcal{P}(\mathcal{T}), \Sigma)$, where $\mathcal{T}$ is a triangle in $\mathbb{R}^2$, $\mathcal{P}(\mathcal{T})$ is a space of polynomials on $\mathcal{T}$, and Σ is a set of linear functionals $\{\sigma_1, \sigma_2, ..., \sigma_{n_s}\}$ acting on the members of $\mathcal{P}(\mathcal{T})$ such that $\forall p \in \mathcal{P}(\mathcal{T})$, $\sigma_i(p) \in \mathbb{R}$, and the liner mapping $p \longmapsto (\sigma_1(p), \sigma_2(p), ..., \sigma_{n_s}(p)) \in \mathbb{R}^{n_s}$ is a bijection. Equivalently, there exists a unique basis $\{\theta_1, \theta_2, ..., \theta_{n_s}\}$ in $\mathcal{P}(\mathcal{T})$ such that $\sigma_i(\theta_j) = \delta_{ij}$, $i, j = 1, 2, ..., n_s$. σ_i's and θ_i's are called the local degrees of freedom (DOF) and the local shape functions, respectively. Following [26], in the definition of a finite element, we always implicitly
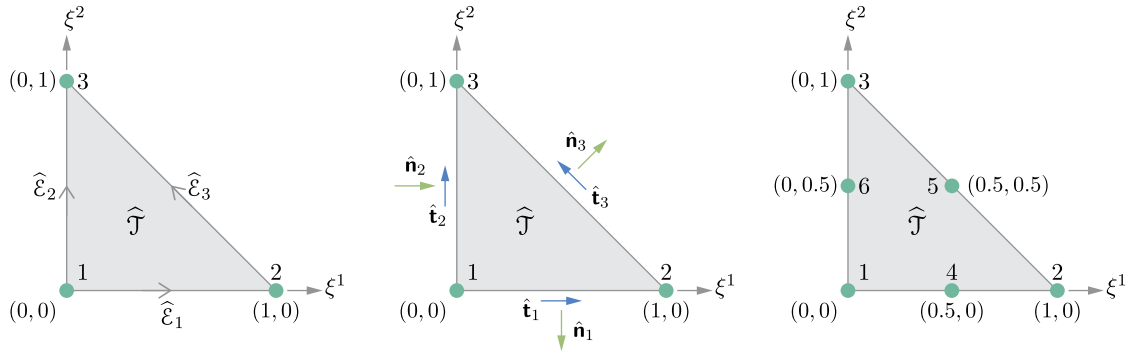
Fig. 1. The three-node reference element and edge numbers and orientations (left), the reference directions for the unit tangent and normal vectors (middle), and the six-node reference element (right).

assume that there exits a linear space $V(\mathcal{T})$ of functions $v : \mathcal{T} \to \mathbb{R}^m$ such that $\mathcal{P}(\mathcal{T}) \subset V(\mathcal{T})$, and Σ can be extended to its dual space $V(\mathcal{T})^\star$. Then, the local interpolation operator is defined as

$$I_{\mathcal{T}} : V(\mathcal{T}) \longrightarrow \mathcal{P}(\mathcal{T}), \quad I_{\mathcal{T}}(v) = \sum_{i=0}^{n_s} \sigma_i(v)\theta_i.$$

Note that $I_{\mathcal{T}}$ is a projection of $V(\mathcal{T})$ into $\mathcal{P}(\mathcal{T})$ that is not bijective, in general. In practice, by having the shape functions, we accept $I_{\mathcal{T}}(v)$ as an approximation of v and find the degrees of freedom as the unknowns.

Suppose $\widehat{\mathcal{T}}$ as shown in Fig. 1 is a reference triangular element with coordinates $\boldsymbol{\xi} = (\xi^1, \xi^2)$. We denote the edges of $\widehat{\mathcal{T}}$ by $\widehat{\mathcal{E}}_i, i = 1, 2, 3$ and their corresponding lengths by $\hat{\ell}_i, i = 1, 2, 3$. For an edge joining two vertices i and j, we define a unique orientation as $i \to j$, where $i < j$. According to Fig. 1, orientations $1 \to 2$, $1 \to 3$, and $2 \to 3$ are assigned to $\widehat{\mathcal{E}}_1$, $\widehat{\mathcal{E}}_2$, and $\widehat{\mathcal{E}}_3$, respectively. Moreover, we define a unit tangent vector $\hat{\mathbf{t}}_i$ and a unit normal vector $\hat{\mathbf{n}}_i$ on each edge; $\hat{\mathbf{t}}_i$ must agree with the edge orientation, and $\hat{\mathbf{n}}_i$ is obtained by a 90 degrees clockwise rotation of $\hat{\mathbf{t}}_i$, that is $\hat{\mathbf{n}}_i = \mathbf{R}\hat{\mathbf{t}}_i$, where

$$\mathbf{R} = \begin{bmatrix} 0 & 1 \\ -1 & 0 \end{bmatrix}. \tag{3.1}$$

We consider the following *reference* finite elements for our four field variables:

$$
\begin{aligned}
&\left(\widehat{\mathcal{T}}, \mathcal{P}_r(T\widehat{\mathcal{T}}), \Sigma^{\widehat{\mathcal{T}},1}\right) && \text{for displacement } \boldsymbol{U}, \\
&\left(\widehat{\mathcal{T}}, \mathcal{P}_r(\otimes^2 T\widehat{\mathcal{T}}), \Sigma^{\widehat{\mathcal{T}},\mathbf{c}}\right), \left(\widehat{\mathcal{T}}, \mathcal{P}_r^-(\otimes^2 T\widehat{\mathcal{T}}), \Sigma^{\widehat{\mathcal{T}},\mathbf{c}-}\right) && \text{for displacement gradient } \boldsymbol{K}, \\
&\left(\widehat{\mathcal{T}}, \mathcal{P}_r(\otimes^2 T\widehat{\mathcal{T}}), \Sigma^{\widehat{\mathcal{T}},\mathbf{d}}\right), \left(\widehat{\mathcal{T}}, \mathcal{P}_r^\ominus(\otimes^2 T\widehat{\mathcal{T}}), \Sigma^{\widehat{\mathcal{T}},\mathbf{d}-}\right) && \text{for stress } \boldsymbol{P}, \\
&\left(\widehat{\mathcal{T}}, \mathcal{P}_r(\widehat{\mathcal{T}}), \Sigma^{\widehat{\mathcal{T}},\ell}\right) && \text{for the pressure-like field } p.
\end{aligned}
\tag{3.2}
$$

In the following, our main focus is to provide explicit expressions for some bases of the above polynomial spaces, also known as local shape functions. We will consider $r = 1, 2$ for the corresponding polynomial spaces of $\boldsymbol{U}$, $\boldsymbol{K}$ and $\boldsymbol{P}$, and $r = 0, 1, 2$ for the corresponding polynomial space of p.

The Lagrange polynomials on the three-node $\widehat{\mathcal{T}}$ are

$$l_1^1 = 1 - \xi^1 - \xi^2, \quad l_2^1 = \xi^1, \quad l_3^1 = \xi^2. \tag{3.3}$$

Using (3.3), the Lagrange polynomials on the six-node $\widehat{\mathcal{T}}$ can be written as $l_i^2 = l_i^1(2l_i^1 - 1)$ and $l_{3+i}^2 = 4l_i^1 l_{i+1}^1$, where $i = 1, 2, 3$ and $l_4^1 = l_1^1$. For $r = 1, 2$, a basis of $\mathcal{P}_r(T\widehat{\mathcal{T}})$ includes

$$\boldsymbol{h}_{2i-1}^{\widehat{\mathcal{T}}} = \begin{bmatrix} l_i^r \\ 0 \end{bmatrix}, \quad \boldsymbol{h}_{2i}^{\widehat{\mathcal{T}}} = \begin{bmatrix} 0 \\ l_i^r \end{bmatrix}, \quad i = 1, 2, ..., 3r,$$

and the set of local degrees of freedom is $\Sigma^{\widehat{\mathcal{T}},1} = \left\{ V^1(\boldsymbol{\xi}_1), V^2(\boldsymbol{\xi}_1), ..., V^1(\boldsymbol{\xi}_{3r}), V^2(\boldsymbol{\xi}_{3r}) \right\}$, where $\boldsymbol{\xi}_i$ is the coordinates of the i-th node of the $3r$-node $\widehat{\mathcal{T}}$ as shown in Fig. 1. We will use $\mathcal{P}_r(T\widehat{\mathcal{T}}), r = 1, 2$ spanned by $\boldsymbol{h}_i^{\widehat{\mathcal{T}}}$ to construct the approximation space of $\boldsymbol{U}$.

Remark 7. We have listed some of the common vector-valued finite elements in the literature in the left column of Table 1. Nédélec's original finite elements are in $\mathbb{R}^3$ for both H(curl) and H(div) and for arbitrary polynomial degree [27,28]. He

Table 1
Tensorial analogues of some classical finite elements for vector fields.

Vector fields	Second-order tensors
Nédélec 1st-kind (N1) H(curl) element [27]	$(\mathcal{T}, \mathcal{P}_r^-(\otimes^2 T\mathcal{T}), \Sigma^{\mathcal{T},\mathbf{c}-})$
Nédélec 2nd-kind (N2) H(curl) element [28]	$(\mathcal{T}, \mathcal{P}_r(\otimes^2 T\mathcal{T}), \Sigma^{\mathcal{T},\mathbf{c}})$
Raviart–Thomas (RT) H(div) element [29]	$(\mathcal{T}, \mathcal{P}_r^\ominus(\otimes^2 T\mathcal{T}), \Sigma^{\mathcal{T},\mathbf{d}-})$
Brezzi–Douglas–Marini (BDM) H(div) element [30]	$(\mathcal{T}, \mathcal{P}_r(\otimes^2 T\mathcal{T}), \Sigma^{\mathcal{T},\mathbf{d}})$

Table 2
Vector valued bases for polynomial spaces of N1 denoted by $\mathcal{P}_r^-(T\widehat{\mathcal{T}})$ and N2 denoted by $\mathcal{P}_r(T\widehat{\mathcal{T}})$ for $r = 1, 2$.

r	$\mathcal{P}_r^-(T\widehat{\mathcal{T}})$		$\mathcal{P}_r(T\widehat{\mathcal{T}})$	
	$\mathbf{v}_J^{\widehat{\mathcal{T}},\widehat{\mathcal{E}}_k}$	$\mathbf{v}_J^{\widehat{\mathcal{T}},\widehat{\mathcal{T}}}$	$\mathbf{v}_J^{\widehat{\mathcal{T}},\widehat{\mathcal{E}}_k}$	$\mathbf{v}_J^{\widehat{\mathcal{T}},\widehat{\mathcal{T}}}$
1	$\mathbf{w}_{ij}$		$l_i\nabla l_j, l_j\nabla l_i$	
2	$l_i\mathbf{w}_{ij}, l_j\mathbf{w}_{ij}$	$l_3\mathbf{w}_{12}, l_2\mathbf{w}_{13}$	$l_i^2\nabla l_j, l_j^2\nabla l_i, l_il_j\nabla(l_j - l_i)$	$l_1l_2\nabla l_3, l_1l_3\nabla l_2, l_2l_3\nabla l_1$

introduced N1 and N2 H(curl) elements for $\mathbb{R}^3$. He also generalized RT and BDM elements to $\mathbb{R}^3$ by developing H(div) version of N1 and N2, respectively. Following his works, the 2D version of H(curl) elements are also called Nédélec elements, but as he himself pointed out in the conclusion of [27], in 2D, H(curl) elements can be easily obtained by a 90 degree rotation of bases of H(div) elements.

For $\mathbf{K} \in H^\mathbf{c}$ and $\mathbf{P} \in H^\mathbf{d}$, we write the tensorial analogues of some classical finite elements for vector fields as summarized in Table 1 (also see Remark 7). All the finite element spaces given in the left column of Table 1 are generalized by Arnold et al. [31] to two spaces of finite element differential forms with arbitrary order for any degree of polynomials and any number of dimensions. Moreover, they derived geometric decomposition of these spaces, which provides explicit local bases for them. See [32,33] for a more intuitive generalization of these vector-valued finite elements. Here, based on the results of [31], we write some analogues tensorial bases for the reference element $\widehat{\mathcal{T}}$ and $r = 1, 2$. By using Theorem 7 in [17], one can calculate these tensorial bases implicitly, e.g., see [17, Examples 9 and 10]. Let us ignore the superscript of l_i^1 in (3.3) and let $\nabla l_i = \begin{bmatrix} \partial l_i/\partial \xi^1 & \partial l_i/\partial \xi^2 \end{bmatrix}$ be a row vector. Also, for each edge of a triangular element with orientation $i \to j$, consider the Whitney function

$$\mathbf{w}_{ij} = l_i\nabla l_j - l_j\nabla l_i. \tag{3.4}$$

The bases for polynomial spaces of N1 and N2, which we respectively denote by $\mathcal{P}_r^-(T\widehat{\mathcal{T}})$ and $\mathcal{P}_r(T\widehat{\mathcal{T}})$ are given in Table 2 for the orders $r = 1, 2$ [31]. Local shape functions $\mathbf{v}_J^{\widehat{\mathcal{T}},\widehat{\mathcal{E}}_k}$ associated with the edge $\widehat{\mathcal{E}}_k$ with orientation $i \to j$, which is indicated in Fig. 1, and local shape functions $\mathbf{v}_J^{\widehat{\mathcal{T}},\widehat{\mathcal{T}}}$ are associated with the reference element $\widehat{\mathcal{T}}$ itself and defined for $r \geq 2$. The tangent component of a shape function $\mathbf{v}$ on an edge $\mathcal{E}_i$ is denoted by $\langle \mathbf{v}, \mathbf{t}_i \rangle$. For a given r, both $\mathcal{P}_r^-(T\widehat{\mathcal{T}})$ and $\mathcal{P}_r(T\widehat{\mathcal{T}})$ contain polynomials of the same order, but

$$\left\{ \left\langle \mathbf{v}_J^{\widehat{\mathcal{T}},\widehat{\mathcal{E}}_k}, \mathbf{t}_k \right\rangle : \mathbf{v}_J^{\widehat{\mathcal{T}},\widehat{\mathcal{E}}_k} \in \mathcal{P}_r^-(T\widehat{\mathcal{T}}), J = 1, 2, ..., r \right\} \qquad \text{is a basis of } \mathcal{P}_{r-1}(\widehat{\mathcal{E}}_k),$$

$$\left\{ \left\langle \mathbf{v}_J^{\widehat{\mathcal{T}},\widehat{\mathcal{E}}_k}, \mathbf{t}_k \right\rangle : \mathbf{v}_J^{\widehat{\mathcal{T}},\widehat{\mathcal{E}}_k} \in \mathcal{P}_r(T\widehat{\mathcal{T}}), J = 1, 2, ..., r + 1 \right\} \quad \text{is a basis of } \mathcal{P}_r(\widehat{\mathcal{E}}_k),$$

where $\mathcal{P}_r(\widehat{\mathcal{E}}_k)$ denotes the one-dimensional polynomial space of order r on the edge $\widehat{\mathcal{E}}_k$. Also, for any J, $\mathbf{v}_J^{\widehat{\mathcal{T}},\widehat{\mathcal{T}}}$ is a zero-tangent bubble polynomial of order r on $\widehat{\mathcal{T}}$, meaning that its tangent components are zero on all the three edges. Some examples of these shape functions are depicted in Fig. 2.

To interpolate $\mathbf{K} \in H^\mathbf{c}$, we define the following tensorial shape functions:

$$\mathbf{r}_{1,J}^{\widehat{\mathcal{T}},\widehat{\mathcal{E}}_k} = \begin{bmatrix} \mathbf{v}_J^{\widehat{\mathcal{T}},\widehat{\mathcal{E}}_k} \\ \mathbf{0} \end{bmatrix}, \quad \mathbf{r}_{2,J}^{\widehat{\mathcal{T}},\widehat{\mathcal{E}}_k} = \begin{bmatrix} \mathbf{0} \\ \mathbf{v}_J^{\widehat{\mathcal{T}},\widehat{\mathcal{E}}_k} \end{bmatrix}, \quad \mathbf{r}_{1,J}^{\widehat{\mathcal{T}},\widehat{\mathcal{T}}} = \begin{bmatrix} \mathbf{v}_J^{\widehat{\mathcal{T}},\widehat{\mathcal{T}}} \\ \mathbf{0} \end{bmatrix}, \quad \mathbf{r}_{2,J}^{\widehat{\mathcal{T}},\widehat{\mathcal{T}}} = \begin{bmatrix} \mathbf{0} \\ \mathbf{v}_J^{\widehat{\mathcal{T}},\widehat{\mathcal{T}}} \end{bmatrix}. \tag{3.5}$$

Accordingly, $\mathcal{P}_r^-(\otimes^2 T\widehat{\mathcal{T}})$ in (3.2)$_2$ is defined by spanning the set of local shape functions $\left\{ \mathbf{r}_{I,J}^{\widehat{\mathcal{T}},\widehat{\mathcal{E}}_k}, \mathbf{r}_{I,J}^{\widehat{\mathcal{T}},\widehat{\mathcal{T}}} \right\}$ that is obtained from $\mathcal{P}_r^-(T\widehat{\mathcal{T}})$. $\mathcal{P}_r(\otimes^2 T\widehat{\mathcal{T}})$ in (3.2)$_2$ is defined similarly by using $\mathcal{P}_r(T\widehat{\mathcal{T}})$. The explicit form of the spaces $\mathcal{P}_r^-(\otimes^2 T\widehat{\mathcal{T}})$ and $\mathcal{P}_r(\otimes^2 T\widehat{\mathcal{T}})$ are given in [17, Example 3]. Suppose $\overrightarrow{\mathbf{T}}_I := \begin{bmatrix} T^{I1} & T^{I2} \end{bmatrix}^\mathsf{T}$ is a column vector containing the elements of the I-th row of a $\binom{2}{0}$-tensor $\mathbf{T}$. The sets $\Sigma^{\widehat{\mathcal{T}},\mathbf{c}}$ and $\Sigma^{\widehat{\mathcal{T}},\mathbf{c}-}$ in (3.2)$_2$ consist of the following local degrees of freedom:
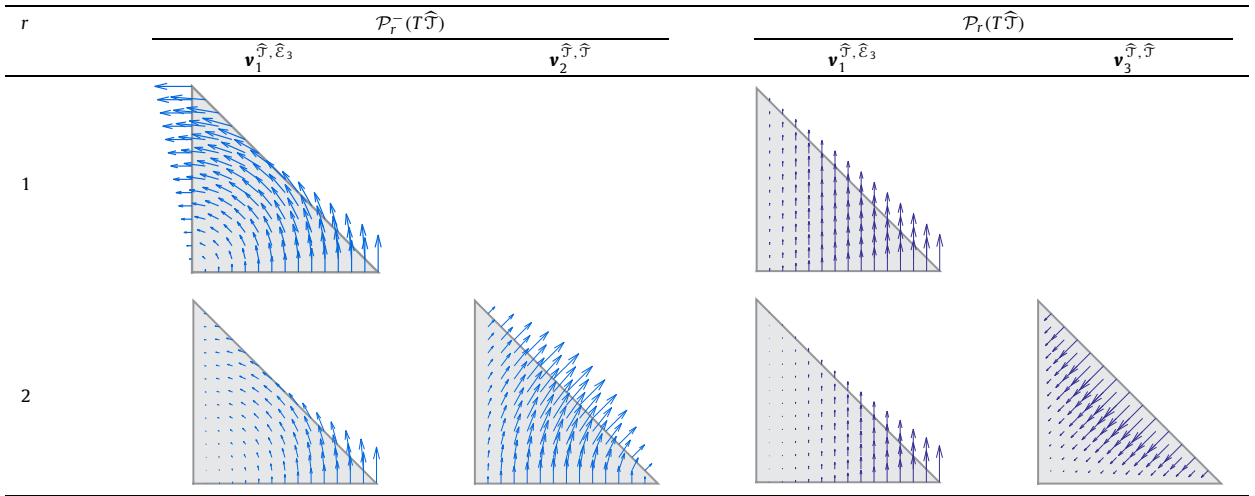
r	$\mathcal{P}_r^-(T\widehat{\mathfrak{T}})$		$\mathcal{P}_r(T\widehat{\mathfrak{T}})$	
	$\mathbf{v}_1^{\widehat{\mathfrak{T}},\widehat{\mathcal{E}}_3}$	$\mathbf{v}_2^{\widehat{\mathfrak{T}},\widehat{\mathfrak{T}}}$	$\mathbf{v}_1^{\widehat{\mathfrak{T}},\widehat{\mathcal{E}}_3}$	$\mathbf{v}_3^{\widehat{\mathfrak{T}},\widehat{\mathfrak{T}}}$

Fig. 2. The illustration of some of the bases given in Table 2.

$$\phi_{I,J}^{\widehat{\mathfrak{T}},\widehat{\mathcal{E}}_k}(\boldsymbol{T}) = \int_{\widehat{\mathcal{E}}_k}\left(\frac{\hat{s}}{\hat{\ell}_k}\right)^{J-1}\langle\overrightarrow{\boldsymbol{T}}_I,\hat{\mathbf{t}}_k\rangle\,d\hat{s}, \quad \phi_{I,J}^{\widehat{\mathfrak{T}},\widehat{\mathfrak{T}}}(\boldsymbol{T}) = \int_{\widehat{\mathfrak{T}}}\langle\overrightarrow{\boldsymbol{T}}_I,\hat{\mathbf{v}}_J\rangle\,d\hat{A}, \tag{3.6}$$

where $\hat{\mathbf{v}}_J$ is a vector-valued polynomial in $\mathbb{R}^2$, see [17, Theorem 7]. Note that $\phi_{I,J}^{\widehat{\mathfrak{T}},\widehat{\mathcal{E}}_k}$ and $\phi_{I,J}^{\widehat{\mathfrak{T}},\widehat{\mathfrak{T}}}$ are associated to the edges $\widehat{\mathcal{E}}_k$ and the area of the reference triangle $\widehat{\mathfrak{T}}$, respectively. In practice, degrees of freedom are obtained by numerically solving the final discrete system so their direct calculation is needed only when we impose some of the boundary conditions strongly. Hence, in 2D, we do not directly compute the degrees of freedom such as $\phi_{I,J}^{\widehat{\mathfrak{T}},\widehat{\mathfrak{T}}}$ that are defined over the area of the elements, and hence, specifying $\hat{\mathbf{v}}_J$ is not required. Also, we choose the polynomials $(\hat{s}/\hat{\ell}_k)^{J-1}$, $J = 1,2,3$ to simplify the calculation of $\phi_{I,J}^{\widehat{\mathfrak{T}},\widehat{\mathcal{E}}_k}$ at the domain boundaries. The choice for these polynomials is not unique, in general. In finite element approximation, degrees of freedom must be a dual basis for the space spanned by the shape functions. Hence, we define some modified shape functions $\bar{\mathbf{r}}_{I,J}^{\widehat{\mathfrak{T}},\widehat{\mathcal{E}}_k}$ by writing a linear combination of $\mathbf{r}_{I,J}^{\widehat{\mathfrak{T}},\widehat{\mathcal{E}}_k}$ over J such that

$$\phi_{M,N}^{\widehat{\mathfrak{T}},\widehat{\mathcal{E}}_l}\left(\bar{\mathbf{r}}_{I,J}^{\widehat{\mathfrak{T}},\widehat{\mathcal{E}}_k}\right) = \begin{cases} 1, & \text{if } k = l \text{ and } I = M \text{ and } J = N, \\ 0, & \text{otherwise.} \end{cases} \tag{3.7}$$

In the case of $\mathcal{P}_r^-(\otimes^2 T\widehat{\mathfrak{T}})$, we have $\bar{\mathbf{r}}_{I,1}^{\widehat{\mathfrak{T}},\widehat{\mathcal{E}}_k} = \mathbf{r}_{I,1}^{\widehat{\mathfrak{T}},\widehat{\mathcal{E}}_k}$ for $r = 1$, and the following shape functions for $r = 2$:

$$\bar{\mathbf{r}}_{I,1}^{\widehat{\mathfrak{T}},\widehat{\mathcal{E}}_k} = 4\mathbf{r}_{I,1}^{\widehat{\mathfrak{T}},\widehat{\mathcal{E}}_k} - 2\mathbf{r}_{I,2}^{\widehat{\mathfrak{T}},\widehat{\mathcal{E}}_k}, \qquad \bar{\mathbf{r}}_{I,2}^{\widehat{\mathfrak{T}},\widehat{\mathcal{E}}_k} = -6\mathbf{r}_{I,1}^{\widehat{\mathfrak{T}},\widehat{\mathcal{E}}_k} + 6\mathbf{r}_{I,2}^{\widehat{\mathfrak{T}},\widehat{\mathcal{E}}_k},$$

Considering $\mathcal{P}_r(\otimes^2 T\widehat{\mathfrak{T}})$, one obtains

$$\bar{\mathbf{r}}_{I,1}^{\widehat{\mathfrak{T}},\widehat{\mathcal{E}}_k} = 4\mathbf{r}_{I,1}^{\widehat{\mathfrak{T}},\widehat{\mathcal{E}}_k} + 2\mathbf{r}_{I,2}^{\widehat{\mathfrak{T}},\widehat{\mathcal{E}}_k}, \qquad \bar{\mathbf{r}}_{I,2}^{\widehat{\mathfrak{T}},\widehat{\mathcal{E}}_k} = -6\mathbf{r}_{I,1}^{\widehat{\mathfrak{T}},\widehat{\mathcal{E}}_k} - 6\mathbf{r}_{I,2}^{\widehat{\mathfrak{T}},\widehat{\mathcal{E}}_k}.$$

for $r = 1$, and the following for $r = 2$:

$$\bar{\mathbf{r}}_{I,1}^{\widehat{\mathfrak{T}},\widehat{\mathcal{E}}_k} = 9\mathbf{r}_{I,1}^{\widehat{\mathfrak{T}},\widehat{\mathcal{E}}_k} - 3\mathbf{r}_{I,2}^{\widehat{\mathfrak{T}},\widehat{\mathcal{E}}_k} - 9\mathbf{r}_{I,3}^{\widehat{\mathfrak{T}},\widehat{\mathcal{E}}_k},$$
$$\bar{\mathbf{r}}_{I,2}^{\widehat{\mathfrak{T}},\widehat{\mathcal{E}}_k} = -36\mathbf{r}_{I,1}^{\widehat{\mathfrak{T}},\widehat{\mathcal{E}}_k} + 24\mathbf{r}_{I,2}^{\widehat{\mathfrak{T}},\widehat{\mathcal{E}}_k} + 60\mathbf{r}_{I,3}^{\widehat{\mathfrak{T}},\widehat{\mathcal{E}}_k},$$
$$\bar{\mathbf{r}}_{I,3}^{\widehat{\mathfrak{T}},\widehat{\mathcal{E}}_k} = 30\mathbf{r}_{I,1}^{\widehat{\mathfrak{T}},\widehat{\mathcal{E}}_k} - 30\mathbf{r}_{I,2}^{\widehat{\mathfrak{T}},\widehat{\mathcal{E}}_k} + 60\mathbf{r}_{I,3}^{\widehat{\mathfrak{T}},\widehat{\mathcal{E}}_k}.$$

Moreover, by choosing $\hat{\mathbf{v}}_J$ properly in $(3.6)_2$, one can show that

$$\phi_{M,N}^{\widehat{\mathfrak{T}},\widehat{\mathcal{E}}_k}\left(\mathbf{r}_{I,J}^{\widehat{\mathfrak{T}},\widehat{\mathfrak{T}}}\right) = \phi_{M,N}^{\widehat{\mathfrak{T}},\widehat{\mathfrak{T}}}\left(\bar{\mathbf{r}}_{I,J}^{\widehat{\mathfrak{T}},\widehat{\mathcal{E}}_k}\right) = 0,$$
$$\phi_{M,N}^{\widehat{\mathfrak{T}},\widehat{\mathfrak{T}}}\left(\mathbf{r}_{I,J}^{\widehat{\mathfrak{T}},\widehat{\mathfrak{T}}}\right) = \begin{cases} 1, & \text{if } I = M \text{ and } J = N, \\ 0, & \text{otherwise.} \end{cases} \tag{3.8}$$

We will use the set of reference shape functions $\left\{\bar{\mathbf{r}}_{I,J}^{\widehat{\mathfrak{T}},\widehat{\mathcal{E}}_k}, \mathbf{r}_{I,J}^{\widehat{\mathfrak{T}},\widehat{\mathfrak{T}}}\right\}$ to approximate $\boldsymbol{K} \in H^{\mathbf{c}}$.

Table 3

Numbers of local degrees of freedom (DOF) in terms of the order of the corresponding polynomial spaces r.

DOF	Number of DOF			
	For each node	For each edge	For $\mathcal{T}$	Total
$\Sigma^{\mathcal{T},1}$	2	0	0	$6r$
$\Sigma^{\mathcal{T},\mathbf{c}-}$, $\Sigma^{\mathcal{T},\mathbf{d}-}$	0	$2r$	$2(r^2 - r)$	$2r(r+2)$
$\Sigma^{\mathcal{T},\mathbf{c}}$, $\Sigma^{\mathcal{T},\mathbf{d}}$	0	$2(r+1)$	$2(r^2-1)$	$2(r+1)(r+2)$
$\Sigma^{\mathcal{T},\ell}$	0	0	$(r+1)(r+2)/2$	$(r+1)(r+2)/2$

In 2D, the spaces of type $H^{\mathbf{c}}$ and $H^{\mathbf{d}}$ are transformed to each other by a 90 degree rotation. To see this, recall the definitions of $H^{\mathbf{c}}$ and $H^{\mathbf{d}}$ in the distributional sense and observe that $\mathbf{grad}(q) = \mathbf{R}^{\mathsf{T}} \mathbf{s}(q)$, where q is a smooth function. Therefore, to construct $(3.2)_3$ for approximating $\boldsymbol{P} \in H^{\mathbf{d}}$, we simply need the following shape functions:

$$\bar{\boldsymbol{s}}_{I,J}^{\widehat{\mathcal{T}},\widehat{\mathcal{E}}_k} = \bar{\boldsymbol{r}}_{I,J}^{\widehat{\mathcal{T}},\widehat{\mathcal{E}}_k} \mathbf{R}^{\mathsf{T}}, \quad \boldsymbol{s}_{I,J}^{\widehat{\mathcal{T}},\widehat{\mathcal{T}}} = \boldsymbol{r}_{I,J}^{\widehat{\mathcal{T}},\widehat{\mathcal{T}}} \mathbf{R}^{\mathsf{T}}. \tag{3.9}$$

The corresponding local degrees of freedom are

$$\psi_{I,J}^{\widehat{\mathcal{T}},\widehat{\mathcal{E}}_k}(\boldsymbol{T}) = \int_{\widehat{\mathcal{E}}_k} \left(\frac{\hat{s}}{\hat{\ell}_k}\right)^{J-1} \langle \overrightarrow{\boldsymbol{T}}_I, \hat{\mathbf{n}}_k \rangle \, d\hat{s}, \quad \psi_{I,J}^{\widehat{\mathcal{T}},\widehat{\mathcal{T}}}(\boldsymbol{T}) = \int_{\widehat{\mathcal{T}}} \langle \overrightarrow{\boldsymbol{T}}_I, \mathbf{R}\hat{\boldsymbol{v}}_J \rangle \, d\hat{A}. \tag{3.10}$$

Note that $\psi_{M,N}^{\widehat{\mathcal{T}},\widehat{\mathcal{E}}_l}\left(\bar{\boldsymbol{s}}_{I,J}^{\widehat{\mathcal{T}},\widehat{\mathcal{E}}_k}\right) = \psi_{M,N}^{\widehat{\mathcal{T}},\widehat{\mathcal{E}}_l}\left(\bar{\boldsymbol{r}}_{I,J}^{\widehat{\mathcal{T}},\widehat{\mathcal{E}}_k} \mathbf{R}^{\mathsf{T}}\right) = \phi_{M,N}^{\widehat{\mathcal{T}},\widehat{\mathcal{E}}_l}\left(\bar{\boldsymbol{r}}_{I,J}^{\widehat{\mathcal{T}},\widehat{\mathcal{E}}_k}\right)$, and thus, the condition (3.7) holds for $\psi_{I,J}^{\widehat{\mathcal{T}},\widehat{\mathcal{E}}_k}$ and $\bar{\boldsymbol{s}}_{I,J}^{\widehat{\mathcal{T}},\widehat{\mathcal{E}}_k}$ as well. Similarly, one can write the condition (3.8) for (3.9) and (3.10). The space $\mathcal{P}_r^{\ominus}(\otimes^2 T\widehat{\mathcal{T}})$ in $(3.2)_3$ is spanned by the set $\left\{\bar{\boldsymbol{s}}_{I,J}^{\widehat{\mathcal{T}},\widehat{\mathcal{E}}_k}, \boldsymbol{s}_{I,J}^{\widehat{\mathcal{T}},\widehat{\mathcal{T}}}\right\}$, which is obtained from a 90 degree rotation of the bases of $\mathcal{P}_r^{-}(T\widehat{\mathcal{T}})$. The same set spans $\mathcal{P}_r(\otimes^2 T\widehat{\mathcal{T}})$ in $(3.2)_3$ if it is written by a 90 degree rotation of the bases of $\mathcal{P}_r(T\widehat{\mathcal{T}})$. Also, note that $\mathcal{P}_r^{-}(\otimes^2 T\widehat{\mathcal{T}})$ and $\mathcal{P}_r^{\ominus}(\otimes^2 T\widehat{\mathcal{T}})$ in (3.2) are transformed to each other by a 90 degree rotation. The explicit expression of these spaces are given in [17, Example 3].

For the reference finite element of pressure $(3.2)_4$, the set of local shape functions $\{t_i^{\widehat{\mathcal{T}}}\}$, which spans $\mathcal{P}_r(\widehat{\mathcal{T}})$, is $\{1\}$ for $r = 0$, $\{1, \xi^1, \xi^2\}$ for $r = 1$, and $\{1, \xi^1, \xi^2, (\xi^1)^2, (\xi^2)^2, \xi^1\xi^2\}$ for $r = 2$. The corresponding local degrees of freedom are of the form

$$\omega_i^{\widehat{\mathcal{T}}}(f) = \frac{1}{\hat{A}} \int_{\widehat{\mathcal{T}}} \hat{p}_i^r f \, d\hat{A}, \tag{3.11}$$

where $\hat{p}_i^r$, $i = 1, 2, ..., n_s$ are polynomials of order r on $\widehat{\mathcal{T}}$, which can be calculated by solving $\omega_i^{\widehat{\mathcal{T}}}(t_j^{\widehat{\mathcal{T}}}) = \delta_{ij}$. However, as was discussed earlier, we do not calculate $\omega_i^{\widehat{\mathcal{T}}}$ directly, and hence, calculating $\hat{p}_i^r$ is not necessary.

The numbers of local degrees of freedom (the number of local shape functions) for the four types of finite elements that we discussed above are summarized in Table 3. This holds for the reference finite elements (3.2) and any finite elements that we will generate from them for an arbitrary triangle $\mathcal{T}$.

Next we explain how to construct a family of finite elements for a given mesh based on the reference finite elements (3.2). Let $\mathcal{B}_h$ denote a triangulation (or simply a mesh) of the reference configuration $\mathcal{B}$, where $\mathcal{B}_h$ consists of arbitrary triangles $\mathcal{T}$, and $h := \max \operatorname{diam} \mathcal{T}$, $\forall \mathcal{T} \in \mathcal{B}_h$. Note that the intersection of any two distinct triangles of $\mathcal{B}_h$ can be empty, a common edge joining two common vertices, or only a vertex of those two triangles. We locally assign the numbers $1, 2, 3$ to vertices of each $\mathcal{T} \in \mathcal{B}_h$, to which we will refer as the ordering of vertices. Let $\mathbf{X}_i = (X_i^1, X_i^2)$ denote the Cartesian coordinates of the i-th vertex of $\mathcal{T}$. The reference triangle $\widehat{\mathcal{T}}$ shown in Fig. 1 can be mapped onto any $\mathcal{T} \in \mathcal{B}_h$ by an affine transformation $\mathbf{T}_{\mathcal{T}}$ given by

$$\mathbf{T}_{\mathcal{T}} : \widehat{\mathcal{T}} \longrightarrow \mathcal{T}, \quad \mathbf{T}_{\mathcal{T}}(\boldsymbol{\xi}) := \mathbf{J}_{\mathcal{T}}\boldsymbol{\xi} + \mathbf{a}_{\mathcal{T}}, \tag{3.12}$$

where

$$\mathbf{J}_{\mathcal{T}} = \begin{bmatrix} X_2^1 - X_1^1 & X_3^1 - X_1^1 \\ X_2^2 - X_1^1 & X_3^2 - X_1^1 \end{bmatrix} \quad \text{and} \quad \mathbf{a}_{\mathcal{T}} = \begin{bmatrix} X_1^1 \\ X_1^2 \end{bmatrix}.$$

The above mapping is bijective and $\mathbf{J}_{\mathcal{T}}$ is invertible. Let $\mathcal{E}_i^{\mathcal{T}} = \mathbf{T}_{\mathcal{T}}(\widehat{\mathcal{E}}_i)$, $i = 1, 2, 3$ denote the edges of $\mathcal{T}$. Also, assume that $\mathcal{E}_i^{\mathcal{T}}$ inherits the orientation of $\widehat{\mathcal{E}}_i$, i.e., if the orientation of $\widehat{\mathcal{E}}_i$ in terms of the coordinates is $\boldsymbol{\xi}_k \to \boldsymbol{\xi}_l$, then the orientation of $\mathcal{E}_i^{\mathcal{T}}$ is $\mathbf{T}_{\mathcal{T}}(\boldsymbol{\xi}_k) = \mathbf{X}_k \to \mathbf{X}_l = \mathbf{T}_{\mathcal{T}}(\boldsymbol{\xi}_l)$. Similar to what we discussed for the reference element, the tangent vector $\mathbf{t}_i$ defined on $\mathcal{E}_i^{\mathcal{T}}$ accepts the orientation of $\mathcal{E}_i^{\mathcal{T}}$, and the normal vector on $\mathcal{E}_i^{\mathcal{T}}$ is obtained by $\mathbf{n}_i = \mathbf{R}\mathbf{t}_i$.

We use the numbering scheme discussed in [34] for convenience in defining global shape functions and degrees of freedom of conforming $H^{\mathbf{c}}$ and $H^{\mathbf{d}}$ finite elements and also for their efficient assembly. In this scheme, a global number is

assigned to each vertex of the mesh. Then, the ordering of the three vertices of each element $\mathcal{T}$ is defined based on the ascending order of the global numbers associated to them, i.e., the first vertex of each $\mathcal{T}$ has the smallest global number among the three vertices and the third vertex has the largest. Using this ordering and the edge orientations of the reference element (see Fig. 1), the orientation of every edge in the mesh joining two vertices will be from the vertex with the smaller to the vertex with the larger global number. The advantage of this scheme is that the orientation of an edge shared by two adjacent elements in the mesh is identical to that of the edge in either of the two elements. More precisely, assume that $\mathcal{T}$ and $\mathcal{T}'$ are adjacent in $\mathcal{B}_h$ and share a common edge $\mathcal{E}$ such that $\mathcal{E} \cap \mathcal{T} = \mathcal{E}_i^{\mathcal{T}}$ and $\mathcal{E} \cap \mathcal{T}' = \mathcal{E}_{i'}^{\mathcal{T}'}$. The scheme guarantees that $\mathcal{E}_i^{\mathcal{T}}$ and $\mathcal{E}_{i'}^{\mathcal{T}'}$ inherit an identical orientation from $\widehat{\mathcal{E}}_i$ and $\widehat{\mathcal{E}}_{i'}$, regardless of their local edge numberings i and i'. For an illustration of this, see [34, Figure 5.1]. It follows that both the tangent and the normal vectors that are defined on $\mathcal{E}_i^{\mathcal{T}}$ and $\mathcal{E}_{i'}^{\mathcal{T}'}$ are identical.

Note that the above scheme violates the standard convention that the three vertices of every element in the mesh have a counterclockwise ordering. Therefore, one should keep in mind that not all the normal vectors of the exterior edges lying on the boundaries of the mesh are pointed outward, and not all their tangent vectors are oriented in the counterclockwise direction. Also, $\det \mathbf{J}_{\mathcal{T}}$ can be either positive or negative, so it would be useful to define the following constant for each element:

$$o_{\mathcal{T}} = \mathrm{sign}\left(\det \mathbf{J}_{\mathcal{T}}\right).$$

Note that $o_{\mathcal{T}} = 1$ if the three vertices of $\mathcal{T}$ have the counterclockwise ordering, and $o_{\mathcal{T}} = -1$ otherwise.

In a general setting, let $\left(\widehat{\mathcal{T}}, \mathcal{P}(\widehat{\mathcal{T}}), \Sigma^{\widehat{\mathcal{T}}}\right)$ be a reference finite element and let $V(\widehat{\mathcal{T}})$ be a linear space of $\mathbb{R}^m$-valued functions in $\widehat{\mathcal{T}}$ such that $\mathcal{P}(\widehat{\mathcal{T}}) \subset V(\widehat{\mathcal{T}})$ and $\Sigma^{\widehat{\mathcal{T}}}$ can be extended to $V(\widehat{\mathcal{T}})^\star$. Also, for any $\mathcal{T} \in \mathcal{B}_h$, suppose $\Psi_{\mathcal{T}} : V(\widehat{\mathcal{T}}) \longrightarrow V(\mathcal{T})$ is a linear bijective mapping, which preserves the structure between $V(\widehat{\mathcal{T}})$ and its counterpart $V(\mathcal{T})$, i.e., $\Psi_{\mathcal{T}}$ is an isomorphism. Then, by using the reference finite element and the following proposition, one can define a set of finite elements for all $\mathcal{T}$ in $\mathcal{B}_h$ [26].

Proposition 8. *Let $\Psi_{\mathcal{T}} : V(\widehat{\mathcal{T}}) \longrightarrow V(\mathcal{T})$ be a linear bijection. For any $\mathcal{T} \in \mathcal{B}_h$, $\left(\mathcal{T}, \mathcal{P}(\mathcal{T}), \Sigma^{\mathcal{T}}\right)$ defined as*

$$\begin{cases} \mathcal{T} = \mathbf{T}_{\mathcal{T}}(\widehat{\mathcal{T}}) \\ \mathcal{P}(\mathcal{T}) = \left\{ \Psi_{\mathcal{T}}(\hat{p}) : \hat{p} \in \mathcal{P}(\widehat{\mathcal{T}}) \right\} \\ \Sigma^{\mathcal{T}} = \left\{ \sigma_1^{\mathcal{T}}, \sigma_2^{\mathcal{T}}, \dots \sigma_{n_s}^{\mathcal{T}} : \sigma_i^{\mathcal{T}}(p) = \sigma_i^{\widehat{\mathcal{T}}}\left(\Psi_{\mathcal{T}}^{-1}(p)\right), \forall p \in \mathcal{P}(\mathcal{T}), i = 1, 2, \dots, n_s \right\} \end{cases}$$

is a finite element with the local shape functions $\theta_i^{\mathcal{T}} = \Psi_{\mathcal{T}}\left(\theta_i^{\widehat{\mathcal{T}}}\right)$, $i = 1, 2, \dots, n_s$, and the local interpolation operator

$$\mathrm{I}_{\mathcal{T}} : V(\mathcal{T}) \longrightarrow \mathcal{P}(\mathcal{T}), \quad \mathrm{I}_{\mathcal{T}}(v) = \sum_{i=0}^{n_s} \sigma_i^{\mathcal{T}}(v)\theta_i^{\mathcal{T}}. \tag{3.13}$$

Proof. By assumption, $\hat{p} = \Psi_{\mathcal{T}}^{-1}(p)$ is bijective, $\forall p \in \mathcal{P}(\mathcal{T})$, and the mapping $\hat{p} \longmapsto \left(\sigma_1^{\widehat{\mathcal{T}}}(\hat{p}), \dots, \sigma_{n_s}^{\widehat{\mathcal{T}}}(\hat{p})\right)$ is a bijection, $\forall \hat{p} \in \mathcal{P}(\widehat{\mathcal{T}})$. Therefore, the composition mapping $p \longmapsto \left(\sigma_1^{\mathcal{T}}(p), \dots, \sigma_{n_s}^{\mathcal{T}}(p)\right)$ is bijective, $\forall p \in \mathcal{P}(\mathcal{T})$, and $\left(\mathcal{T}, \mathcal{P}(\mathcal{T}), \Sigma^{\mathcal{T}}\right)$ is a finite element. $\theta_i^{\mathcal{T}} \in \mathcal{P}^{\mathcal{T}}$ and $\sigma_j^{\mathcal{T}}\left(\theta_i^{\mathcal{T}}\right) = \sigma_j^{\widehat{\mathcal{T}}}\left(\Psi_{\mathcal{T}}^{-1}(\theta_i^{\mathcal{T}})\right) = \sigma_j^{\widehat{\mathcal{T}}}\left(\theta_i^{\widehat{\mathcal{T}}}\right) = \delta_{ij}$, for $i, j = 1, 2, \dots, n_s$, and hence, $\theta_i^{\mathcal{T}}$, $i = 1, 2, \dots n_s$ are the local shape functions. Next we show that the local interpolation operator $\mathrm{I}_{\mathcal{T}}$ is well-defined. If $q \in P(\mathcal{T})$, there exists $\hat{q} \in P(\widehat{\mathcal{T}}) \subset V(\widehat{\mathcal{T}})$ such that $q = \Psi_{\mathcal{T}}(\hat{q})$, so $q \in V(\mathcal{T})$, and we conclude that $P(\mathcal{T}) \subset V(\mathcal{T})$. Also, knowing that $\sigma_i^{\widehat{\mathcal{T}}}$ can be calculated for elements of $V(\widehat{\mathcal{T}})$, one can write $\sigma_i^{\mathcal{T}}(v) = \sigma_i^{\widehat{\mathcal{T}}}\left(\Psi_{\mathcal{T}}^{-1}(v)\right)$ for any $v \in V(\mathcal{T})$, and hence, $\Sigma^{\mathcal{T}}$ can be extended to $V(\mathcal{T})^\star$. $\square$

Consider the reference finite element of displacement $\left(\widehat{\mathcal{T}}, \mathcal{P}_r(T\widehat{\mathcal{T}}), \Sigma^{\widehat{\mathcal{T}}, 1}\right)$. Let $V(\widehat{\mathcal{T}}) = C^0(T\widehat{\mathcal{T}})$ and define $V(\mathcal{T})$ similarly. Use the mapping

$$\mathbf{T}_{\mathcal{T}}^1 : C^0(T\widehat{\mathcal{T}}) \longrightarrow C^0(T\mathcal{T}), \quad \mathbf{T}_{\mathcal{T}}^1(\widehat{\boldsymbol{V}}) := \widehat{\boldsymbol{V}} \circ \mathbf{T}_{\mathcal{T}}^{-1}, \tag{3.14}$$

and generate the family of finite elements $\left\{\left(\mathcal{T}, \mathcal{P}_r(T\mathcal{T}), \Sigma^{\mathcal{T}, 1}\right)\right\}_{\mathcal{T} \in \mathcal{B}_h}$ as described in Proposition 8. Accordingly, the local shape functions are $\boldsymbol{h}_k^{\mathcal{T}} = \mathbf{T}_{\mathcal{T}}^1\left(\boldsymbol{h}_k^{\widehat{\mathcal{T}}}\right)$. It is straightforward to check that $\boldsymbol{h}_k^{\mathcal{T}}$ is a Lagrange polynomial on $\mathcal{T}$, and members of the set of degrees of freedom $\Sigma^{\mathcal{T}, 1}$ are the values of the interpolated function at the nodes of $\mathcal{T}$.

The mapping (3.14) does not transform $H^{\mathbf{c}}(T\widehat{\mathcal{T}})$ into $H^{\mathbf{c}}(T\mathcal{T})$ or $H^{\mathbf{d}}(T\widehat{\mathcal{T}})$ into $H^{\mathbf{d}}(T\mathcal{T})$. Instead, one needs to use the Piola transforms. Considering the affine mapping (3.12), the Piola transforms $\mathbf{T}_{\mathcal{T}}^{\mathbf{c}}$ and $\mathbf{T}_{\mathcal{T}}^{\mathbf{d}}$ are defined as

$$\mathbf{T}_{\mathfrak{I}}^{\mathbf{c}} : H^{\mathbf{c}}(T\widehat{\mathfrak{I}}) \longrightarrow H^{\mathbf{c}}(T\mathfrak{I}), \quad \mathbf{T}_{\mathfrak{I}}^{\mathbf{c}}(\widehat{\boldsymbol{V}}) := \mathbf{J}_{\mathfrak{I}}^{-\mathsf{T}}\widehat{\boldsymbol{V}} \circ \mathbf{T}_{\mathfrak{I}}^{-1}, \tag{3.15}$$

$$\mathbf{T}_{\mathfrak{I}}^{\mathbf{d}} : H^{\mathbf{d}}(T\widehat{\mathfrak{I}}) \longrightarrow H^{\mathbf{d}}(T\mathfrak{I}), \quad \mathbf{T}_{\mathfrak{I}}^{\mathbf{d}}(\widehat{\boldsymbol{V}}) := \frac{1}{\det \mathbf{J}_{\mathfrak{I}}}\mathbf{J}_{\mathfrak{I}}\widehat{\boldsymbol{V}} \circ \mathbf{T}_{\mathfrak{I}}^{-1}. \tag{3.16}$$

For a $\binom{2}{0}$-tensor $\boldsymbol{T}$, one calculates the Piola transformations separately for each row:

$$\mathbf{T}_{\mathfrak{I}}^{\mathbf{c}}(\boldsymbol{T}) = \begin{bmatrix} \mathbf{T}_{\mathfrak{I}}^{\mathbf{c}}(\overrightarrow{\boldsymbol{T}}_1)^{\mathsf{T}} \\ \mathbf{T}_{\mathfrak{I}}^{\mathbf{c}}(\overrightarrow{\boldsymbol{T}}_2)^{\mathsf{T}} \end{bmatrix}, \quad \mathbf{T}_{\mathfrak{I}}^{\mathbf{d}}(\boldsymbol{T}) = \begin{bmatrix} \mathbf{T}_{\mathfrak{I}}^{\mathbf{d}}(\overrightarrow{\boldsymbol{T}}_1)^{\mathsf{T}} \\ \mathbf{T}_{\mathfrak{I}}^{\mathbf{d}}(\overrightarrow{\boldsymbol{T}}_2)^{\mathsf{T}} \end{bmatrix}. \tag{3.17}$$

The Piola mapping $\mathbf{T}_{\mathfrak{I}}^{\mathbf{c}}$ is an isomorphism of $H^{\mathbf{c}}(T\widehat{\mathfrak{I}})$ onto $H^{\mathbf{c}}(T\mathfrak{I})$, and the Piola mapping $\mathbf{T}_{\mathfrak{I}}^{\mathbf{d}}$ is an isomorphism of $H^{\mathbf{d}}(T\widehat{\mathfrak{I}})$ onto $H^{\mathbf{d}}(T\mathfrak{I})$. This and other useful properties of these mappings can be summarized in the following Lemma.

Lemma 9. *Using the numbering scheme discussed above, assume that $\mathfrak{I} = \mathbf{T}_{\mathfrak{I}}(\widehat{\mathfrak{I}})$ is an arbitrary element with edge lengths ℓ_k, unit tangent vectors $\mathbf{t}_k$, and unit normal vectors $\mathbf{n}_k$. Let $\widehat{\boldsymbol{V}} \in H^{\mathbf{c}}(T\widehat{\mathfrak{I}})$ and $\widehat{\boldsymbol{U}} \in H^{\mathbf{d}}(T\widehat{\mathfrak{I}})$, and set $\boldsymbol{V} = \mathbf{T}_{\mathfrak{I}}^{\mathbf{c}}(\widehat{\boldsymbol{V}})$ and $\boldsymbol{U} = \mathbf{T}_{\mathfrak{I}}^{\mathbf{d}}(\widehat{\boldsymbol{U}})$. Also, assume that $q = \hat{q} \circ \mathbf{T}_{\mathfrak{I}}^{-1}$, where $\hat{q} \in C^0(\widehat{\mathfrak{I}})$. Define $\boldsymbol{v}_J = o_{\mathfrak{I}} \mathbf{T}_{\mathfrak{I}}^{\mathbf{d}}(\hat{\boldsymbol{v}}_J)$ and $\hat{p}_k(\hat{s}) := \sum_{i=0}^{n} a_i (\hat{s}/\hat{\ell}_k)^i$, and construct $p_k = \hat{p}_k \circ g_k^{-1}$ with $g_k(\hat{s}) = (\ell_k/\hat{\ell}_k)\hat{s}$. Recall the linear operators (2.1) and set $I = 1$, and note that operators with the hat symbol are written with respect to the reference element coordinates $\boldsymbol{\xi} = (\xi^1, \xi^2)$. The following relations hold:*

(i) $\int_{\mathfrak{I}} \langle \mathbf{c}(\boldsymbol{V}), q \rangle dA = o_{\mathfrak{I}} \int_{\widehat{\mathfrak{I}}} \langle \widehat{\mathbf{c}}(\widehat{\boldsymbol{V}}), \hat{q} \rangle d\hat{A}$, and $\int_{\mathfrak{I}} \langle \boldsymbol{V}, \mathbf{s}(q) \rangle dA = o_{\mathfrak{I}} \int_{\widehat{\mathfrak{I}}} \langle \widehat{\boldsymbol{V}}, \widehat{\mathbf{s}}(\hat{q}) \rangle d\hat{A}$,

(ii) $\int_{\mathfrak{I}} \langle \mathbf{div}(\boldsymbol{U}), q \rangle dA = o_{\mathfrak{I}} \int_{\widehat{\mathfrak{I}}} \langle \widehat{\mathbf{div}}(\widehat{\boldsymbol{U}}), \hat{q} \rangle d\hat{A}$, and $\int_{\mathfrak{I}} \langle \boldsymbol{U}, \mathbf{grad}(q) \rangle dA = o_{\mathfrak{I}} \int_{\widehat{\mathfrak{I}}} \langle \widehat{\boldsymbol{U}}, \widehat{\mathbf{grad}}(\hat{q}) \rangle d\hat{A}$,

(iii) $\int_{\mathcal{E}_k} p_k \langle \boldsymbol{V}, \mathbf{t}_k \rangle ds = \int_{\widehat{\mathcal{E}}_k} \hat{p}_k \langle \widehat{\boldsymbol{V}}, \hat{\mathbf{t}}_k \rangle d\hat{s}$, and $\int_{\mathfrak{I}} \langle \boldsymbol{V}, \boldsymbol{v}_J \rangle dA = \int_{\widehat{\mathfrak{I}}} \langle \widehat{\boldsymbol{V}}, \hat{\boldsymbol{v}}_J \rangle d\hat{A}$,

(iv) $\int_{\mathcal{E}_k} p_k \langle \boldsymbol{U}, \mathbf{n}_k \rangle ds = \int_{\widehat{\mathcal{E}}_k} \hat{p}_k \langle \widehat{\boldsymbol{U}}, \hat{\mathbf{n}}_k \rangle d\hat{s}$, and $\int_{\mathfrak{I}} \langle \boldsymbol{U}, \mathbf{R}\boldsymbol{v}_J \rangle dA = \int_{\widehat{\mathfrak{I}}} \langle \widehat{\boldsymbol{U}}, \mathbf{R}\hat{\boldsymbol{v}}_J \rangle d\hat{A}$,

(v) $\int_{\mathfrak{I}} \langle \boldsymbol{U}, \boldsymbol{V} \rangle dA = o_{\mathfrak{I}} \int_{\widehat{\mathfrak{I}}} \langle \widehat{\boldsymbol{U}}, \widehat{\boldsymbol{V}} \rangle d\hat{A}$.

Proof. The second identities in (*iii*) and (*v*) can be derived directly form the assumptions. Other identities are the consequences of the following relations:

(i) $\mathbf{c}(\boldsymbol{V}) = \frac{1}{\det \mathbf{J}_{\mathfrak{I}}}\widehat{\mathbf{c}}(\widehat{\boldsymbol{V}}) \circ \mathbf{T}_{\mathfrak{I}}^{-1}$, and $\mathbf{s}(q) = \frac{1}{\det \mathbf{J}_{\mathfrak{I}}}\mathbf{J}_{\mathfrak{I}}\widehat{\mathbf{s}}(\hat{q}) \circ \mathbf{T}_{\mathfrak{I}}^{-1}$,

(ii) $\mathbf{div}\,\boldsymbol{U} = \frac{1}{\det \mathbf{J}_{\mathfrak{I}}}\widehat{\mathbf{div}}\,\widehat{\boldsymbol{U}} \circ \mathbf{T}_{\mathfrak{I}}^{-1}$, and $\mathbf{grad}(q) = \mathbf{J}_{\mathfrak{I}}^{-\mathsf{T}}\widehat{\mathbf{grad}}(\hat{q}) \circ \mathbf{T}_{\mathfrak{I}}^{-1}$,

(iii) $\mathbf{t}_k = \frac{\hat{\ell}_k}{\ell_k}\mathbf{J}_{\mathfrak{I}}\hat{\mathbf{t}}_k$,

(iv) $\mathbf{n}_k = \frac{\hat{\ell}_k}{\ell_k}(\det \mathbf{J}_{\mathfrak{I}})\mathbf{J}_{\mathfrak{I}}^{-\mathsf{T}}\hat{\mathbf{n}}_k$, and $\frac{1}{\det \mathbf{J}_{\mathfrak{I}}}\mathbf{R}\mathbf{J}_{\mathfrak{I}} = \mathbf{J}_{\mathfrak{I}}^{-\mathsf{T}}\mathbf{R}$. $\quad\square$

Consider the two reference finite elements for displacement gradient $\left(\widehat{\mathfrak{I}}, \mathcal{P}_r(\otimes^2 T\widehat{\mathfrak{I}}), \Sigma^{\widehat{\mathfrak{I}},\mathbf{c}}\right)$ and $\left(\widehat{\mathfrak{I}}, \mathcal{P}_r^-(\otimes^2 T\widehat{\mathfrak{I}}), \Sigma^{\widehat{\mathfrak{I}},\mathbf{c}-}\right)$. Let $V(\widehat{\mathfrak{I}}) = H^{\mathbf{c}}(\widehat{\mathfrak{I}})$ and $V(\mathfrak{I}) = H^{\mathbf{c}}(\mathfrak{I})$, and use the Piola mapping (3.15), and relation (3.17)$_1$. Then, based on Proposition 8, construct two families of finite elements $\left\{\left(\mathfrak{I}, \mathcal{P}_r(\otimes^2 T\mathfrak{I}), \Sigma^{\mathfrak{I},\mathbf{c}}\right)\right\}_{\mathfrak{I}\in\mathcal{B}_h}$ and $\left\{\left(\mathfrak{I}, \mathcal{P}_r^-(\otimes^2 T\mathfrak{I}), \Sigma^{\mathfrak{I},\mathbf{c}-}\right)\right\}_{\mathfrak{I}\in\mathcal{B}_h}$. The local shape functions are $\bar{\boldsymbol{r}}_{I,J}^{\mathfrak{I},\mathcal{E}_k} = \mathbf{T}_{\mathfrak{I}}^{\mathbf{c}}\left(\bar{\boldsymbol{r}}_{I,J}^{\widehat{\mathfrak{I}},\widehat{\mathcal{E}}_k}\right)$, $\boldsymbol{r}_{I,J}^{\mathfrak{I},\mathfrak{I}} = \mathbf{T}_{\mathfrak{I}}^{\mathbf{c}}\left(\boldsymbol{r}_{I,J}^{\widehat{\mathfrak{I}},\widehat{\mathfrak{I}}}\right)$, and the local degrees of freedom read $\phi_{I,J}^{\mathfrak{I},\mathcal{E}_k}(\boldsymbol{T}) = \left(\phi_{I,J}^{\widehat{\mathfrak{I}},\widehat{\mathcal{E}}_k} \circ \mathbf{T}_{\mathfrak{I}}^{\mathbf{c}-1}\right)(\boldsymbol{T})$ and $\phi_{I,J}^{\mathfrak{I},\mathfrak{I}}(\boldsymbol{T}) = \left(\phi_{I,J}^{\widehat{\mathfrak{I}},\widehat{\mathfrak{I}}} \circ \mathbf{T}_{\mathfrak{I}}^{\mathbf{c}-1}\right)(\boldsymbol{T})$. Lemma 9, (*iii*) implies that $\phi_{I,J}^{\mathfrak{I},\mathcal{E}_k}$ and $\phi_{I,J}^{\mathfrak{I},\mathfrak{I}}$ are in fact (3.6) with all the hat symbols removed.

Similarly, by using the Piola mapping (3.16), (3.17)$_2$, and Proposition 8 generate two families $\left\{\left(\mathfrak{I}, \mathcal{P}_r(\otimes^2 T\mathfrak{I}), \Sigma^{\mathfrak{I},\mathbf{d}}\right)\right\}_{\mathfrak{I}\in\mathcal{B}_h}$ and $\left\{\left(\mathfrak{I}, \mathcal{P}_r^\ominus(\otimes^2 T\mathfrak{I}), \Sigma^{\mathfrak{I},\mathbf{d}-}\right)\right\}_{\mathfrak{I}\in\mathcal{B}_h}$ from the two reference finite elements for stress $\left(\widehat{\mathfrak{I}}, \mathcal{P}_r(\otimes^2 T\widehat{\mathfrak{I}}), \Sigma^{\widehat{\mathfrak{I}},\mathbf{d}}\right)$ and $\left(\widehat{\mathfrak{I}}, \mathcal{P}_r^\ominus(\otimes^2 T\widehat{\mathfrak{I}}), \Sigma^{\widehat{\mathfrak{I}},\mathbf{d}-}\right)$. The local shape functions read $\bar{\boldsymbol{s}}_{I,J}^{\mathfrak{I},\mathcal{E}_k} = \mathbf{T}_{\mathfrak{I}}^{\mathbf{d}}\left(\bar{\boldsymbol{s}}_{I,J}^{\widehat{\mathfrak{I}},\widehat{\mathcal{E}}_k}\right)$, $\boldsymbol{s}_{I,J}^{\mathfrak{I},\mathfrak{I}} = \mathbf{T}_{\mathfrak{I}}^{\mathbf{d}}\left(\boldsymbol{s}_{I,J}^{\widehat{\mathfrak{I}},\widehat{\mathfrak{I}}}\right)$. Also, according to Lemma 9, (*iv*), the local degrees of freedom $\psi_{I,J}^{\mathfrak{I},\mathcal{E}_k}$, $\psi_{I,J}^{\mathfrak{I},\mathfrak{I}}$ are (3.10) without the hat symbols.

Recall the reference finite element of the pressure-like field $\left(\widehat{\mathfrak{I}}, \mathcal{P}_r(\widehat{\mathfrak{I}}), \Sigma^{\widehat{\mathfrak{I}},\ell}\right)$. Set $V(\widehat{\mathfrak{I}}) = L^2(\widehat{\mathfrak{I}})$ and $V(\mathfrak{I}) = L^2(\mathfrak{I})$. Then, use the mapping

$$\mathbf{T}_{\mathfrak{I}}^{\ell} : L^2(\widehat{\mathfrak{I}}) \longrightarrow L^2(\mathfrak{I}), \quad \mathbf{T}_{\mathfrak{I}}^{\ell}(\hat{f}) := \hat{f} \circ \mathbf{T}_{\mathfrak{I}}^{-1}. \tag{3.18}$$

and Proposition 8 to generate $\left\{\left(\mathfrak{I}, \mathcal{P}_r(\mathfrak{I}), \Sigma^{\mathfrak{I},\ell}\right)\right\}_{\mathfrak{I}\in\mathcal{B}_h}$. The local shape functions become $t_i^{\mathfrak{I}} = \mathbf{T}_{\mathfrak{I}}^{\ell}(t_i^{\widehat{\mathfrak{I}}})$, and by recalling (3.11), it is straightforward to show that the local degrees of freedom are $\omega_i^{\mathfrak{I}}(f) = \frac{1}{A}\int_{\mathfrak{I}} p_i^r f\, dA$, where $p_i^r = \hat{p}_i^r \circ \mathbf{T}_{\mathfrak{I}}^{-1}$.

3.2. Finite element spaces

In order to define suitable conforming finite element spaces, we first define the following notions of jump across the edges of a 2D mesh for vector and tensor fields. We denote the set of all interior edges of the mesh by $\mathcal{E}_h^i$. For an edge $\mathcal{E} \in \mathcal{E}_h^i$, there exist two elements $\mathcal{T}, \mathcal{T}' \in \mathcal{B}_h$ such that $\mathcal{E} = \mathcal{T} \cap \mathcal{T}'$. Also, let $\mathbf{n}$ be the unit normal vector of $\mathcal{E}$ such that it points from $\mathcal{T}$ to $\mathcal{T}'$. Let $\boldsymbol{V}$ be a vector-valued function and $\boldsymbol{T}$ a tensor-valued function that are both defined on $\mathcal{B}_h$ and have limits on both sides of the edge $\mathcal{E}$. We define the jump of $\boldsymbol{V}$ across $\mathcal{E}$ as

$$\llbracket \boldsymbol{V} \rrbracket_{\mathcal{E}} := \boldsymbol{V}_{\mathcal{T}'} - \boldsymbol{V}_{\mathcal{T}},$$

where $\boldsymbol{V}_{\mathcal{T}} = \boldsymbol{V}|_{\mathcal{T}}$ and $\boldsymbol{V}_{\mathcal{T}'} = \boldsymbol{V}|_{\mathcal{T}'}$. Recall that $\mathbf{t} = \mathbf{R}^{\mathsf{T}}\mathbf{n}$ is the unit tangent of $\mathcal{E}$ and set $\boldsymbol{T}_{\mathcal{T}} = \boldsymbol{T}|_{\mathcal{T}}$ and $\boldsymbol{T}_{\mathcal{T}'} = \boldsymbol{T}|_{\mathcal{T}'}$. Then, the jump of the tangent traction and the normal traction of $\boldsymbol{T}$ across $\mathcal{E}$ are defined as

$$\llbracket \mathbf{t}\boldsymbol{T} \rrbracket_{\mathcal{E}} := (\boldsymbol{T}_{\mathcal{T}'} - \boldsymbol{T}_{\mathcal{T}})\,\mathbf{t},$$

$$\llbracket \mathbf{n}\boldsymbol{T} \rrbracket_{\mathcal{E}} := (\boldsymbol{T}_{\mathcal{T}'} - \boldsymbol{T}_{\mathcal{T}})\,\mathbf{n}.$$

Note that all the above jumps are vector-valued functions in 2D and their domain is the set of interior edges of the mesh.

We are now in a position to define the following finite element spaces:

$$V_{h,r}^1 := \left\{ \boldsymbol{V}_h \in L^2(T\mathcal{B}_h) : \forall \mathcal{T} \in \mathcal{B}_h, \ \boldsymbol{V}_h|_{\mathcal{T}} \in \mathcal{P}_r(T\mathcal{T}), \ \forall \mathcal{E} \in \mathcal{E}_h^i, \ \llbracket \boldsymbol{V}_h \rrbracket_{\mathcal{E}} = \mathbf{0} \right\},$$

$$V_{h,r}^{\mathbf{c}-} := \left\{ \boldsymbol{T}_h \in L^2(\otimes^2 T\mathcal{B}_h) : \forall \mathcal{T} \in \mathcal{B}_h, \ \boldsymbol{T}_h|_{\mathcal{T}} \in \mathcal{P}_r^-(\otimes^2 T\mathcal{T}), \ \forall \mathcal{E} \in \mathcal{E}_h^i, \ \llbracket \mathbf{t}\boldsymbol{T}_h \rrbracket_{\mathcal{E}} = \mathbf{0} \right\},$$

$$V_{h,r}^{\mathbf{c}} := \left\{ \boldsymbol{T}_h \in L^2(\otimes^2 T\mathcal{B}_h) : \forall \mathcal{T} \in \mathcal{B}_h, \ \boldsymbol{T}_h|_{\mathcal{T}} \in \mathcal{P}_r(\otimes^2 T\mathcal{T}), \ \forall \mathcal{E} \in \mathcal{E}_h^i, \ \llbracket \mathbf{t}\boldsymbol{T}_h \rrbracket_{\mathcal{E}} = \mathbf{0} \right\},$$

$$V_{h,r}^{\mathbf{d}-} := \left\{ \boldsymbol{T}_h \in L^2(\otimes^2 T\mathcal{B}_h) : \forall \mathcal{T} \in \mathcal{B}_h, \ \boldsymbol{T}_h|_{\mathcal{T}} \in \mathcal{P}_r^{\ominus}(\otimes^2 T\mathcal{T}), \ \forall \mathcal{E} \in \mathcal{E}_h^i, \ \llbracket \mathbf{n}\boldsymbol{T}_h \rrbracket_{\mathcal{E}} = \mathbf{0} \right\},$$

$$V_{h,r}^{\mathbf{d}} := \left\{ \boldsymbol{T}_h \in L^2(\otimes^2 T\mathcal{B}_h) : \forall \mathcal{T} \in \mathcal{B}_h, \ \boldsymbol{T}_h|_{\mathcal{T}} \in \mathcal{P}_r(\otimes^2 T\mathcal{T}), \ \forall \mathcal{E} \in \mathcal{E}_h^i, \ \llbracket \mathbf{n}\boldsymbol{T}_h \rrbracket_{\mathcal{E}} = \mathbf{0} \right\},$$

$$V_{h,r}^{\ell} := \left\{ f_h \in L^2(\mathcal{B}_h) : \forall \mathcal{T} \in \mathcal{B}_h, \ f_h|_{\mathcal{T}} \in \mathcal{P}_r(\mathcal{T}) \right\}.$$

In addition, let $\check{V}_{h,r}^{\mathbf{c}}$ be either $V_{h,r}^{\mathbf{c}-}$ or $V_{h,r}^{\mathbf{c}}$, and let $\check{V}_{h,r}^{\mathbf{d}}$ be either $V_{h,r}^{\mathbf{d}-}$ or $V_{h,r}^{\mathbf{d}}$. The above spaces are conforming according to the following theorem.

Theorem 10. $V_{h,r}^1 \subset H^1(T\mathcal{B}_h)$, $\check{V}_{h,r}^{\mathbf{c}} \subset H^{\mathbf{c}}(\mathcal{B}_h)$, $\check{V}_{h,r}^{\mathbf{d}} \subset H^{\mathbf{d}}(\mathcal{B}_h)$, and $V_{h,r}^{\ell} \subset L^2(\mathcal{B}_h)$.

Proof. $V_{h,r}^{\ell} \subset L^2(\mathcal{B}_h)$ is trivial. For proof of $V_{h,r}^1 \subset H^1(T\mathcal{B}_h)$ see [26, Proposition 1.74]. $\check{V}_{h,r}^{\mathbf{c}} \subset H^{\mathbf{c}}(\mathcal{B}_h)$ and $\check{V}_{h,r}^{\mathbf{d}} \subset H^{\mathbf{d}}(\mathcal{B}_h)$ can be proved similarly by following the steps of the proof for $V_{h,r}^1 \subset H^1(T\mathcal{B}_h)$ and recalling the distributional definitions of the operators $\mathbf{c}$ and $\mathbf{div}$ and the Green's formulas (2.9) and

$$\langle\!\langle \mathbf{c}(\boldsymbol{M}), \boldsymbol{V} \rangle\!\rangle = \langle\!\langle \boldsymbol{M}, \mathbf{s}(\boldsymbol{V}) \rangle\!\rangle + \int_{\partial\mathcal{B}} \langle \boldsymbol{M}\boldsymbol{T}_{\partial\mathcal{B}}, \boldsymbol{V} \rangle ds,$$

where $\boldsymbol{M}$ is a $\binom{2}{0}$-tensor, $\boldsymbol{V}$ is a vector, and $\boldsymbol{T}_{\partial\mathcal{B}}$ is the oriented unit tangent vector field of $\partial\mathcal{B}$. $\square$

To interpolate the four field variables $(\boldsymbol{U}, \boldsymbol{K}, \boldsymbol{P}, p)$ over the entire mesh $\mathcal{B}_h$, we next define the global shape functions analogous to the local shape functions $\left(\left\{ \boldsymbol{h}_k^{\mathcal{T}} \right\}, \left\{ \bar{\boldsymbol{r}}_{I,J}^{\mathcal{T},\mathcal{E}_k}, \boldsymbol{r}_{I,J}^{\mathcal{T},\mathcal{T}} \right\}, \left\{ \bar{\boldsymbol{s}}_{I,J}^{\mathcal{T},\mathcal{E}_k}, \boldsymbol{s}_{I,J}^{\mathcal{T},\mathcal{T}} \right\}, \left\{ t_i^{\mathcal{T}} \right\} \right)$ of an element $\mathcal{T}$. Let $\boldsymbol{H}_I^{\mathcal{N}}$, $I = 1, 2$ denote the two global shape functions of each node $\mathcal{N} \in \mathcal{B}_h$. $\boldsymbol{H}^{\mathcal{N}}$ is defined on $\mathcal{B}_h$ such that

$$\boldsymbol{H}_I^{\mathcal{N}}\Big|_{\mathcal{T}} = \begin{cases} \boldsymbol{h}_{2(i-1)+I}^{\mathcal{T}}, & \text{if } \mathcal{N} \cap \mathcal{T} = \mathcal{N}_i, \\ \mathbf{0}_{2\times 1}, & \text{if } \mathcal{N} \cap \mathcal{T} = \emptyset, \end{cases} \quad \forall \mathcal{T} \in \mathcal{B}_h,$$

where $\mathcal{N}_i$ is i-th node of $\mathcal{T}$. Hence, the support of the function $\boldsymbol{H}_I^{\mathcal{N}}$ in its domain $\mathcal{B}_h$ is all those adjacent elements of $\mathcal{B}_h$ that share the node $\mathcal{N}$. Considering properties of the Lagrange polynomials, one can show that $\boldsymbol{H}_I^{\mathcal{N}}$ is continuous everywhere in $\mathcal{B}_h$, and hence $\boldsymbol{H}_I^{\mathcal{N}} \in V_{h,r}^1$. If we interpolate a vector-valued function on $\mathcal{B}_h$ by using $V_{h,r}^1$, the global degree of freedom associated with $\boldsymbol{H}_I^{\mathcal{N}}$ is the value of the I-th component of that vector-valued function at the node $\mathcal{N}$.
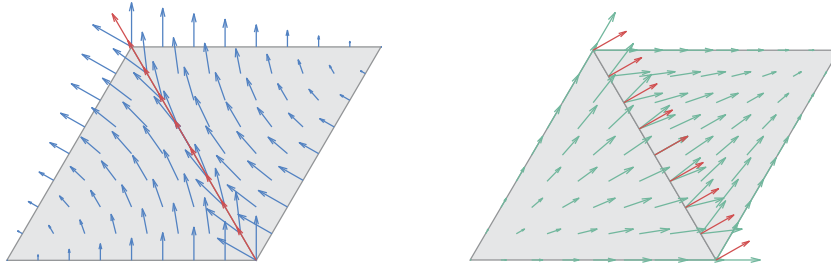
Fig. 3. The nonzero row of the global shape functions $\boldsymbol{R}_{1,1}^{\mathcal{E}} \in V_{h,1}^{\mathbf{c}-}$ (left) and $\boldsymbol{S}_{1,1}^{\mathcal{E}} \in V_{h,1}^{\mathbf{d}-}$ (right), where $\mathcal{E}$ is the common edge of the two adjacent elements. Observe that $\boldsymbol{S}_{1,1}^{\mathcal{E}} = \boldsymbol{R}_{1,1}^{\mathcal{E}} \mathsf{R}^{\mathsf{T}}$. The tangent (normal) components of the fields, which are shown with red arrows, are continuous across $\mathcal{E}$ in the left (right) plot. (For interpretation of the references to color in this figure legend, the reader is referred to the web version of this article.)

Let $\boldsymbol{R}_{I,J}^{\mathcal{E}}$, $\boldsymbol{R}_{I,J}^{\mathcal{T}}$ be the global shape functions corresponding to $\bar{\boldsymbol{r}}_{I,J}^{\mathcal{T},\mathcal{E}_k}$, $\boldsymbol{r}_{I,J}^{\mathcal{T},\mathcal{T}}$. We define them on $\mathcal{B}_h$ such that

$$\boldsymbol{R}_{I,J}^{\mathcal{E}}\Big|_{\mathcal{T}} = \begin{cases} \bar{\boldsymbol{r}}_{I,J}^{\mathcal{T},\mathcal{E}_k}, & \text{if } \mathcal{E} \cap \mathcal{T} = \mathcal{E}_k, \\ \mathbf{0}_{2\times 2}, & \text{if } \mathcal{E} \cap \mathcal{T} = \emptyset, \end{cases} \quad \forall \mathcal{T} \in \mathcal{B}_h, \quad \text{and} \quad \boldsymbol{R}_{I,J}^{\mathcal{T}} = \begin{cases} \boldsymbol{r}_{I,J}^{\mathcal{T},\mathcal{T}}, & \text{on } \mathcal{T}, \\ \mathbf{0}_{2\times 2}, & \text{otherwise.} \end{cases}$$

Note that $\mathcal{E}_k$ is an edge of $\mathcal{T}$ and $k \in \{1, 2, 3\}$ is its local numbering in $\mathcal{T}$. If $\mathcal{E}$ is an exterior edge, i.e., $\mathcal{E} \in \partial \mathcal{B}_h$, the support of $\boldsymbol{R}_{I,J}^{\mathcal{E}}$ in $\mathcal{B}_h$ is only one element that contains $\mathcal{E}$, and if $\mathcal{E}$ is an interior edge, the support of $\boldsymbol{R}_{I,J}^{\mathcal{E}}$ are two adjacent elements that have $\mathcal{E}$ in common. Let $L^{\mathcal{E}}$ be the union of the support boundaries of $\boldsymbol{R}_{I,J}^{\mathcal{E}}$ and the corresponding edge $\mathcal{E}$, and let $\mathbf{t}_L$ be the unit tangent vector field on $L^{\mathcal{E}}$. On $L^{\mathcal{E}}$ the function $\boldsymbol{R}_{I,J}^{\mathcal{E}}$ is multi-valued. However, $\boldsymbol{R}_{I,J}^{\mathcal{E}}\mathbf{t}_L$ is continuous (single-valued) across $L^{\mathcal{E}}$. Here, we emphasize that the above description of $\boldsymbol{R}_{I,J}^{\mathcal{E}}$ is valid if we use the numbering scheme discussed in Section 3.1. The support of the global shape function $\boldsymbol{R}_{I,J}^{\mathcal{T}}$ in $\mathcal{B}_h$ is the corresponding element $\mathcal{T}$. $\boldsymbol{R}_{I,J}^{\mathcal{T}}$ is multi-valued on $\partial \mathcal{T}$ while $\boldsymbol{R}_{I,J}^{\mathcal{T}}\mathbf{t}_{\partial \mathcal{T}}$ is continuous across $\partial \mathcal{T}$. Based on the above discussion, one can conclude that $[\![\mathsf{t}\boldsymbol{R}_{I,J}^{\mathcal{E}}]\!]_{\mathcal{E}'} = \mathbf{0}$ and $[\![\mathsf{t}\boldsymbol{R}_{I,J}^{\mathcal{T}}]\!]_{\mathcal{E}'} = \mathbf{0}$, $\forall \mathcal{E}' \in \mathcal{B}_h$, and hence $\boldsymbol{R}_{I,J}^{\mathcal{E}}, \boldsymbol{R}_{I,J}^{\mathcal{T}} \in \check{V}_{h,r}^{\mathbf{c}}$. Let us now define the global degrees of freedom. Suppose $\mathcal{T}$ and $\mathcal{T}'$ are adjacent in $\mathcal{B}_h$ such that their common edge $\mathcal{E}$ is numbered $\mathcal{E}_k$ in $\mathcal{T}$ and $\mathcal{E}_{k'}$ in $\mathcal{T}'$, where k is not necessary equal to k'. The numbering scheme of Section 3.1 guarantees that $\phi_{I,J}^{\mathcal{T},\mathcal{E}_k} = \phi_{I,J}^{\mathcal{T}',\mathcal{E}_{k'}}$, $\forall I, J$. This equivalence enables one to use either of them for calculating the global degrees of freedom for $\mathcal{E}$ (this is also necessary for the assembly of finite elements). Therefore, it is well-defined to write $\Phi_{I,J}^{\mathcal{E}} : \check{V}_{h,r}^{\mathbf{c}} \longrightarrow \mathbb{R}$, $\Phi_{I,J}^{\mathcal{E}}(\boldsymbol{T}_h) := \phi_{I,J}^{\mathcal{T},\mathcal{E}_k}(\boldsymbol{T}_h|_{\mathcal{T}})$ as the global degree of freedom associated with $\boldsymbol{R}_{I,J}^{\mathcal{E}}$. Also, the global degree of freedom associated with $\boldsymbol{R}_{I,J}^{\mathcal{T}}$ is $\Phi_{I,J}^{\mathcal{T}} : \check{V}_{h,r}^{\mathbf{c}} \longrightarrow \mathbb{R}$, $\Phi_{I,J}^{\mathcal{T}}(\boldsymbol{T}_h) := \phi_{I,J}^{\mathcal{T},\mathcal{T}}(\boldsymbol{T}_h|_{\mathcal{T}})$. Note that $\Phi_{I,J}^{\mathcal{E}}, \Phi_{I,J}^{\mathcal{T}} \in (\check{V}_{h,r}^{\mathbf{c}})^{\star}$, but they can be extended to $H^{\mathbf{c}}(\mathcal{B}_h)^{\star}$.

Similarly, one can define the global shape functions $\boldsymbol{S}_{I,J}^{\mathcal{E}}$, $\boldsymbol{S}_{I,J}^{\mathcal{T}}$ and the global degrees of freedom $\Psi_{I,J}^{\mathcal{E}}, \Psi_{I,J}^{\mathcal{T}}$ based on the corresponding local shape functions $\bar{\boldsymbol{s}}_{I,J}^{\mathcal{T},\mathcal{E}_k}$, $\boldsymbol{s}_{I,J}^{\mathcal{T},\mathcal{T}}$ and degrees of freedom $\psi_{I,J}^{\mathcal{T},\mathcal{E}_k}$, $\psi_{I,J}^{\mathcal{T},\mathcal{T}}$. One can also obtain the global shape functions directly as $\boldsymbol{S}_{I,J}^{\mathcal{E}} = \boldsymbol{R}_{I,J}^{\mathcal{E}}\mathsf{R}^{\mathsf{T}}$ and $\boldsymbol{S}_{I,J}^{\mathcal{T}} = \boldsymbol{R}_{I,J}^{\mathcal{T}}\mathsf{R}^{\mathsf{T}}$. Therefore, $[\![\mathsf{n}\boldsymbol{S}_{I,J}^{\mathcal{E}}]\!]_{\mathcal{E}'} = \mathbf{0}$ and $[\![\mathsf{n}\boldsymbol{S}_{I,J}^{\mathcal{T}}]\!]_{\mathcal{E}'} = \mathbf{0}$, $\forall \mathcal{E}' \in \mathcal{B}_h$, and $\boldsymbol{S}_{I,J}^{\mathcal{E}}, \boldsymbol{S}_{I,J}^{\mathcal{T}} \in \check{V}_{h,r}^{\mathbf{d}}$. In Fig. 3, we illustrate the first (nonzero) rows of $\boldsymbol{R}_{1,1}^{\mathcal{E}} \in V_{h,1}^{\mathbf{c}-}$ and $\boldsymbol{S}_{1,1}^{\mathcal{E}} \in V_{h,1}^{\mathbf{d}-}$ on their supports. See $\boldsymbol{v}_2^{\widehat{\mathcal{T}},\widehat{\mathcal{T}}}$ and $\boldsymbol{v}_3^{\widehat{\mathcal{T}},\widehat{\mathcal{T}}}$ in Fig. 2 for some examples of nonzero rows of $\boldsymbol{R}_{I,J}^{\mathcal{T}}$ on its support.

To define the global shape function analogous to $t_i^{\mathcal{T}}$, consider the function $T_i^{\mathcal{T}}$ on $\mathcal{B}_h$ with support $\mathcal{T}$ such that $T_i^{\mathcal{T}} = t_i^{\mathcal{T}}$ on $\mathcal{T}$. It is straightforward to show that $T_i^{\mathcal{T}} \in V_{h,r}^{\ell}$. For interpolating a scaler field f on $\mathcal{B}_h$ using $V_{h,r}^{\ell}$, one simply uses $\omega_i^{\mathcal{T}}(f|_{\mathcal{T}})$ as the global degree of freedom associate with $T_i^{\mathcal{T}}$.

Theorem 11. $\left\{ \boldsymbol{H}_I^{\mathcal{N}} \right\}_{\mathcal{N} \in \mathcal{B}_h}$ *is a basis for* $V_{h,r}^1$, $\left\{ \boldsymbol{R}_{I,J}^{\mathcal{E}}, \boldsymbol{R}_{I,J}^{\mathcal{T}} \right\}_{\mathcal{E},\mathcal{T} \in \mathcal{B}_h}$ *is a basis for* $\check{V}_{h,r}^{\mathbf{c}}$, $\left\{ \boldsymbol{S}_{I,J}^{\mathcal{E}}, \boldsymbol{S}_{I,J}^{\mathcal{T}} \right\}_{\mathcal{E},\mathcal{T} \in \mathcal{B}_h}$ *is a basis for* $\check{V}_{h,r}^{\mathbf{d}}$, *and* $\left\{ T_i^{\mathcal{T}} \right\}_{\mathcal{T} \in \mathcal{B}_h}$ *is a basis for* $V_{h,r}^{\ell}$.

Proof. See [26, Lemma 1.77 and Proposition 1.78] for the proof of the first statement. The other three statements can be proved similarly considering [26, Lemma 1.86, Proposition 1.87, Lemma 1.92, and Proposition 1.93]. □

3.3. Compatible-strain mixed finite element methods

Using the approximation spaces defined in the previous section, one writes the following mixed finite element methods for (2.8):
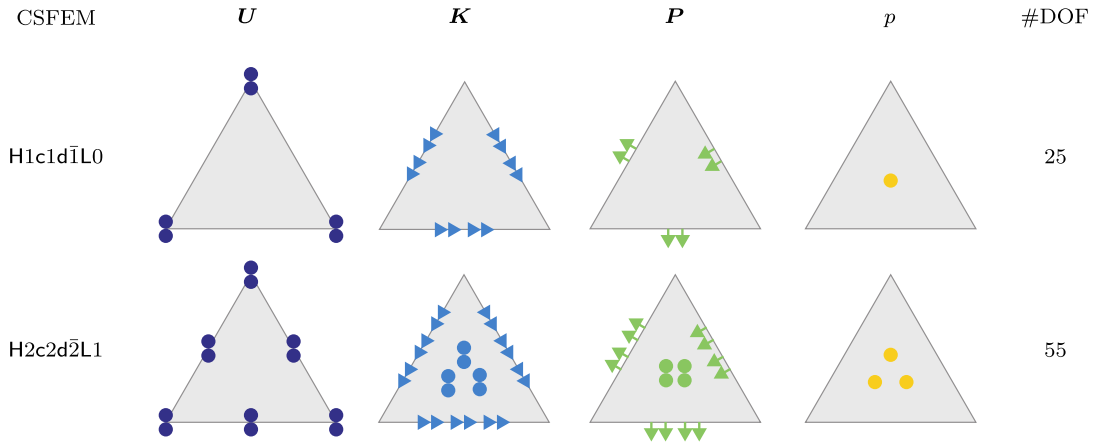
CSFEM	U	K	P	p	#DOF
H1c1d$\bar{1}$L0					25
H2c2d$\bar{2}$L1					55

Fig. 4. The schematic diagrams for some first-order and second-order mixed finite elements.

Given a body force B of L^2-class, a boundary displacement $\overline{U}$ on Γ_d of $H^{1/2}$-class, and a boundary traction $\overline{T}$ on Γ_t of L^2-class, find $(U_h, K_h, P_h, p_h) \in V^1_{h,m}(\Gamma_d, \overline{U}) \times \check{V}^{\mathbf{c}}_{h,n} \times \check{V}^{\mathbf{d}}_{h,r} \times V^{\ell}_{h,s}$ *such that*

$$\langle\langle P_h, \mathbf{grad}\, \Upsilon_h \rangle\rangle = \langle\langle \rho_0 B, \Upsilon_h \rangle\rangle + \int_{\Gamma_t} \langle \overline{T}, \Upsilon_h \rangle ds, \quad \forall \Upsilon_h \in V^1_{h,m}(\Gamma_d),$$

$$\langle\langle \widetilde{P}(K_h), \kappa_h \rangle\rangle - \langle\langle P_h, \kappa_h \rangle\rangle + \langle\langle p_h\, Q\,(K_h), \kappa_h \rangle\rangle = 0, \qquad \forall \kappa_h \in \check{V}^{\mathbf{c}}_{h,n}, \tag{3.19}$$

$$\langle\langle \mathbf{grad}\, U_h, \pi_h \rangle\rangle - \langle\langle K_h, \pi_h \rangle\rangle = 0, \qquad \forall \pi_h \in \check{V}^{\mathbf{d}}_{h,r},$$

$$\langle\langle C(J_h), q_h \rangle\rangle = 0, \qquad \forall q_h \in V^{\ell}_{h,s}.$$

Remark 12 *(Compatibility of strain and continuity of traction).*

(*i*) Let K_h be a displacement gradient field on $\mathcal{B}_h$. The zero jump $[\![\mathrm{t} K_h]\!]_{\mathcal{E}} = 0$ is known as the Hadamard jump condition along the edge $\mathcal{E}$. If $K_h \in \check{V}^{\mathbf{c}}_{h,r} \subset H^{\mathbf{c}}(\mathcal{B}_h)$, the Hadamard jump condition is satisfied for all the internal edges of $\mathcal{B}_h$ independently of the refinement level of the mesh. This is a necessary compatibility condition for the existence of a displacement field $U_h \in H^1(T\mathcal{B}_h)$ (continuous along edges) such that $K_h = \mathbf{grad}\, U_h$ [35].

(*ii*) Suppose P_h is a stress field on $\mathcal{B}_h$. The zero jump condition $[\![\mathrm{n} P_h]\!]_{\mathcal{E}} = 0$ indicates that traction vector associated with P_h is continuous across the edge $\mathcal{E}$. If $P_h \in \check{V}^{\mathbf{d}}_{h,r} \subset H^{\mathbf{d}}(\mathcal{B}_h)$, the continuity of traction holds for all the internal edges of $\mathcal{B}_h$ independently of the refinement level of the mesh. This is required by localization of the balance of linear momentum.

Inspired by Remark 12 (i), we call the finite element methods introduced in (3.19) the *compatible-strain mixed finite element methods* (CSFEMs). We also use the following notation for referring to (3.19):

$$\text{H}mc n(\bar{n})\text{d}r(\bar{r})\text{L}s \quad \text{in the case of} \quad V^1_{h,m} \times V^{\mathbf{c}}_{h,n}(V^{\mathbf{c}-}_{h,n}) \times V^{\mathbf{d}}_{h,r}(V^{\mathbf{d}-}_{h,r}) \times V^{\ell}_{h,s},$$

where $m, n, r = 1, 2$ and $s = 0, 1, 2$. This results in 96 possible choices of CSFEMs. However, since (3.19) corresponds to a saddle point of a variational problem (see Remark 4) not all these choices lead to convergent (consistent and stable) methods as the solution and test spaces need to satisfy certain conditions. We will discuss this further in Section 3.5 and in the first numerical example. We will conclude that the well-performing choices of CSFEMs among the first and second-order elements are H1c1d$\bar{1}$L0 and H2c2d$\bar{2}$L1. The schematic diagrams of these two cases are given in Fig. 4.

3.4. Matrix formulation

In this section, we focus on the implementation of CSFEMs. In particular, we discuss how to represent (3.19) as a nonlinear system of algebraic (polynomial) equations, which can be solved using Newton's method. We define the vector representation of a second-order tensor T and the matrix representation of a vector V with 4 entries by

$$\lceil T \rceil := \begin{bmatrix} T^{11} & T^{12} & T^{21} & T^{22} \end{bmatrix}^{\mathsf{T}} \quad \text{and} \quad [V] := \begin{bmatrix} V^1 & V^2 \\ V^3 & V^4 \end{bmatrix}.$$

One can show that $\langle\langle \boldsymbol{Y}, \boldsymbol{Z} \rangle\rangle = \langle\langle \lceil \boldsymbol{Y} \rceil, \lceil \boldsymbol{Z} \rceil \rangle\rangle = \int_{\mathcal{B}} \lceil \boldsymbol{Y} \rceil^{\mathsf{T}} \lceil \boldsymbol{Z} \rceil \, dA = \int_{\mathcal{B}} \lceil \boldsymbol{Z} \rceil^{\mathsf{T}} \lceil \boldsymbol{Y} \rceil \, dA$. Let $\lceil \check{V}_{h,r}^{\mathbf{c}} \rceil := \{ \lceil \boldsymbol{T}_h \rceil : \boldsymbol{T}_h \in \check{V}_{h,r}^{\mathbf{c}} \}$ and define $\lceil \check{V}_{h,r}^{\mathbf{d}} \rceil$ similarly. Then, (3.19) can be rewritten as

Find $(\boldsymbol{U}_h, \lceil \boldsymbol{K}_h \rceil, \lceil \boldsymbol{P}_h \rceil, p_h) \in V_{h,m}^1(\Gamma_d, \overline{\boldsymbol{U}}) \times \lceil \check{V}_{h,n}^{\mathbf{c}} \rceil \times \lceil \check{V}_{h,r}^{\mathbf{d}} \rceil \times V_{h,s}^\ell$ *such that*

$$
\begin{aligned}
&\int_{\mathcal{B}_h} \lceil \mathbf{grad}\, \Upsilon_h \rceil^{\mathsf{T}} \lceil \boldsymbol{P}_h \rceil \, dA - \int_{\mathcal{B}_h} \rho_0 \Upsilon_h^{\mathsf{T}} \boldsymbol{B} \, dA - \int_{\Gamma_t} \Upsilon_h^{\mathsf{T}} \overline{\boldsymbol{T}} \, ds = 0, && \forall \Upsilon_h \in V_{h,m}^1(\Gamma_d), \\[4pt]
&\int_{\mathcal{B}_h} \lceil \boldsymbol{\kappa}_h \rceil^{\mathsf{T}} \left(\lceil \widetilde{\boldsymbol{P}}(\boldsymbol{K}_h) \rceil + p_h \lceil \boldsymbol{Q}\,(\boldsymbol{K}_h) \rceil \right) dA - \int_{\mathcal{B}_h} \lceil \boldsymbol{\kappa}_h \rceil^{\mathsf{T}} \lceil \boldsymbol{P}_h \rceil \, dA = 0, && \forall \lceil \boldsymbol{\kappa}_h \rceil \in \lceil \check{V}_{h,n}^{\mathbf{c}} \rceil, \\[4pt]
&\int_{\mathcal{B}_h} \lceil \boldsymbol{\pi}_h \rceil^{\mathsf{T}} \lceil \mathbf{grad}\, \boldsymbol{U}_h \rceil \, dA - \int_{\mathcal{B}_h} \lceil \boldsymbol{\pi}_h \rceil^{\mathsf{T}} \lceil \boldsymbol{K}_h \rceil \, dA = 0, && \forall \lceil \boldsymbol{\pi}_h \rceil \in \lceil \check{V}_{h,r}^{\mathbf{d}} \rceil, \\[4pt]
&\int_{\mathcal{B}_h} q_h \, C(J_h) \, dA = 0, && \forall q_h \in V_{h,s}^\ell.
\end{aligned}
\tag{3.20}
$$

The local shape functions are discussed in Section 3.1. Here, to be consistent with (3.20), we define the following vector representations of the local shape functions:

$$
\begin{aligned}
\mathbf{g}_{\mathcal{T},j}^1(\mathbf{X}) &:= \left\lceil \mathbf{grad}\, h_j^{\mathcal{T}}(\mathbf{X}) \right\rceil, \\
\mathbf{b}_{\mathcal{T},k}^{\mathbf{c}}(\mathbf{X}) &:= \left\lceil \bar{\boldsymbol{r}}_{I,J}^{\mathcal{T},\mathcal{E}_i}(\mathbf{X}) \right\rceil, & \mathbf{b}_{\mathcal{T},l}^{\mathbf{c}}(\mathbf{X}) &:= \left\lceil \boldsymbol{r}_{I,J}^{\mathcal{T},\mathcal{T}}(\mathbf{X}) \right\rceil, \\
\mathbf{b}_{\mathcal{T},k}^{\mathbf{d}}(\mathbf{X}) &:= \left\lceil \bar{\boldsymbol{s}}_{I,J}^{\mathcal{T},\mathcal{E}_i}(\mathbf{X}) \right\rceil, & \mathbf{b}_{\mathcal{T},l}^{\mathbf{d}}(\mathbf{X}) &:= \left\lceil \boldsymbol{s}_{I,J}^{\mathcal{T},\mathcal{T}}(\mathbf{X}) \right\rceil,
\end{aligned}
\tag{3.21}
$$

where $j = 1, 2, ..., 2r$ for $\boldsymbol{U}_h \in V_{h,r}^1$, and the numberings k and l are specified as

$$
k := I + 2(J - 1) + 2(i - 1)\max J, \quad l := I + 2(J - 1) + \max k,
\tag{3.22}
$$

where $i = 1, 2, 3$ and $I = 1, 2$. For $\boldsymbol{K}_h \in V_{h,1}^{\mathbf{c}-}$ and $\boldsymbol{P}_h \in V_{h,1}^{\mathbf{d}-}$, we have $J = 1$, using $V_{h,1}^{\mathbf{c}}$, $V_{h,2}^{\mathbf{c}-}$, $V_{h,1}^{\mathbf{d}}$, and $V_{h,2}^{\mathbf{d}-}$ we have $J = 1, 2$, and $J = 1, 2, 3$ for $V_{h,2}^{\mathbf{c}}$ and $V_{h,2}^{\mathbf{d}}$. Note that in (3.21), $\mathbf{b}_{\mathcal{T},l}^{\mathbf{d}}$ and $\mathbf{b}_{\mathcal{T},l}^{\mathbf{c}}$ are defined only for second or higher-order finite element spaces, i.e., $\check{V}_{h,r}^{\mathbf{c}}$ and $\check{V}_{h,r}^{\mathbf{d}}$ with $r \geq 2$. These relations can also be realized from Table 3. Let us write the following sparse matrices using the local shape functions of displacement and pressure and (3.21):

$$
\begin{aligned}
\mathbf{B}_{\mathcal{T}}^1 &= \begin{bmatrix} h_1^{\mathcal{T}} & h_2^{\mathcal{T}} & \cdots & h_{n^1}^{\mathcal{T}} \end{bmatrix}_{2 \times n^1}, \\
\mathbf{G}_{\mathcal{T}}^1 &= \begin{bmatrix} \mathbf{g}_{\mathcal{T},1}^1 & \mathbf{g}_{\mathcal{T},2}^1 & \cdots & \mathbf{g}_{\mathcal{T},n^1}^1 \end{bmatrix}_{4 \times n^1}, \\
\mathbf{B}_{\mathcal{T}}^{\mathbf{c}} &= \begin{bmatrix} \mathbf{b}_{\mathcal{T},1}^{\mathbf{c}} & \mathbf{b}_{\mathcal{T},2}^{\mathbf{c}} & \cdots & \mathbf{b}_{\mathcal{T},n^c}^{\mathbf{c}} \end{bmatrix}_{4 \times n^c}, \\
\mathbf{B}_{\mathcal{T}}^{\mathbf{d}} &= \begin{bmatrix} \mathbf{b}_{\mathcal{T},1}^{\mathbf{d}} & \mathbf{b}_{\mathcal{T},2}^{\mathbf{d}} & \cdots & \mathbf{b}_{\mathcal{T},n^d}^{\mathbf{d}} \end{bmatrix}_{4 \times n^d}, \\
\mathbf{B}_{\mathcal{T}}^\ell &= \begin{bmatrix} t_1^{\mathcal{T}} & t_2^{\mathcal{T}} & \cdots & t_{n^\ell}^{\mathcal{T}} \end{bmatrix}_{1 \times n^\ell},
\end{aligned}
\tag{3.23}
$$

where n^1, n^c, n^d, and n^ℓ depend on the order of the corresponding approximation spaces and are given in the last column of Table 3. For a solution or test variable $\boldsymbol{V}_h$, one defines $\boldsymbol{V}_{\mathcal{T}} := \boldsymbol{V}_h|_{\mathcal{T}}$. Next, recalling (3.13), one writes the following local interpolation operators for each $\mathcal{T}$:

$$
\begin{aligned}
\boldsymbol{U}_{\mathcal{T}} &= \mathbf{B}_{\mathcal{T}}^1 \mathbf{q}_{\mathcal{T}}^1, & \lceil \mathbf{grad}\, \boldsymbol{U}_{\mathcal{T}} \rceil &= \mathbf{G}_{\mathcal{T}}^1 \mathbf{q}_{\mathcal{T}}^1, & \lceil \boldsymbol{K}_{\mathcal{T}} \rceil &= \mathbf{B}_{\mathcal{T}}^{\mathbf{c}} \mathbf{q}_{\mathcal{T}}^{\mathbf{c}}, & \lceil \boldsymbol{P}_{\mathcal{T}} \rceil &= \mathbf{B}_{\mathcal{T}}^{\mathbf{d}} \mathbf{q}_{\mathcal{T}}^{\mathbf{d}}, & p_{\mathcal{T}} &= \mathbf{B}_{\mathcal{T}}^\ell \mathbf{q}_{\mathcal{T}}^\ell, \\
\Upsilon_{\mathcal{T}} &= \mathbf{B}_{\mathcal{T}}^1 \mathbf{t}_{\mathcal{T}}^1, & \lceil \mathbf{grad}\, \Upsilon_{\mathcal{T}} \rceil &= \mathbf{G}_{\mathcal{T}}^1 \mathbf{t}_{\mathcal{T}}^1, & \lceil \boldsymbol{\kappa}_{\mathcal{T}} \rceil &= \mathbf{B}_{\mathcal{T}}^{\mathbf{c}} \mathbf{t}_{\mathcal{T}}^{\mathbf{c}}, & \lceil \boldsymbol{\pi}_{\mathcal{T}} \rceil &= \mathbf{B}_{\mathcal{T}}^{\mathbf{d}} \mathbf{t}_{\mathcal{T}}^{\mathbf{d}}, & q_{\mathcal{T}} &= \mathbf{B}_{\mathcal{T}}^\ell \mathbf{t}_{\mathcal{T}}^\ell,
\end{aligned}
\tag{3.24}
$$

where $\mathbf{t}_{\mathcal{T}}^1$, $\mathbf{t}_{\mathcal{T}}^{\mathbf{c}}$, $\mathbf{t}_{\mathcal{T}}^{\mathbf{d}}$, and $\mathbf{t}_{\mathcal{T}}^\ell$ are some column vectors containing arbitrary real numbers. These vectors are associated with the corresponding test spaces. $\mathbf{q}_{\mathcal{T}}^1$, $\mathbf{q}_{\mathcal{T}}^{\mathbf{c}}$, $\mathbf{q}_{\mathcal{T}}^{\mathbf{d}}$, and $\mathbf{q}_{\mathcal{T}}^\ell$ are vectors of the unknown local degrees of freedom, that is

$$\mathbf{q}^1_{\mathfrak{T}} = \begin{bmatrix} \mathtt{q}^1_{\mathfrak{T},1} & \mathtt{q}^1_{\mathfrak{T},2} & \cdots & \mathtt{q}^1_{\mathfrak{T},n^1} \end{bmatrix}^{\mathsf{T}}, \quad \mathtt{q}^1_{\mathfrak{T},m} = U^J_h(\mathbf{X}_i),$$

$$\mathbf{q}^{\mathbf{c}}_{\mathfrak{T}} = \begin{bmatrix} \mathtt{q}^{\mathbf{c}}_{\mathfrak{T},1} & \mathtt{q}^{\mathbf{c}}_{\mathfrak{T},2} & \cdots & \mathtt{q}^{\mathbf{c}}_{\mathfrak{T},n^c} \end{bmatrix}^{\mathsf{T}}, \quad \mathtt{q}^{\mathbf{c}}_{\mathfrak{T},k} = \phi^{\mathfrak{T},\mathcal{E}_i}_{I,J}(\boldsymbol{K}_{\mathfrak{T}}), \quad \mathtt{q}^{\mathbf{c}}_{\mathfrak{T},l} = \phi^{\mathfrak{T},\mathfrak{T}}_{I,J}(\boldsymbol{K}_{\mathfrak{T}}),$$

$$\mathbf{q}^{\mathbf{d}}_{\mathfrak{T}} = \begin{bmatrix} \mathtt{q}^{\mathbf{d}}_{\mathfrak{T},1} & \mathtt{q}^{\mathbf{d}}_{\mathfrak{T},2} & \cdots & \mathtt{q}^{\mathbf{d}}_{\mathfrak{T},n^d} \end{bmatrix}^{\mathsf{T}}, \quad \mathtt{q}^{\mathbf{d}}_{\mathfrak{T},k} = \psi^{\mathfrak{T},\mathcal{E}_i}_{I,J}(\boldsymbol{P}_{\mathfrak{T}}), \quad \mathtt{q}^{\mathbf{d}}_{\mathfrak{T},l} = \psi^{\mathfrak{T},\mathfrak{T}}_{I,J}(\boldsymbol{P}_{\mathfrak{T}}),$$

$$\mathbf{q}^{\ell}_{\mathfrak{T}} = \begin{bmatrix} \mathtt{q}^{\ell}_{\mathfrak{T},1} & \mathtt{q}^{\ell}_{\mathfrak{T},2} & \cdots & \mathtt{q}^{\ell}_{\mathfrak{T},n^\ell} \end{bmatrix}^{\mathsf{T}}, \quad \mathtt{q}^{\ell}_{\mathfrak{T},i} = \omega^{\mathfrak{T}}_i(p_{\mathfrak{T}}). \tag{3.25}$$

Note that $U^J_h(\mathbf{X}_i)$, $J = 1, 2$ is the value of the displacement at the i-th node of $\mathfrak{T}$, and $m := J + 2(i-1)$. Also, $\phi^{\mathfrak{T},\mathcal{E}_i}_{I,J}$, $\phi^{\mathfrak{T},\mathfrak{T}}_{I,J}$ and $\psi^{\mathfrak{T},\mathcal{E}_i}_{I,J}$, $\psi^{\mathfrak{T},\mathfrak{T}}_{I,J}$ are given in (3.6) and (3.10) with the hat symbols removed. The numberings k and l are defined in (3.22), and the size of the vectors $(\mathbf{q}^1_{\mathfrak{T}}, \mathbf{q}^{\mathbf{c}}_{\mathfrak{T}}, \mathbf{q}^{\mathbf{d}}_{\mathfrak{T}}, \mathbf{q}^{\ell}_{\mathfrak{T}})$ and $(\mathbf{t}^1_{\mathfrak{T}}, \mathbf{t}^{\mathbf{c}}_{\mathfrak{T}}, \mathbf{t}^{\mathbf{d}}_{\mathfrak{T}}, \mathbf{t}^{\ell}_{\mathfrak{T}})$ is (n^1, n^c, n^d, n^ℓ). Inserting (3.24) into the restriction of (3.20) to an element $\mathfrak{T}$, and then summing over $\mathfrak{T} \in \mathcal{B}_h$ results in the following representation of (3.20):

$$\sum_{\mathfrak{T}\in\mathcal{B}_h} (\mathbf{t}^1_{\mathfrak{T}})^{\mathsf{T}} \left(\mathbf{K}^{\mathbf{1d}}_{\mathfrak{T}} \mathbf{q}^{\mathbf{d}}_{\mathfrak{T}} - \mathbf{F}^1_{\mathfrak{T}} - \mathbf{F}^1_{\mathcal{E}^{\mathfrak{T}}_t} \right) = 0,$$

$$\sum_{\mathfrak{T}\in\mathcal{B}_h} (\mathbf{t}^{\mathbf{c}}_{\mathfrak{T}})^{\mathsf{T}} \left(\mathbf{N}^{\mathbf{c}}_{\mathfrak{T}}(\mathbf{q}^{\mathbf{c}}_{\mathfrak{T}}, \mathbf{q}^{\ell}_{\mathfrak{T}}) + \mathbf{K}^{\mathbf{cd}}_{\mathfrak{T}} \mathbf{q}^{\mathbf{d}}_{\mathfrak{T}} \right) = 0,$$

$$\sum_{\mathfrak{T}\in\mathcal{B}_h} (\mathbf{t}^{\mathbf{d}}_{\mathfrak{T}})^{\mathsf{T}} \left(\mathbf{K}^{\mathbf{d1}}_{\mathfrak{T}} \mathbf{q}^1_{\mathfrak{T}} + \mathbf{K}^{\mathbf{dc}}_{\mathfrak{T}} \mathbf{q}^{\mathbf{c}}_{\mathfrak{T}} \right) = 0,$$

$$\sum_{\mathfrak{T}\in\mathcal{B}_h} (\mathbf{t}^{\ell}_{\mathfrak{T}})^{\mathsf{T}} \left(\mathbf{N}^{\ell}_{\mathfrak{T}}(\mathbf{q}^{\mathbf{c}}_{\mathfrak{T}}) \right) = 0. \tag{3.26}$$

The new local matrices and vectors used in the above relations are defined as

$$\mathbf{K}^{\mathbf{1d}}_{\mathfrak{T}} = \int_{\mathfrak{T}} (\mathbf{G}^1_{\mathfrak{T}})^{\mathsf{T}} \mathbf{B}^{\mathbf{d}}_{\mathfrak{T}} \, dA, \quad \mathbf{K}^{\mathbf{d1}}_{\mathfrak{T}} = (\mathbf{K}^{\mathbf{1d}}_{\mathfrak{T}})^{\mathsf{T}}, \tag{3.27}$$

$$\mathbf{K}^{\mathbf{cd}}_{\mathfrak{T}} = - \int_{\mathfrak{T}} (\mathbf{B}^{\mathbf{c}}_{\mathfrak{T}})^{\mathsf{T}} \mathbf{B}^{\mathbf{d}}_{\mathfrak{T}} \, dA, \quad \mathbf{K}^{\mathbf{dc}}_{\mathfrak{T}} = (\mathbf{K}^{\mathbf{cd}}_{\mathfrak{T}})^{\mathsf{T}}, \tag{3.28}$$

$$\mathbf{N}^{\mathbf{c}}_{\mathfrak{T}}(\mathbf{q}^{\mathbf{c}}_{\mathfrak{T}}, \mathbf{q}^{\ell}_{\mathfrak{T}}) = \int_{\mathfrak{T}} (\mathbf{B}^{\mathbf{c}}_{\mathfrak{T}})^{\mathsf{T}} \left(\left\lceil \widetilde{\boldsymbol{P}}([\mathbf{B}^{\mathbf{c}}_{\mathfrak{T}} \mathbf{q}^{\mathbf{c}}_{\mathfrak{T}}]) \right\rceil + (\mathbf{B}^{\ell}_{\mathfrak{T}} \mathbf{q}^{\ell}_{\mathfrak{T}}) \left\lceil \boldsymbol{Q} \left([\mathbf{B}^{\mathbf{c}}_{\mathfrak{T}} \mathbf{q}^{\mathbf{c}}_{\mathfrak{T}}] \right) \right\rceil \right) dA, \tag{3.29}$$

$$\mathbf{N}^{\ell}_{\mathfrak{T}}(\mathbf{q}^{\mathbf{c}}_{\mathfrak{T}}) = \int_{\mathfrak{T}} (\mathbf{B}^{\ell}_{\mathfrak{T}})^{\mathsf{T}} C\big(J_{\mathfrak{T}}(\mathbf{q}^{\mathbf{c}}_{\mathfrak{T}})\big) dA, \quad J_{\mathfrak{T}}(\mathbf{q}^{\mathbf{c}}_{\mathfrak{T}}) = \det(\boldsymbol{I} + [\mathbf{B}^{\mathbf{c}}_{\mathfrak{T}} \mathbf{q}^{\mathbf{c}}_{\mathfrak{T}}]), \tag{3.30}$$

$$\mathbf{F}^1_{\mathfrak{T}} = \int_{\mathfrak{T}} (\mathbf{B}^1_{\mathfrak{T}})^{\mathsf{T}} \rho_0 \boldsymbol{B} \, dA, \tag{3.31}$$

$$\mathbf{F}^1_{\mathcal{E}^{\mathfrak{T}}_t} = \begin{cases} \int_{\mathcal{E}^{\mathfrak{T}}_t} (\mathbf{B}^1_{\mathcal{E}^{\mathfrak{T}}_t})^{\mathsf{T}} \overline{\boldsymbol{T}} \, ds, & \text{if } \mathfrak{T} \cap \Gamma_t = \mathcal{E}^{\mathfrak{T}}_t, \\ \mathbf{0}_{n^1 \times 1}, & \text{otherwise.} \end{cases} \tag{3.32}$$

The term $\mathcal{E}^{\mathfrak{T}}_t$ in (3.32) denotes the edge of $\mathfrak{T}$ that lies on the traction boundary Γ_t. Also, to define $\mathbf{B}^1_{\mathcal{E}_t}$ in (3.32), consider a zero matrix of size $2 \times n^1$, and then substitute 1D Lagrange polynomials over $\mathcal{E}^{\mathfrak{T}}_t$ into those columns that are associated with $\mathcal{E}^{\mathfrak{T}}_t$. Let $\mathbf{K}^{\mathbf{1d}}_{\widehat{\mathfrak{T}}} = \int_{\widehat{\mathfrak{T}}} (\mathbf{G}^1_{\widehat{\mathfrak{T}}})^{\mathsf{T}} \mathbf{B}^{\mathbf{d}}_{\widehat{\mathfrak{T}}} \, d\hat{A}$ and $\mathbf{K}^{\mathbf{cd}}_{\widehat{\mathfrak{T}}} = - \int_{\widehat{\mathfrak{T}}} (\mathbf{B}^{\mathbf{c}}_{\widehat{\mathfrak{T}}})^{\mathsf{T}} \mathbf{B}^{\mathbf{d}}_{\widehat{\mathfrak{T}}} \, d\hat{A}$ be the counterparts of (3.27) and (3.28) for the reference finite element $\widehat{\mathfrak{T}}$, where $\mathbf{G}^1_{\widehat{\mathfrak{T}}}$, $\mathbf{B}^{\mathbf{c}}_{\widehat{\mathfrak{T}}}$, and $\mathbf{B}^{\mathbf{d}}_{\widehat{\mathfrak{T}}}$ are obtained according to (3.23) but using the reference local shape functions. For all $\mathfrak{T} \in \mathcal{B}_h$, Lemma 9, (ii) and (v) imply the following relations:

$$\mathbf{K}^{\mathbf{1d}}_{\mathfrak{T}} = o_{\mathfrak{T}} \mathbf{K}^{\mathbf{1d}}_{\widehat{\mathfrak{T}}}, \quad \mathbf{K}^{\mathbf{cd}}_{\mathfrak{T}} = o_{\mathfrak{T}} \mathbf{K}^{\mathbf{cd}}_{\widehat{\mathfrak{T}}}. \tag{3.33}$$

Therefore, the local matrices $\mathbf{K}^{\mathbf{1d}}_{\mathfrak{T}}$, $\mathbf{K}^{\mathbf{d1}}_{\mathfrak{T}}$, $\mathbf{K}^{\mathbf{cd}}_{\mathfrak{T}}$, and $\mathbf{K}^{\mathbf{dc}}_{\mathfrak{T}}$ are independent of the geometry of $\mathfrak{T}$ and depend only on the ordering of the three vertices of $\mathfrak{T}$. In practice, the relations (3.33) enable one to obtain (3.27) and (3.28) $\forall \mathfrak{T} \in \mathcal{B}_h$ with much less computational cost. It is also practical to change the domain variables of the integrals (3.29)–(3.32) from $\mathbf{X} \in \mathfrak{T}$ to $\boldsymbol{\xi} \in \widehat{\mathfrak{T}}$. For example, (3.29) and (3.31) can be obtained as

$$\mathbf{N}^{\mathbf{c}}_{\mathfrak{T}}(\mathbf{q}^{\mathbf{c}}_{\mathfrak{T}}, \mathbf{q}^{\ell}_{\mathfrak{T}}) = |\det \mathbf{J}_{\mathfrak{T}}| \int_{\widehat{\mathfrak{T}}} (\bar{\mathbf{B}}^{\mathbf{c}}_{\mathfrak{T}})^{\mathsf{T}} \left(\left\lceil \widetilde{\boldsymbol{P}}([\bar{\mathbf{B}}^{\mathbf{c}}_{\mathfrak{T}} \mathbf{q}^{\mathbf{c}}_{\mathfrak{T}}]) \right\rceil + (\mathbf{B}^{\ell}_{\widehat{\mathfrak{T}}} \mathbf{q}^{\ell}_{\mathfrak{T}}) \left\lceil \boldsymbol{Q} \left([\bar{\mathbf{B}}^{\mathbf{c}}_{\mathfrak{T}} \mathbf{q}^{\mathbf{c}}_{\mathfrak{T}}] \right) \right\rceil \right) d\hat{A},$$

$$\mathbf{F}^1_{\mathcal{T}} = \left| \det \mathbf{J}_{\mathcal{T}} \right| \int_{\widehat{\mathcal{T}}} (\mathbf{B}^1_{\widehat{\mathcal{T}}})^{\mathsf{T}} \rho_0 (\boldsymbol{B} \circ \mathbf{T}_{\mathcal{T}}) \, d\hat{A},$$

where $\bar{\mathbf{B}}^{\mathbf{c}}_{\mathcal{T}} = \mathbf{B}^{\mathbf{c}}_{\mathcal{T}} \circ \mathbf{T}_{\mathcal{T}}$, and $\mathbf{B}^{\ell}_{\mathcal{T}}$ and $\mathbf{B}^1_{\widehat{\mathcal{T}}}$ are actually $\mathbf{B}^{\ell}_{\mathcal{T}}$ and $\mathbf{B}^1_{\mathcal{T}}$ but are written using the reference local shape functions.

Next we assemble (3.27)–(3.32) for all $\mathcal{T} \in \mathcal{B}_h$ and then accordingly write the global counterparts of the vectors of the local degrees of freedom (3.25) and $\mathbf{t}^1_{\mathcal{T}}, \mathbf{t}^{\mathbf{c}}_{\mathcal{T}}, \mathbf{t}^{\mathbf{d}}_{\mathcal{T}}$, and $\mathbf{t}^{\ell}_{\mathcal{T}}$. We use the subscript h for both the assembled and the global matrices and vectors, e.g., we denote the assembled form of $\mathbf{K}^{\mathbf{cd}}_{\mathcal{T}}$ and $\mathbf{F}^1_{\mathcal{T}}$ by $\mathbf{K}^{\mathbf{cd}}_h$ and $\mathbf{F}^1_h$, respectively, and the global counterparts of $\mathbf{q}^1_{\mathcal{T}}$ and $\mathbf{t}^1_{\mathcal{T}}$ by $\mathbf{q}^1_h$ and $\mathbf{t}^1_h$, respectively. Next, according to (3.26), one defines

$$\mathbb{Q}_h = \begin{bmatrix} \mathbf{q}^1_h \\ \mathbf{q}^{\mathbf{c}}_h \\ \mathbf{q}^{\mathbf{d}}_h \\ \mathbf{q}^{\ell}_h \end{bmatrix}, \quad \mathbb{T}_h = \begin{bmatrix} \mathbf{t}^1_h \\ \mathbf{t}^{\mathbf{c}}_h \\ \mathbf{t}^{\mathbf{d}}_h \\ \mathbf{t}^{\ell}_h \end{bmatrix}, \quad \mathbb{K}_h = \begin{bmatrix} \mathbf{0} & \mathbf{0} & \mathbf{K}^{\mathbf{1d}}_h & \mathbf{0} \\ \mathbf{0} & \mathbf{0} & \mathbf{K}^{\mathbf{cd}}_h & \mathbf{0} \\ \mathbf{K}^{\mathbf{d1}}_h & \mathbf{K}^{\mathbf{dc}}_h & \mathbf{0} & \mathbf{0} \\ \mathbf{0} & \mathbf{0} & \mathbf{0} & \mathbf{0} \end{bmatrix}, \quad \mathbb{N}_h(\mathbb{Q}_h) = \begin{bmatrix} \mathbf{0} \\ \mathbf{N}^{\mathbf{c}}_h(\mathbf{q}^{\mathbf{c}}_h, \mathbf{q}^{\ell}_h) \\ \mathbf{0} \\ \mathbf{N}^{\ell}_h(\mathbf{q}^{\mathbf{c}}_h) \end{bmatrix}, \quad \mathbb{F}_h = \begin{bmatrix} \mathbf{F}^1_h + \mathbf{F}^1_{\Gamma_t} \\ \mathbf{0} \\ \mathbf{0} \\ \mathbf{0} \end{bmatrix}, \quad (3.34)$$

where $\mathbb{Q}_h$ includes all the unknown degrees of freedom of the problem and a few known degrees of freedom in its $\mathbf{q}^1_h$, which comes from the displacement boundary $\boldsymbol{U}|_{\Gamma_d} = \overline{\boldsymbol{U}}$. $\mathbb{T}_h$ is a vector of arbitrary real numbers with a few fixed zero elements in its $\mathbf{t}^1_h$ as a result of $\boldsymbol{\Upsilon}|_{\Gamma_d} = \mathbf{0}$. Suppose n is the total number of nodes in the mesh except those lying on Γ_d, and $n_{\mathcal{E}}$ and $n_{\mathcal{T}}$ are the total numbers of edges and elements in the mesh, respectively. After imposing the displacement boundary conditions, the total number of degrees of freedom is

$$N = 2n + (e^c + e^d)n_{\mathcal{E}} + (a^c + a^d + a^{\ell})n_{\mathcal{T}},$$

where e^c (e^d) and a^c (a^d) are the numbers of local degrees of freedom for displacement gradient $\boldsymbol{K}$ (stress $\boldsymbol{P}$), which are defined on each edge and on each element, respectively. Also, a^{ℓ} is the number of local degrees of freedom for the pressure-like variable p, which is defined only on each element. These numbers depend on the choice of CSFEMs and the orders of their approximation spaces; e^c and e^d can be read from the third column of Table 3 and a^c, a^d, and a^{ℓ} from its fourth column. Recalling n^c and n^d in (3.23), we have $n^c = 3e^c + a^c$ and $n^d = 3e^d + a^d$. The size of the sparse matrix $\mathbb{K}_h$ is $N \times N$, and the size of the vectors $\mathbb{T}_h, \mathbb{Q}_h, \mathbb{N}_h$, and, $\mathbb{F}_h$ is $N \times 1$. Let $N^1 = 2n$, $N^c = n_{\mathcal{E}} e^c + n_{\mathcal{T}} a^c$, $N^d = n_{\mathcal{E}} e^d + n_{\mathcal{T}} a^d$, and $N^{\ell} = n_{\mathcal{T}} a^{\ell}$. Then, the size of the global vectors $(\mathbf{q}^1_h, \mathbf{q}^{\mathbf{c}}_h, \mathbf{q}^{\mathbf{d}}_h, \mathbf{q}^{\ell}_h)$ and $(\mathbf{t}^1_h, \mathbf{t}^{\mathbf{c}}_h, \mathbf{t}^{\mathbf{d}}_h, \mathbf{t}^{\ell}_h)$ is $(N^1, N^c, N^d, N^{\ell})$.

Remark 13. From (3.33), the symmetric sparse matrix $\mathbb{K}_h$ does not depend on the geometry and dimensions, but only on the connectivity and numbering of the elements of the mesh. That is, the matrix $\mathbb{K}_h$ is identical for homeomorphic (topologically equivalent) meshes.

By using (3.34), one can write (3.26) as $\mathbb{T}_h^{\mathsf{T}} \left(\mathbb{K}_h \mathbb{Q}_h + \mathbb{N}_h(\mathbb{Q}_h) - \mathbb{F}_h \right) = 0$. Since $\mathbb{T}_h$ is arbitrary, one obtains the following nonlinear system of algebraic equations:

$$\mathbb{K}_h \mathbb{Q}_h + \mathbb{N}_h(\mathbb{Q}_h) = \mathbb{F}_h. \quad (3.35)$$

Define $\mathbb{R}_h(\mathbb{Q}_h) := \mathbb{K}_h \mathbb{Q}_h + \mathbb{N}_h(\mathbb{Q}_h) - \mathbb{F}_h$ as the residual of the nonlinear equation (3.35). Using Newton's method, the solution of (3.35) can be obtained iteratively by $\mathbb{Q}_h^{(i+1)} = \mathbb{Q}_h^{(i)} - \mathbb{K}_{t_h}^{-1}\left(\mathbb{Q}_h^{(i)}\right) \mathbb{R}_h\left(\mathbb{Q}_h^{(i)}\right)$ starting form an initial guess, where i is the iteration number and $\mathbb{K}_{t_h}$ is the tangent stiffness matrix (Jacobian matrix) given by

$$\mathbb{K}_{t_h} = \begin{bmatrix} \mathbf{0} & \mathbf{0} & \mathbf{K}^{\mathbf{1d}}_h & \mathbf{0} \\ \mathbf{0} & \mathbf{H}^{\mathbf{cc}}_h & \mathbf{K}^{\mathbf{cd}}_h & \mathbf{H}^{\mathbf{c}\ell}_h \\ \mathbf{K}^{\mathbf{d1}}_h & \mathbf{K}^{\mathbf{dc}}_h & \mathbf{0} & \mathbf{0} \\ \mathbf{0} & \mathbf{H}^{\ell\mathbf{c}}_h & \mathbf{0} & \mathbf{0} \end{bmatrix}.$$

Here, $\mathbf{H}^{\ell\mathbf{c}}_h = (\mathbf{H}^{\mathbf{c}\ell}_h)^{\mathsf{T}}$, and $\mathbf{H}^{\mathbf{cc}}_h$ and $\mathbf{H}^{\mathbf{c}\ell}_h$ are obtained by assembling the following matrices for all $\mathcal{T} \in \mathcal{B}_h$:

$$\mathbf{H}^{\mathbf{cc}}_{\mathcal{T}}(\mathbf{q}^{\mathbf{c}}_{\mathcal{T}}, \mathbf{q}^{\ell}_{\mathcal{T}}) = \int_{\mathcal{T}} (\mathbf{B}^{\mathbf{c}}_{\mathcal{T}})^{\mathsf{T}} \widetilde{\mathbf{A}} \left(\mathbf{B}^{\mathbf{c}}_{\mathcal{T}} \mathbf{q}^{\mathbf{c}}_{\mathcal{T}}, \mathbf{B}^{\ell}_{\mathcal{T}} \mathbf{q}^{\ell}_{\mathcal{T}} \right) \mathbf{B}^{\mathbf{c}}_{\mathcal{T}} \, dA, \qquad \mathbf{H}^{\mathbf{c}\ell}_{\mathcal{T}}(\mathbf{q}^{\mathbf{c}}_{\mathcal{T}}) = \int_{\mathcal{T}} (\mathbf{B}^{\mathbf{c}}_{\mathcal{T}})^{\mathsf{T}} \left[\mathbf{Q} \left([\mathbf{B}^{\mathbf{c}}_{\mathcal{T}} \mathbf{q}^{\mathbf{c}}_{\mathcal{T}}] \right) \right] \mathbf{B}^{\ell}_{\mathcal{T}} \, dA, \quad (3.36)$$

where $\widetilde{\mathbf{A}}(\boldsymbol{K}, p)$ in 2D is a 4×4 matrix representation of the 4th-order elasticity tensor obtained form the derivative of components of the constitutive relation $\boldsymbol{P} = \widetilde{\boldsymbol{P}}(\boldsymbol{K}) + p\,\boldsymbol{Q}\,(\boldsymbol{K})$ with respect to components of $\boldsymbol{K}$. Note that the tangent stiffness matrix $\mathbb{K}_{t_h}$ is symmetric and indefinite; this is closely related to Remark 4.

For our numerical examples, we consider the incompressible neo-Hookean solid with the energy function

$$\widetilde{W} = \frac{\mu}{2}(I_1 - 2), \quad (3.37)$$

where μ is the shear modulus at the ground state. The constitutive part of stress reads $\widetilde{P}(\boldsymbol{K}) = \mu(\boldsymbol{I} + \boldsymbol{K})$. We use the following functions to impose the incompressibility condition $J = 1$: $C_1(J) = J - 1$, and $C_2(J) = \ln J$. We have observed in our numerical examples that $C_1(J)$ has a better performance over $C_1(J)$ in problems with tension loadings, while in bending problems with very refined meshes $C_2(J)$ has a better performance over $C_1(J)$. We need the following relations for calculating (3.36):

$$\boldsymbol{Q}_1(\boldsymbol{K}) = J\boldsymbol{F}^{-\mathsf{T}}, \qquad \widetilde{\mathbf{A}}_1(p) = \mu\mathbf{I} - p\bar{\mathbf{I}},$$
$$\boldsymbol{Q}_2(\boldsymbol{K}) = \boldsymbol{F}^{-\mathsf{T}}, \qquad \widetilde{\mathbf{A}}_2(\boldsymbol{K}, p) = \mu\mathbf{I} - \frac{p}{J}\bar{\mathbf{I}} - p\lceil\boldsymbol{F}^{-\mathsf{T}}\rceil\lceil\boldsymbol{F}^{-\mathsf{T}}\rceil^{\mathsf{T}},$$

where $\mathbf{I}$ is the 4×4 identity matrix, and $\bar{\mathbf{I}}$ denotes an anti-diagonal matrix with non-zero components $\bar{\mathbf{I}}^{14} = \bar{\mathbf{I}}^{41} = -1$ and $\bar{\mathbf{I}}^{23} = \bar{\mathbf{I}}^{32} = 1$. One can show that $\boldsymbol{F}^{-\mathsf{T}} = \frac{1}{J}(\boldsymbol{I} + \mathbf{R}\boldsymbol{K}\mathbf{R}^{\mathsf{T}})$.

3.5. Solvability and stability

Theorem 14. *The tangent stiffness matrix $\mathbb{K}_{t_h}$ is invertible (non-singular) if and only if the following four conditions hold:*

(i) $\ker(\mathbf{K}_h^{\mathbf{d1}}) = \{\mathbf{0}_{N^1 \times 1}\}$,

(ii) $\ker(\mathbf{K}_h^{\mathbf{cd}}) \cap \ker(\mathbf{K}_h^{\mathbf{1d}}) = \{\mathbf{0}_{N^d \times 1}\}$,

(iii) $\ker(\mathbf{H}_h^{\mathbf{c}\ell}) = \{\mathbf{0}_{N^\ell \times 1}\}$,

(iv) $\ker(\mathbf{H}_h^{\mathbf{cc}}) \cap K = \{\mathbf{0}_{N^c \times 1}\}$, *where* $K = \{\mathbf{X} \in \ker(\mathbf{H}_h^{\ell\mathbf{c}}) : \mathbf{Y}^{\mathsf{T}}\mathbf{K}_h^{\mathbf{dc}}\mathbf{X} = 0, \forall\mathbf{Y} \in \ker(\mathbf{K}_h^{\mathbf{1d}})\}$.

Proof. Rearrange the rows and the columns of $\mathbb{K}_{t_h}$ to obtain

$$\mathbb{K}_{t_h} = \begin{bmatrix} \mathbb{A}_h & \mathbb{B}_h^{\mathsf{T}} \\ \mathbb{B}_h & \mathbf{0} \end{bmatrix}, \quad \mathbb{A}_h = \begin{bmatrix} \mathbf{H}_h^{\mathbf{cc}} & \mathbf{0} \\ \mathbf{0} & \mathbf{0} \end{bmatrix}, \quad \mathbb{B} = \begin{bmatrix} \mathbf{H}_h^{\ell\mathbf{c}} & \mathbf{0} \\ \mathbf{K}_h^{\mathbf{dc}} & \mathbf{K}_h^{\mathbf{d1}} \end{bmatrix}, \quad \mathbb{B}_h^{\mathsf{T}} = \begin{bmatrix} \mathbf{H}_h^{\mathbf{c}\ell} & \mathbf{K}_h^{\mathbf{cd}} \\ \mathbf{0} & \mathbf{K}_h^{\mathbf{1d}} \end{bmatrix}.$$

Then, apply [36, Theorem 3.2.1] and use an argument similar to that of [36, §3.2.5]. □

Corollary 15. *The tangent stiffness matrix $\mathbb{K}_{t_h}$ is invertible, only if $0 \leq N^d - N^1 \leq N^c$ and $N^\ell \leq N^c$.*

Proof. Theorem 14, (i), (ii), and (iii) imply that $N^1 \leq N^d$, $N^d \leq N^c + N^1$, and $N^\ell \leq N^c$, respectively. □

Remark 16. Given a matrix $\mathbf{A}_{m \times n}$, there exist two unitary matrices $\mathbf{U}_{m \times m}$ and $\mathbf{V}_{n \times n}$ and a rectangular diagonal matrix $\mathbf{S}_{m \times n}$ with non-negative entries on the main diagonal such that $\mathbf{A} = \mathbf{U}\mathbf{S}\mathbf{V}^*$, where the superscript $*$ denotes the conjugate transpose. The diagonal entries of $\mathbf{S}$, $\mathbf{S}_{i,j}$ with $i = j$, are known as the singular values of $\mathbf{A}$. It is straightforward to show that $\ker(\mathbf{A}) = \{\mathbf{0}\}$, if and only if the smallest singular value of $\mathbf{A}$ is non-zero. This can be used to numerically check the conditions of Theorem 14. In particular, one can compute the smallest singular values of sparse matrices $\mathbf{K}_h^{\mathbf{d1}}$ and $\begin{bmatrix} \mathbf{K}_h^{\mathbf{dc}} & \mathbf{K}_h^{\mathbf{d1}} \end{bmatrix}^{\mathsf{T}}$ to check (i) and (ii), respectively.

Remark 17. Conditions of Theorem 14 can be rewritten as inf-sup conditions. For example, $\ker(\mathbf{K}_h^{\mathbf{d1}}) = \{\mathbf{0}_{N^1 \times 1}\}$, where $\mathbf{K}_h^{\mathbf{d1}} : \mathbb{R}^{N^1} \to \mathbb{R}^{N^d}$, is equivalent to the following statement:

$$\exists\beta_h > 0, \quad \text{such that} \quad \inf_{\mathbf{X} \in \mathbb{R}^{N^1}} \sup_{\mathbf{Y} \in \mathbb{R}^{N^d}} \frac{\mathbf{Y}^{\mathsf{T}}\mathbf{K}_h^{\mathbf{d1}}\mathbf{X}}{\|\mathbf{X}\|_{\mathbb{R}^{N^1}} \|\mathbf{Y}\|_{\mathbb{R}^{N^d}}} \geq \beta_h.$$

Also see [26, Lemmas A.39 and A.40] and note that $\mathbb{R}^{N^d\star}$ can be identified with $\mathbb{R}^{N^d}$. One can also show that β_h is the smallest singular value of $\mathbf{K}_h^{\mathbf{d1}}$, see [26, Remark 2.23] and [36, §3.4.3].

Recall that $\mathbf{H}_h^{\mathbf{c}\ell}(\mathbf{q}_h^{\mathbf{c}})$ and $\mathbf{H}_h^{\mathbf{cc}}(\mathbf{q}_h^{\mathbf{c}}, \mathbf{q}_h^{\ell})$ are nonlinear operators. They depend on the state of deformation of the body and vary at each iteration of Newton's method. Hence, it is difficult to draw a general conclusion for invertibility of $\mathbb{K}_{t_h}$ based on the conditions (iii) and (iv) of Theorem 14 without considering the physics of the problem. On the other hand, $\mathbf{K}_h^{\mathbf{cd}}$ and $\mathbf{K}_h^{\mathbf{1d}}$ are linear operators and remain unchanged throughout the deformation. Therefore, in the following discussions, we focus on conditions (i) and (ii) of Theorem 14.

Considering different meshes with few elements and counting the total degrees of freedom (N^1, N^c, N^d, N^ℓ), one can check that all the possible mixed formulations of the first and the second order satisfy $N^\ell \leq N^c$. However, many of them violate $0 \leq N^d - N^1 \leq N^c$, and hence, result in a singular tangent stiffness matrix $\mathbb{K}_{t_h}$. Those are H2c$\bar{m}$d$\bar{1}$Ln, H2cmd$\bar{1}$Ln,

H2c$\bar{m}$d1Ln, H2cmd1Ln, H1c$\bar{1}$d1Ln, Hmc$\bar{1}$d$\bar{2}$Ln, Hmc$\bar{1}$d2Ln, Hmc1d$\bar{2}$Ln, Hmc1d2Ln, and Hmc$\bar{2}$d2Ln for $m = 1, 2$ and $n = 0, 1, 2$. In addition, considering several arbitrary meshes and computing the smallest singular value of $\left[\mathbf{K}_h^{\mathbf{dc}} \quad \mathbf{K}_h^{\mathbf{d1}} \right]^\top$, we conclude that $\ker(\mathbf{K}_h^{\mathbf{cd}}) \cap \ker(\mathbf{K}_h^{\mathbf{1d}}) = \{\mathbf{0}_{N^d \times 1}\}$ does not hold, in general, for Hmc$\bar{n}$d$\bar{n}$Lr and HmcndnLr with $m, n = 1, 2$ and $r = 0, 1, 2$. The cases mentioned above are 75 out of 96 possible first and second order mixed methods. These cases have solvability issues for any mesh size its h.

In [17] based on the observations in several numerical examples it was reported that only 7 out of the 32 possible choices of the first and second-order CSFEMs for compressible solids result in solvable algebraic systems. Those observations agree with the above arguments because all the remaining 25 mixed methods violate one or both of the necessary conditions $\ker(\mathbf{K}_h^{\mathbf{d1}}) = \{\mathbf{0}_{N^1 \times 1}\}$ and $\ker(\mathbf{K}_h^{\mathbf{cd}}) \cap \ker(\mathbf{K}_h^{\mathbf{1d}}) = \{\mathbf{0}_{N^d \times 1}\}$. In fact, those 25 cases can be obtained directly from the 75 cases we mentioned above by removing the pressure field and the incompressibility constraint from the mixed formulations.

In view of Theorem 14, (*i*) and (*ii*), we have narrowed down the 96 possible choices of mixed FEMs to the following 21 solvable ones: H1c1d$\bar{1}$Lm, H1c$\bar{2}$d$\bar{1}$Lm, H1c$\bar{2}$d1Lm, H1c2d$\bar{1}$Lm, H1c2d1Lm, H1c2d$\bar{2}$Lm, and H2c2d$\bar{2}$Lm for $m = 0, 1, 2$. Satisfaction of the conditions of Theorem 14 for a given mesh is not sufficient; the *stability* of the method requires that all the four conditions hold as the mesh gets refined and h goes to zero. Our numerical examples suggest that H1c1d$\bar{1}$L0 and H2c2d$\bar{2}$L1 have an overall good performance among the first-order and second-order elements, respectively. These elements are illustrated in Fig. 4.

4. Numerical examples

In this section, we consider six different examples to assess the convergence and accuracy of CSFEMs in the analysis of incompressible solids. For all the examples, we consider the energy function (3.37). We use the L^2-norm to measure the values and the errors of the approximated filed variables ($\boldsymbol{U}_h, \boldsymbol{K}_h, \boldsymbol{P}_h, p_h$) over the entire mesh. We also use the Frobenius norm of a second-order tensor $\boldsymbol{T}$, $\|\boldsymbol{T}\| := \left(\sum_{I,J} T^{IJ} T^{IJ} \right)^{\frac{1}{2}}$ to show the distribution of the values of $\boldsymbol{K}_h$ and $\boldsymbol{P}_h$ in the deformed configurations.

Example 1: inflation of a cylindrical shell   We consider the inflation of an incompressible thick cylindrical shell shown in Fig. 5. The inner boundary of the shell is traction free and the outer boundary is subjected to $\boldsymbol{U}_{\text{out}} = (\lambda - 1)\mathbf{X}$. We assume that there is no body force, i.e., $\boldsymbol{B} = \mathbf{0}$. Owing to the incompressibility constraint $J = 1$, one can obtain the exact solution of the problem as follows:

$$\boldsymbol{U}_e(\mathbf{X}) = \left(\frac{r(R)}{R} - 1 \right) \mathbf{X},$$

$$p_e(\mathbf{X}) = -\mu \frac{R^2}{r(R)^2} + \frac{\mu(\lambda^2 - 1)R_{\text{out}}^2}{2} \left(\frac{1}{r(R_{\text{in}})^2} - \frac{1}{r(R)^2} \right) + \mu \ln \left(\frac{r(R_{\text{in}})}{R_{\text{in}} r(R)} R \right),$$

where $r(R) = \sqrt{R^2 + (\lambda^2 - 1)R_{\text{out}}^2}$ and $R = \|\mathbf{X}\|$. Having $\boldsymbol{U}_e$ and p_e, one can obtain $\boldsymbol{K}_e = \mathbf{grad}\, \boldsymbol{U}_e$ and $\boldsymbol{P}_e = \widetilde{\boldsymbol{P}}(\boldsymbol{K}_e) + p_e \boldsymbol{Q}(\boldsymbol{K}_e)$. The exact solution enables one to study and verify the accuracy and convergence of CSFEMs. Note that this is an example of a universal deformation [37]. For our numerical analysis, we assume that $R_{\text{in}} = 0.5$ mm, $R_{\text{out}} = 1$ mm, and $\lambda = 3$. We also assume $\mu = 1$ N/mm^2 in (3.37) and use the constraint function $C(J) = J - 1$. Using symmetry of the problem, we model only a quarter of the shell in the numerical analysis (see the generated unstructured meshes in Fig. 5). Using the symmetry and the numerical solutions of a quarter of the domain, one will be able to recover the solution for the entire domain.

As was discussed in §3.5, among the 96 possible choices of the first and second-order CSFEMs, only 21 may result in a non-singular tangent stiffness matrix $\mathbb{K}_{t_h}$ and the remaining 75 CSFEMs have solvability issues. We studied and compared the performance of the 21 solvable CSFEMs using the exact solution of this problem. Our numerical experiments indicate that the following 8 CSFEMs have good performance: H1c1d$\bar{1}$L0, H1c$\bar{2}$d$\bar{1}$L0, H1c$\bar{2}$d$\bar{1}$L1, H1c$\bar{2}$d1L0, H1c2d1L0, H2c2d$\bar{2}$L0, H2c2d$\bar{2}$L1, H2c2d$\bar{2}$L2. We do not consider the reaming 13 CSFEMs further due to their poor performance.

For the four meshes shown in Fig. 5, the relative L^2-norm of errors associated with each of the above 8 CSFEMs are given in Table 4. Considering the relative errors of the four primary field variables $\boldsymbol{U}$, $\boldsymbol{K}$, $\boldsymbol{P}$, and p, H2c2d$\bar{2}$L1 (#7) is the most accurate method among all CSFEMs. Based on the number of degrees of freedom in the fourth column, H1c1d$\bar{1}$L0 (#1) has the least computational cost among all CSFEMs. Although for an identical mesh, H1c$\bar{2}$d$\bar{1}$L0, H1c$\bar{2}$d$\bar{1}$L1, H1c$\bar{2}$d1L0, and H2c2d$\bar{2}$L2 (#2 − #4 and #8) have (many) more degrees of freedom than H1c1d$\bar{1}$L0 (#1), none of them has a better relative error in approximating the four primary variables. For an identical mesh, H1c2d1L0 and H2c2d$\bar{2}$L0 (#5 and #6) are more accurate than H1c1d$\bar{1}$L0 (#1) in approximating the four primary variables, but they are computationally much more expensive (more number of DOFs). In other words, it may be better to refine the mesh and use H1c1d$\bar{1}$L0 rather than using H1c2d1L0 or H2c2d$\bar{2}$L0 with a coarser mesh. Therefore, H2c2d$\bar{2}$L1 and H1c1d$\bar{1}$L0 (#1 and #7), which are shown in Fig. 4, have an overall better performance among all CSFEMs. Between these two methods, if we compare H1c1d$\bar{1}$L0 with 56298 #DOF and H2c2d$\bar{2}$L1 with 34240 #DOF, we conclude that the latter method results in a more accurate solution for less computational cost.
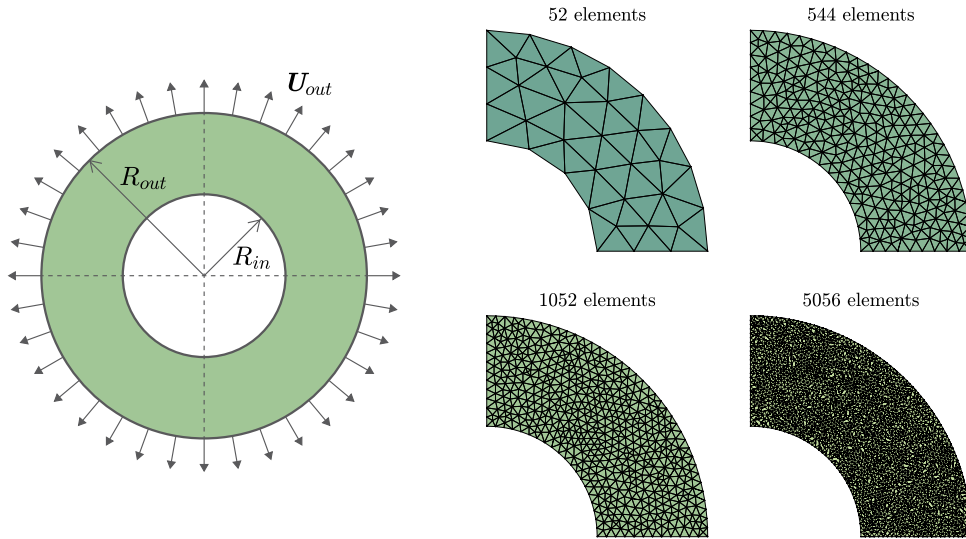
Fig. 5. Inflation of a cylindrical shell: geometry, boundary conditions, and four unstructured meshes.
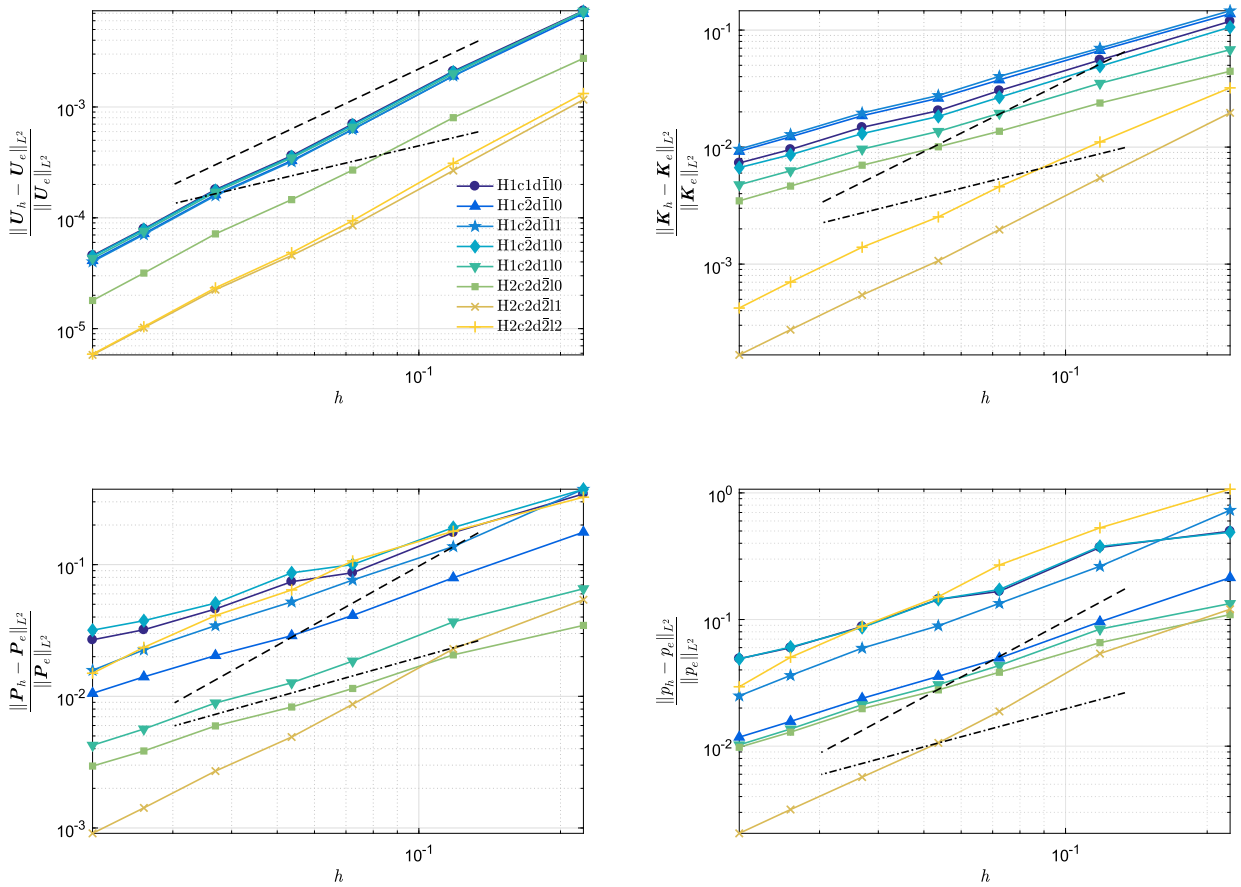

Fig. 6. Relative L^2-norms of errors in approximating displacement, displacement gradient, stress, and pressure versus the maximum diameter h. In each diagram, different curves are associated with different CSFEMs. In each diagram, the dash–dot line and the dashed line have the slopes of 1 and 2, respectively.

To study the convergence order of CSFEMs, we plot the relative errors of the four primary variables versus the maximum diameter h of some unstructured meshes in Fig. 6. Note that our observations in Table 4 also hold for Fig. 6 with regard to accuracy. The convergence order of displacement $\boldsymbol{U}$ is close to 2 for all methods. The convergence order of displacement

Table 4
Convergence and relative error of different CSFEMs for inflation of a cylindrical shell. DOF denotes the degrees of freedom for each mesh, (U_e, F_e, P_e, p_e) is the exact solution, and (U_h, F_h, P_h, p_h) is the approximate solution for each CSFEM.

#	CSFEM	#Elements	#DOF	$\frac{\|U_h - U_e\|_{L2}}{\|U_e\|_{L2}}$	$\frac{\|K_h - K_e\|_{L2}}{\|K_e\|_{L2}}$	$\frac{\|P_h - P_e\|_{L2}}{\|P_e\|_{L2}}$	$\frac{\|p_h - p_e\|_{L2}}{\|p_e\|_{L2}}$
1	H1c1d$\bar{1}$L0	52	646	7.38e-03	1.19e-01	3.45e-01	4.98e-01
		544	6226	7.03e-04	3.04e-02	8.68e-02	1.67e-01
		1052	11902	3.63e-04	2.05e-02	7.43e-02	1.44e-01
		5056	56298	7.95e-05	9.54e-03	3.20e-02	5.98e-02
2	H1c$\bar{2}$d$\bar{1}$L0	52	854	6.97e-03	1.38e-01	1.76e-01	2.14e-01
		544	8402	6.28e-04	3.75e-02	4.11e-02	4.96e-02
		1052	16110	3.28e-04	2.61e-02	2.89e-02	3.56e-02
		5056	76522	7.20e-05	1.22e-02	1.40e-02	1.57e-02
3	H1c$\bar{2}$d$\bar{1}$L1	52	958	7.29e-03	1.46e-01	3.74e-01	7.29e-01
		544	9490	6.27e-04	4.02e-02	7.64e-02	1.34e-01
		1052	18214	3.21e-04	2.76e-02	5.21e-02	8.92e-02
		5056	86634	7.05e-05	1.28e-02	2.25e-02	3.62e-02
4	H1c$\bar{2}$d1L0	52	1028	7.18e-03	1.06e-01	3.73e-01	4.89e-01
		544	10094	6.86e-04	2.66e-02	1.00e-01	1.73e-01
		1052	19348	3.56e-04	1.83e-02	8.66e-02	1.44e-01
		5056	91860	7.84e-05	8.61e-03	3.75e-02	6.06e-02
5	H1c2d1L0	52	1306	7.32e-03	6.80e-02	6.56e-02	1.34e-01
		544	12874	6.57e-04	1.94e-02	1.85e-02	4.34e-02
		1052	24690	3.47e-04	1.36e-02	1.27e-02	3.06e-02
		5056	117310	7.56e-05	6.28e-03	5.64e-03	1.37e-02
6	H2c2d$\bar{2}$L0	52	1688	2.74e-03	4.45e-02	3.45e-02	1.09e-01
		544	16742	2.70e-04	1.37e-02	1.15e-02	3.84e-02
		1052	32136	1.46e-04	1.01e-02	8.29e-03	2.78e-02
		5056	152872	3.17e-05	4.64e-03	3.84e-03	1.29e-02
7	H2c2d$\bar{2}$L1	52	1792	1.16e-03	1.96e-02	5.41e-02	1.21e-01
		544	17830	8.51e-05	1.97e-03	8.70e-03	1.88e-02
		1052	34240	4.57e-05	1.07e-03	4.91e-03	1.06e-02
		5056	162984	1.02e-05	2.75e-04	1.42e-03	3.16e-03
8	H2c2d$\bar{2}$L2	52	1948	1.32e-03	3.21e-02	3.25e-01	1.07
		544	19462	9.42e-05	4.58e-03	1.07e-01	2.69e-01
		1052	37396	4.85e-05	2.53e-03	6.42e-02	1.51e-01
		5056	178152	1.04e-05	7.03e-04	2.35e-02	5.03e-02
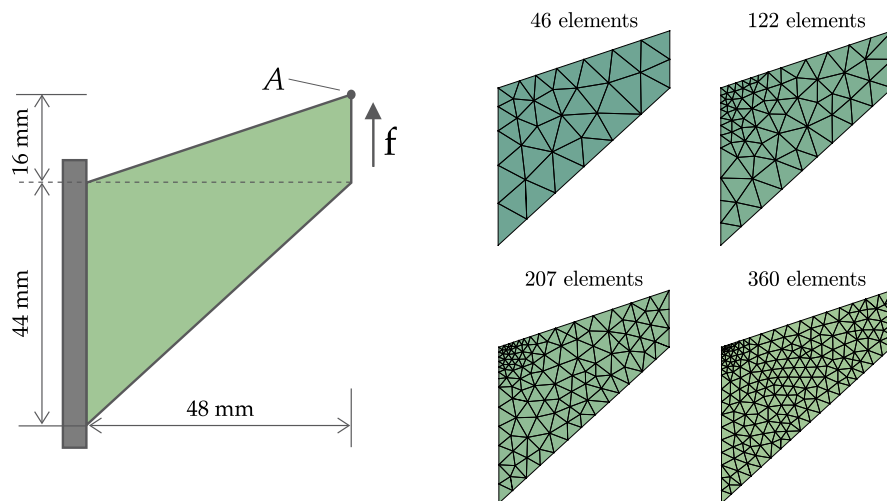
Fig. 7. Cook's membrane: geometry, boundary conditions, and four unstructured meshes.

gradient K is close to 1 for all methods except H2c2d$\bar{2}$L1 and H2c2d$\bar{2}$L2, for which the convergence order is almost 2. For the stress P, the convergence order is close to 1 for all methods except H2c2d$\bar{2}$L1, which has a convergence order of almost 2. We also observe that the convergence order of the pressure-like variable p and the stress P are the same for all methods. Based on the above discussions, we will use H1c1d$\bar{1}$L0 and H2c2d$\bar{2}$L1 in the remaining examples.
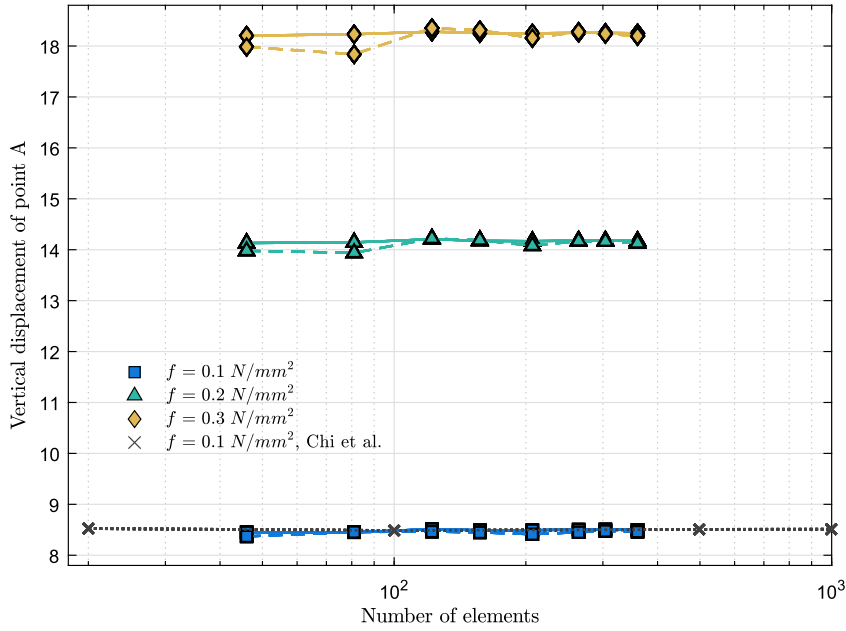
Fig. 8. Cook's membrane: vertical displacement of point *A* in Fig. 7 for different values of the shearing force *f* versus the number of elements in the mesh. The dashed and the solid lines are generated using H1c1d$\bar{1}$L0 and H2c2d$\bar{2}$L1, respectively. The dotted line indicates the results of [10].
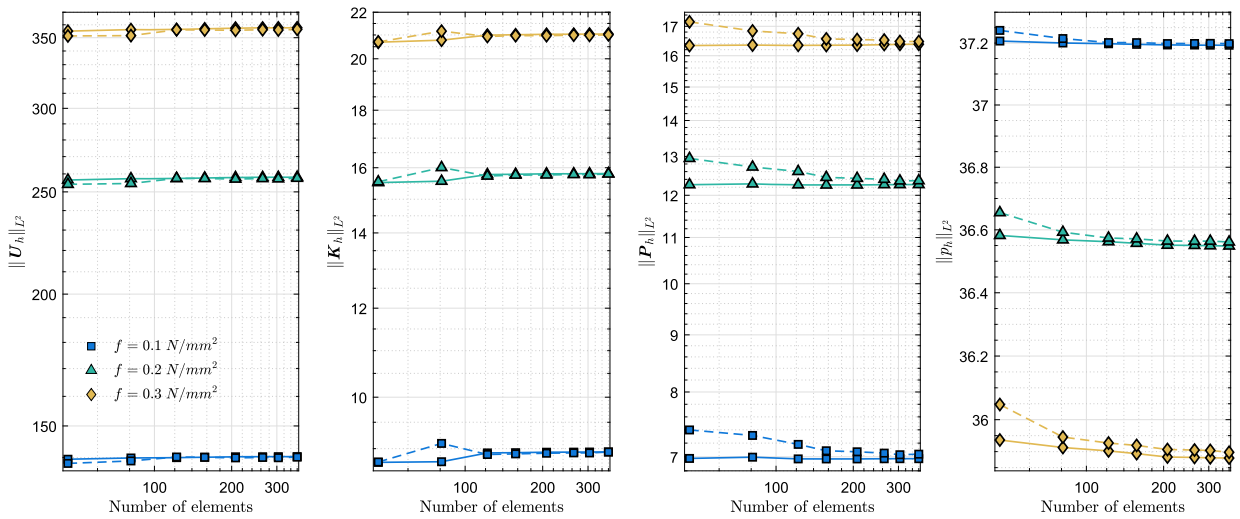
Fig. 9. Cook's membrane: L^2-norms of displacement, displacement gradient, stress, and pressure versus the number of elements in the mesh for different values of the shearing force *f*. The dashed and the solid lines are obtained by using H1c1d$\bar{1}$L0 and H2c2d$\bar{2}$L1, respectively.

Example 2: Cook's membrane To assess the performance of CSFEMs in bending analysis, we consider the standard Cook's membrane problem shown in Fig. 7. We assume $\mu = 1$ N/mm^2 and use the constraint function $C(J) = \ln J$. We investigate the pointwise convergence of H1c1d$\bar{1}$L0 and H2c2d$\bar{2}$L1 in Fig. 8 by plotting the vertical displacement of point *A* indicated in Fig. 7 for different meshes and for different values of the shearing force *f*. We also compare our results with those generated only for $f = 0.1$ N/mm^2 in the work of Chi et al. [10]. We observe that both CSFEMs provide good approximations for relatively coarse meshes and H2c2d$\bar{2}$L1 converges faster than H1c1d$\bar{1}$L0. Also, there is a good agreement between CSFEMs and the method used in [10].

To study convergence, in Fig. 9, we plot the L^2-norms of displacement, displacement gradient, stress, and pressure using H1c1d$\bar{1}$L0 (dashed lines) and H2c2d$\bar{2}$L1 (solid lines) and for different values of shearing force *f*. Considering the four primary variables and for all values of the shearing force *f*, one can see that H2c2d$\bar{2}$L1 converges rapidly. The convergence of H1c1d$\bar{1}$L0 is comparable to that of H2c2d$\bar{2}$L1 in approximating **U** and **K**. However, the convergence of H1c1d$\bar{1}$L0 in approximating **P** and *p* becomes slower than that of H2c2d$\bar{2}$L1 as the value of the shearing force *f* increases.
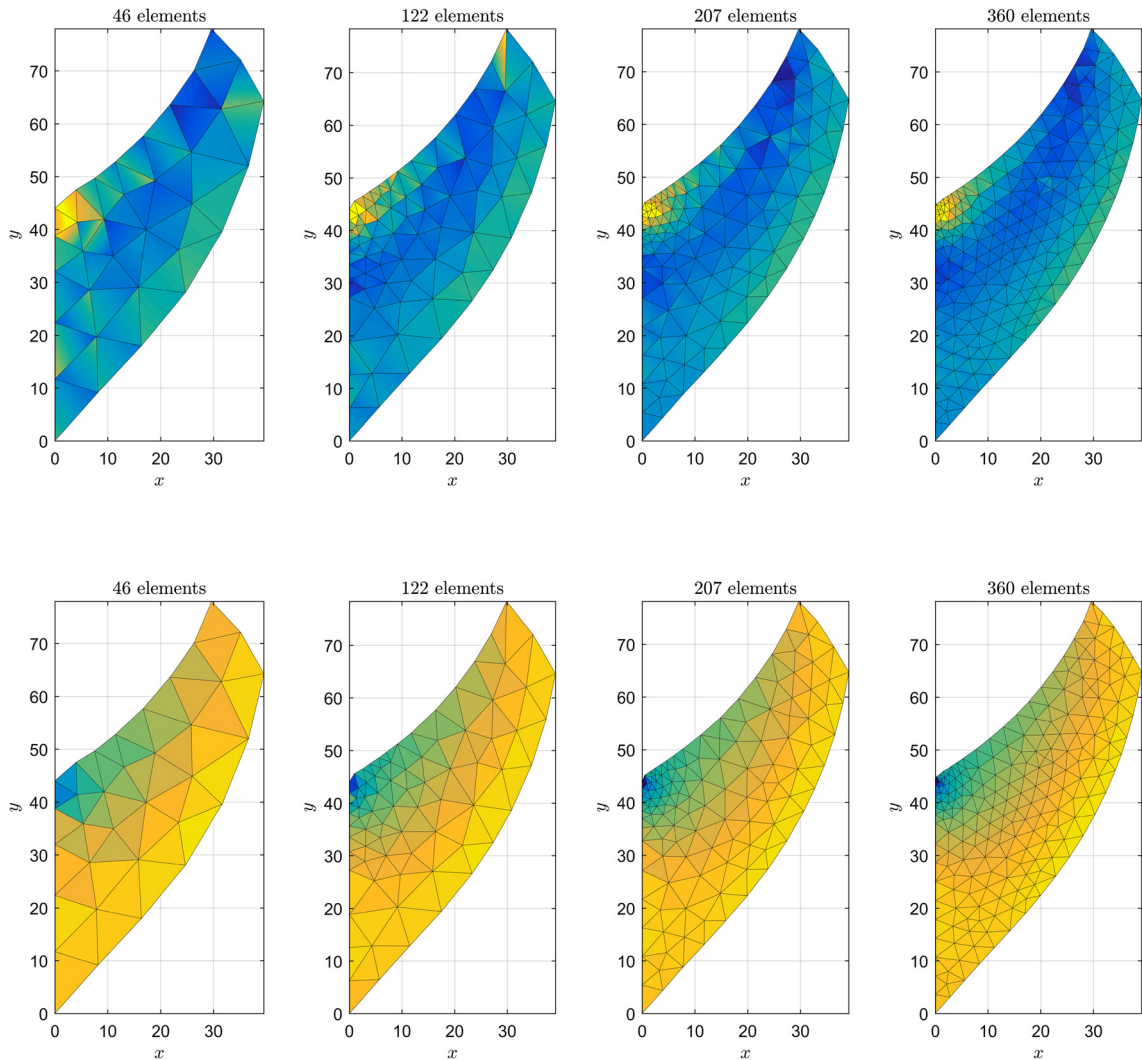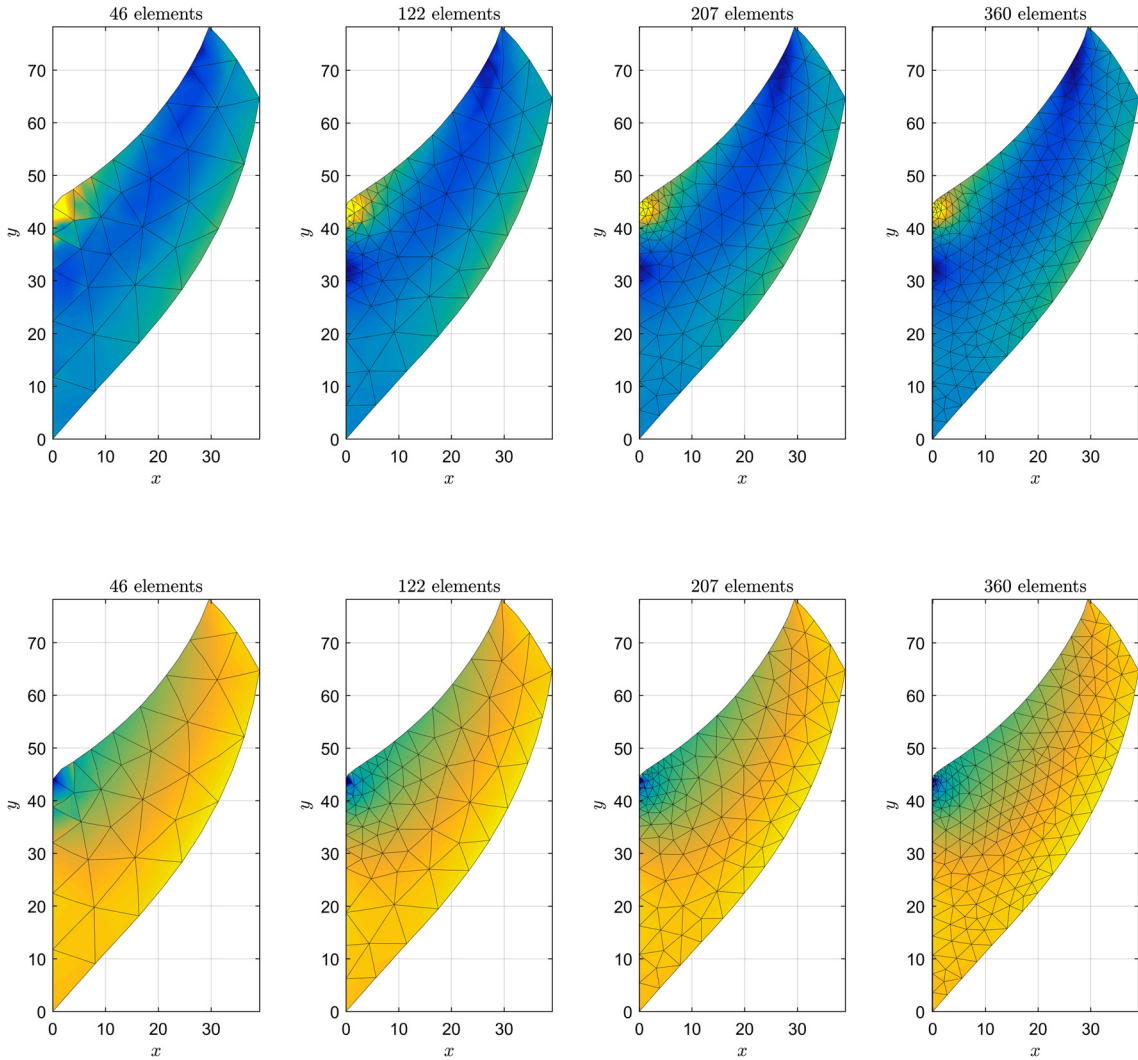
Fig. 10. The deformed configurations of Cook's membrane for the shear force $f = 0.3$ N/mm^2 using H1c1d$\bar{1}$L0. Colors indicate values of $\|\boldsymbol{P}_h\|$ in the first row and pressure p_h in the second row, where lighter colors correspond to larger values. (For interpretation of the references to color in this figure legend, the reader is referred to the web version of this article.)

Figs. 10 and 11 depict the deformed configurations of Cook's membrane for the four meshes of Fig. 7 and $f = 0.3$ N/mm^2 by using H1c1d$\bar{1}$L0 and H2c2d$\bar{2}$L1, receptively. In both figures, colors indicate the values of $\|\boldsymbol{P}_h\|$ in the first row and the values of the pressure p_h in the second row with lighter colors corresponding to larger values. The standard two-field mixed formulation of incompressible elasticity in terms of displacement and pressure is unstable if displacement is approximated by continuous piecewise linear polynomials and pressure with piecewise constant polynomials on triangular elements [26,10]. Although H1c1d$\bar{1}$L0 uses the same low-order polynomial spaces for displacement and pressure, as it can be observed from Fig. 10, it is convergent and does not result in any numerical artifacts in the approximation of pressure. Note that in the mixed formulation of CSFEMs such as H1c1d$\bar{1}$L0, displacement and pressure are not coupled directly with a bilinear term. In addition, comparing with the standard two-field mixed FEMs, H1c1d$\bar{1}$L0 provides a more accurate approximation of strain and stress by approximating them directly in their domains of definition. In Fig. 11, one observes the fast convergence of H2c2d$\bar{2}$L1 in approximating stress and pressure and its accuracy even for a coarse mesh with 46 elements.

Example 3: bending of an arch Following [16], for further testing of H1c1d$\bar{1}$L0 and H2c2d$\bar{2}$L1 in bending problems, we consider bending of the arch shown in Fig. 12. Note that f in Fig. 12 is a uniformly distributed load in the radial direction. We assume $E = 250$ N/mm^2 and $\nu = 0.5$ ($\mu = E/2(1 + \nu)$) and use $C(J) = \ln J$ as the constraint function. Because of the symmetry, we study half of the arch as shown in the generated meshes in Fig. 12. Fig. 13 shows the reference and the deformed states of the arch subjected to $f = 20$ N/mm^2 using H2c2d$\bar{2}$L1 and the mesh with 324 elements in Fig. 12. The colors indicate the values of $\|\boldsymbol{K}_h\|$ with lighter colors corresponding to larger values. As one expects, the middle portion of the half of the arch at $x = 0.3$ ($x = -0.3$) is narrowed and stretched, and hence, shows large values of $\|\boldsymbol{K}_h\|$.

Fig. 11. The deformed configurations of Cook's membrane for the shear force $f = 0.3$ N/mm^2 using H2c2d$\bar{2}$L1. Colors indicate values of $\|\boldsymbol{P}_h\|$ in the first row and pressure p_h in the second row, where lighter colors correspond to larger values. (For interpretation of the references to color in this figure legend, the reader is referred to the web version of this article.)

Fig. 14 shows the convergence of H1c1d$\bar{1}$L0 (dashed lines) and H2c2d$\bar{2}$L1 (solid lines) for different values of the load f. We observe that both methods converge considering all the four primary fields and for all values of the transverse load f. However, H2c2d$\bar{2}$L1 has a faster convergence, and hence provides a more accurate approximation when using coarse meshes. Fig. 15 shows the deformed configurations of half of the arch for $f = 20$ N/mm^2 using the meshes of Fig. 12. The results are generated using H2c2d$\bar{2}$L1 and colors indicate the values of $\|\boldsymbol{P}_h\|$ in the first row and p_h in the second row, where lighter colors correspond to higher values. Comparing the mesh with 71 elements with the mesh with 998 elements, one can see the accuracy of H2c2d$\bar{2}$L1 in approximating stress and pressure even when using a coarse mesh.

Example 4: stretching a block with a hole at its center We consider a square block with a hole at its center as shown in Fig. 16. The block is subjected to uniform displacement boundaries of $(u, 0)$ at its right and $(-u, 0)$ at its left edge. The top and bottom edges are traction free. The goal of this example is to test the performance of CSFEMs at very large stretches. We assume $\mu = 1$ N/mm^2 and use $C(J) = J - 1$. Due to symmetry, we consider only a quarter of the block as shown in the generated meshes in Fig. 16. Fig. 17 illustrates the reference and the deformed configurations of the block using H2c2d$\bar{2}$L1 and the mesh with 184 elements in Fig. 16. The boundary displacement $u = 1.5$ mm results in a large stretch of 4. The colors indicate the values of $\|\boldsymbol{K}_h\|$ with lighter colors associated with larger values. The maximum of $\|\boldsymbol{K}_h\|$ is 6.5 at the boundary of the hole and $x = 0$. Fig. 18 illustrates the convergence of H1c1d$\bar{1}$L0 (dashed lines) and H2c2d$\bar{2}$L1 (solid lines) for different values of the imposed boundary displacement u. We observe that H2c2d$\bar{2}$L1 converges rapidly considering all the primary variables and for all values of u. Also, considering displacement, displacement gradient, and stress, H1c1d$\bar{1}$L0 has a good convergence, but it has a poor performance in approximating pressure for *stretch* $= 4$ ($u = 1.5$ mm). Fig. 19 shows
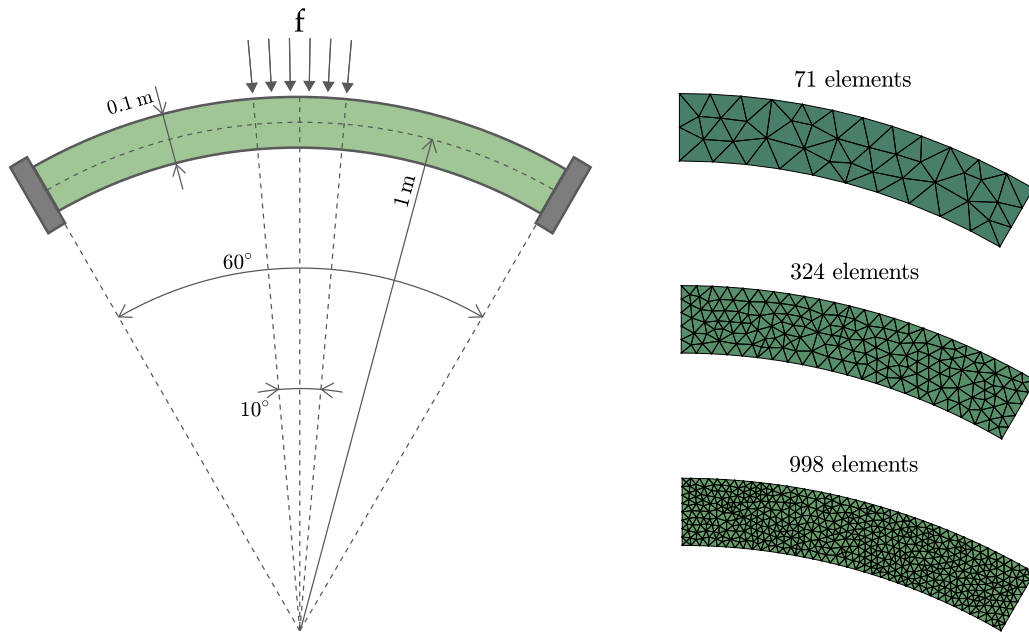
Fig. 12. Bending of an arch: geometry, boundary conditions, and three unstructured meshes.
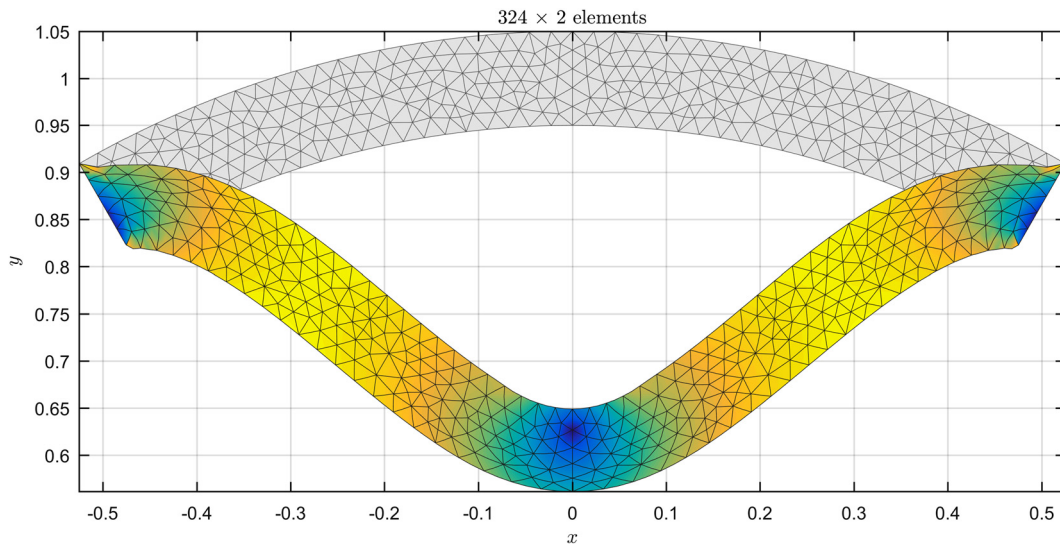
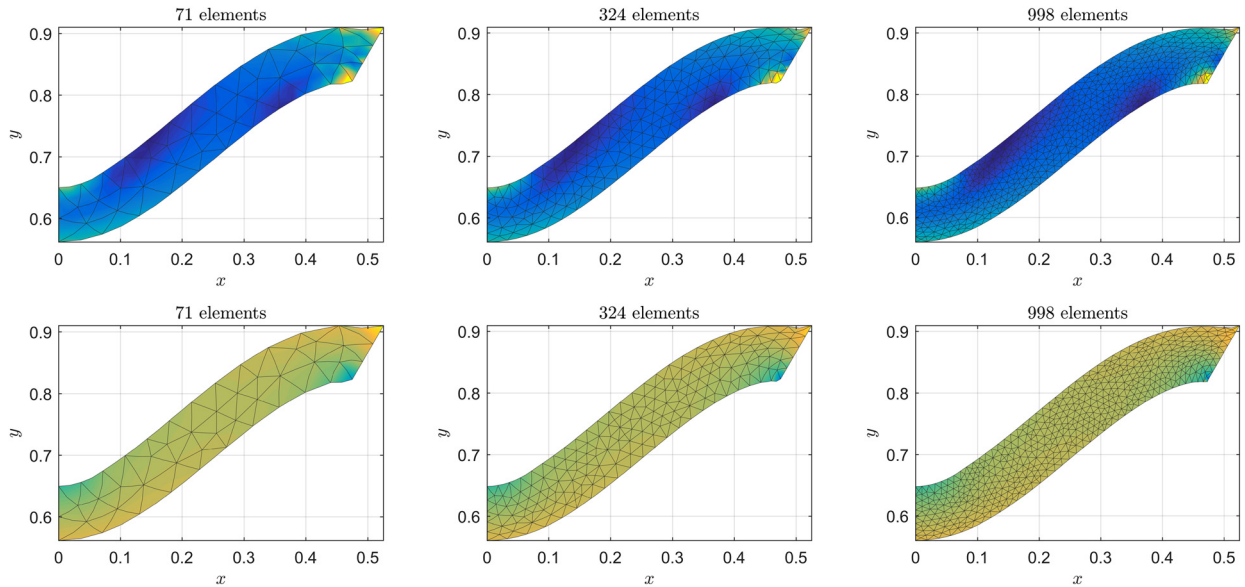**Fig. 13.** The reference and deformed configurations of the arch for the bending load $f = 20$ N/mm^2 using H2c2d$\bar{2}$L1. Colors indicate values of the norm of displacement gradient $\|\boldsymbol{K}_h\|$, where lighter colors correspond to larger values. (For interpretation of the references to color in this figure legend, the reader is referred to the web version of this article.)

the deformed configurations of a quarter of the block for $u = 1.5$ mm using the meshes of Fig. 16. The results are obtained using H2c2d$\bar{2}$L1 and colors indicate the values of $\|\boldsymbol{P}_h\|$ in the first column and p_h in the second column, where lighter colors correspond to higher values. As one can observe, even for *stretch* $= 4$ and using a coarse mesh with 48 elements, H2c2d$\bar{2}$L1 provides an accurate distribution of stress and pressure.

Example 5: stretching a block with randomly distributed holes   Next, we consider a block with randomly distributed holes as shown in Fig. 20. The size of the block is 1 mm × 1 mm. The left edge of the block is fixed and the right edge is subjected to a uniform displacement boundary $(u, 0)$. The top and the bottom edges are traction free. Similar to the previous example, this example tests the performance of CSFEMs at very large stretches but for a more complex geometry. We again consider $\mu = 1$ N/mm^2 and $C(J) = J - 1$. Fig. 21 shows the reference and the deformed configurations of the block using H2c2d$\bar{2}$L1 and the mesh with 184 elements in Fig. 20. The colors indicate the values of $\|\boldsymbol{K}_h\|$, where lighter colors correspond to larger values. The large values of $\|\boldsymbol{K}_h\|$ correspond to the boundaries of the middle portion of the holes with maximum $\|\boldsymbol{K}_h\|$ of
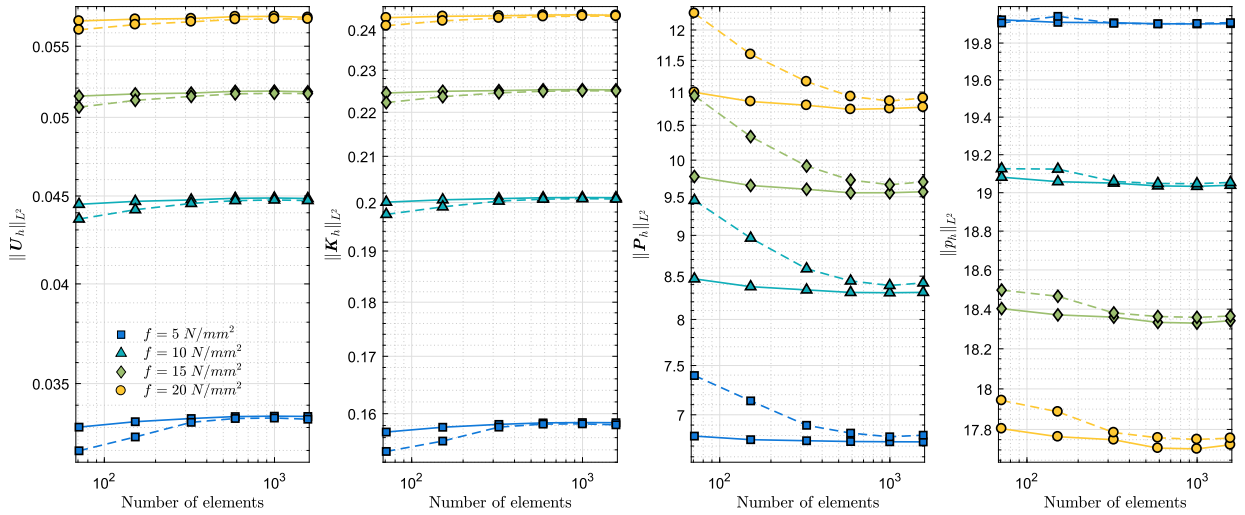
Fig. 14. Bending of an arch: L^2-norms of displacement, displacement gradient, stress, and pressure versus the number of elements in the mesh for different values of the bending force f. The dashed and the solid lines are obtained using H1c1d$\bar{1}$L0 and H2c2d$\bar{2}$L1, respectively.

Fig. 15. The deformed configurations of the arch for the bending load $f = 20$ N/mm^2 using H2c2d$\bar{2}$L1. Colors indicate values of the norm of stress $\|P_h\|$ in the first row and the pressure p_h in the second row, where lighter colors correspond to larger values. For interpretation of the references to color in this figure legend, the reader is referred to the web version of this article.)

approximately 5.5 at $(0.6, 0.5)$. Fig. 22 illustrates the convergence of H1c1d$\bar{1}$L0 (dashed lines) and H2c2d$\bar{2}$L1 (solid lines) for different values of u. We observe that H2c2d$\bar{2}$L1 converges considering the four primary variables and for all values of u. We also see that H1c1d$\bar{1}$L0 has good convergence, in general, but it becomes inaccurate in approximating pressure with the increase of stretch to 3 ($u = 2$ mm). Note that we had similar observations in Fig. 14. Using the meshes of Fig. 20 and using H2c2d$\bar{2}$L1, in Fig. 23 we illustrate the deformed configurations of the block for $u = 2$ mm. The colors indicate the values of $\|P_h\|$ in the first column and p_h in the second column with lighter colors corresponding to higher values. This mainly shows the stability of H2c2d$\bar{2}$L1 in approximating the stress and pressure without any numerical artifacts even for a complex geometry under a large stretch.

Example 6: rubber reinforced with rigid particles   As was discussed in Remark 12, the discrete fields $K_h \in \check{V}^{\mathbf{c}}_{h,r}$ and $P_h \in \check{V}^{\mathbf{d}}_{h,r}$ naturally satisfy, respectively, the Hadamard jump condition and the continuity of traction on all the internal edges of any mesh. This enables one to accurately model heterogeneous solids in which inhomogeneities do not slide at the interfaces, i.e., the displacement field is continuous at the interfaces. More specifically, we generate a mesh for the entire heterogeneous material such that the interfaces between all inhomogeneities lie completely on some internal edges of the mesh. Then we
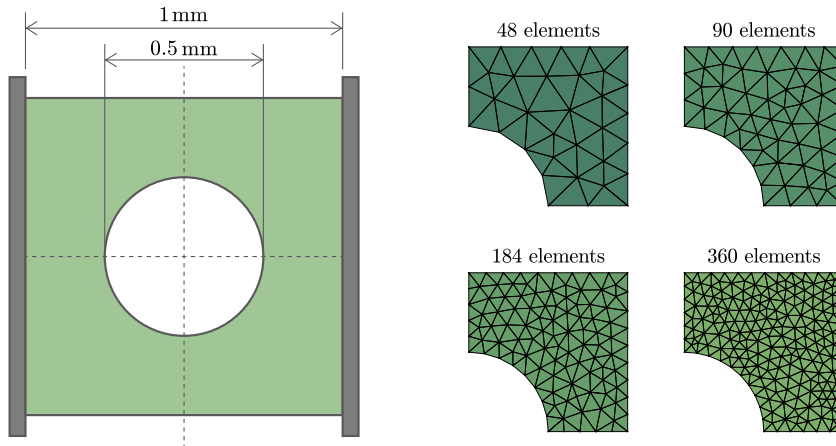
Fig. 16. Stretching a block with a hole at its center: geometry, boundary conditions, and four unstructured meshes.
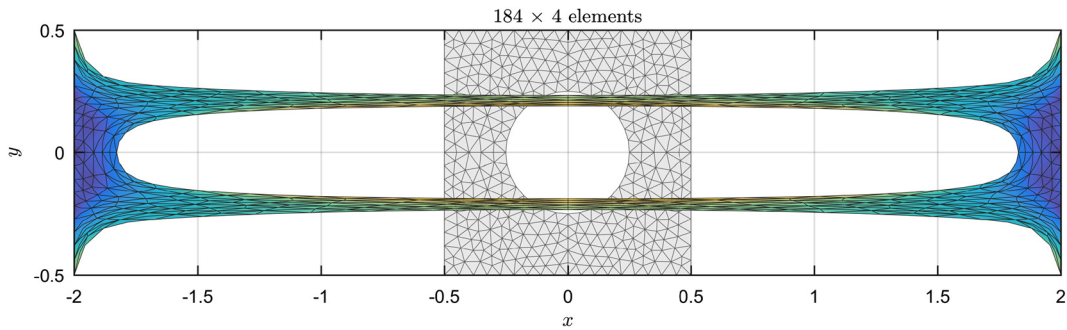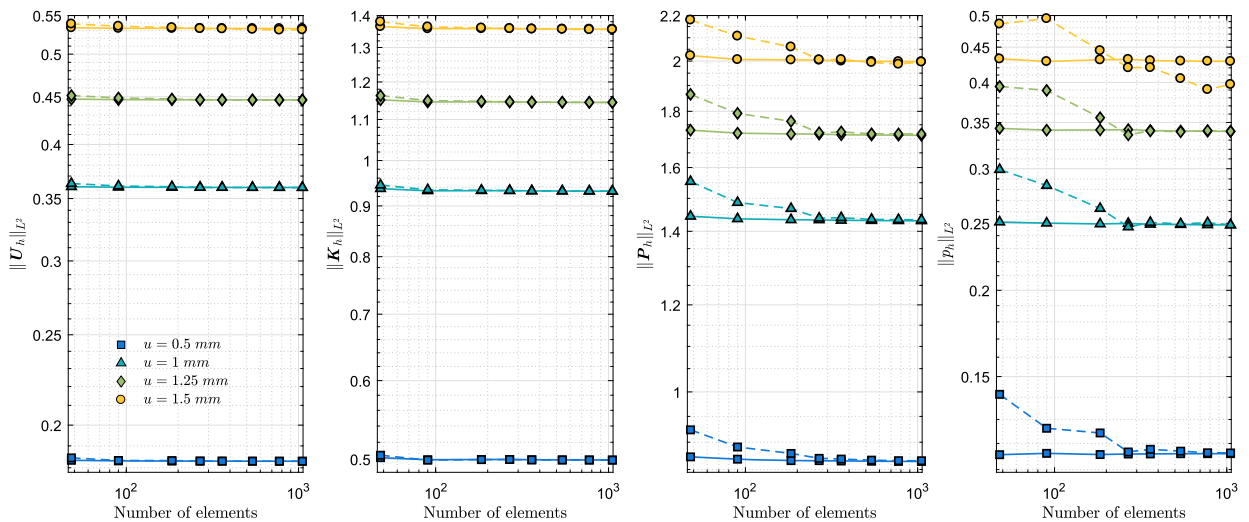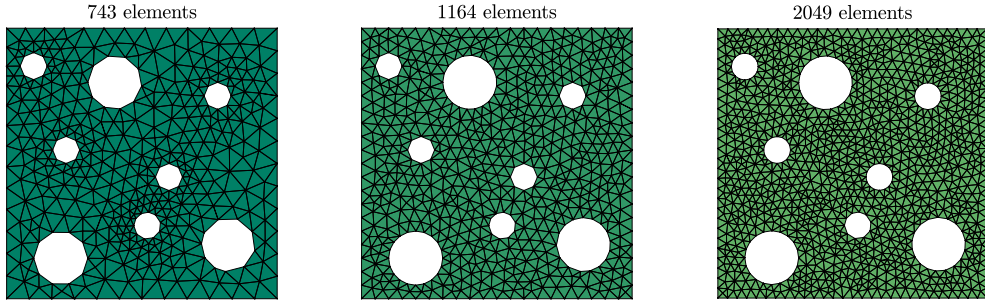

Fig. 17. The reference and deformed configurations of a block with a hole for $u = 1.5$ mm (*stretch* $= 4$) obtained by using H2c2d$\bar{2}$L1. Colors indicate values of the norm of displacement gradient $\|\boldsymbol{K}_h\|$, where lighter colors correspond to larger values such that max $\|\boldsymbol{K}_h\| = 6.5$ is indicated by yellow. (For interpretation of the references to color in this figure legend, the reader is referred to the web version of this article.)
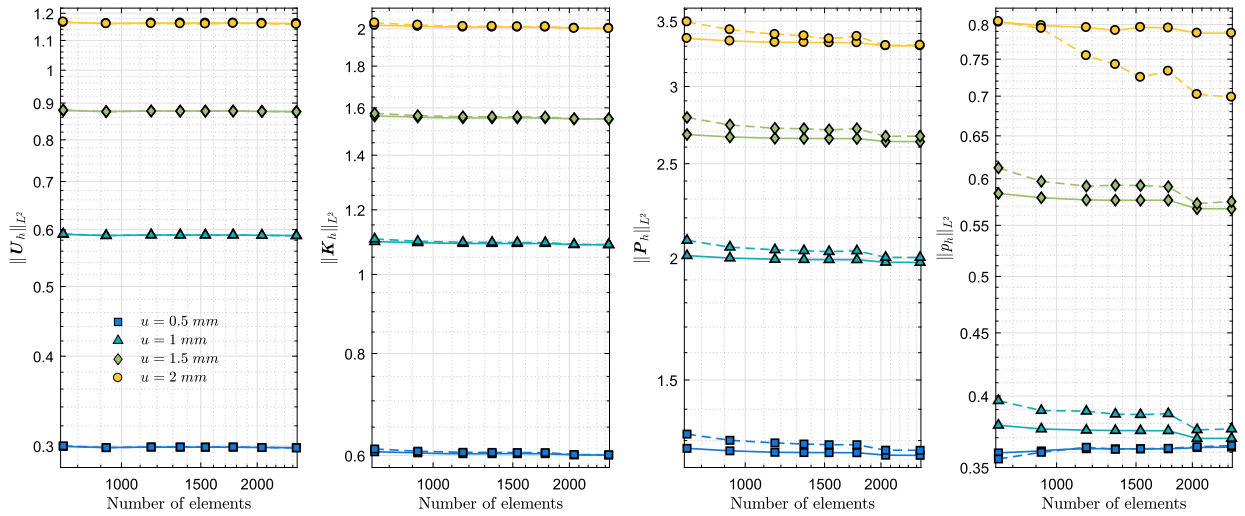

Fig. 18. Stretching a block with a hole at its center: L^2-norms of displacement, displacement gradient, stress, and pressure versus the number of elements in the mesh. u in the legend is the horizontal displacement imposed at the right boundary. The left boundary is subjected to $-u$ simultaneously. The dashed and solid lines are generated by using H1c1d$\bar{1}$L0 and H2c2d$\bar{2}$L1, respectively.
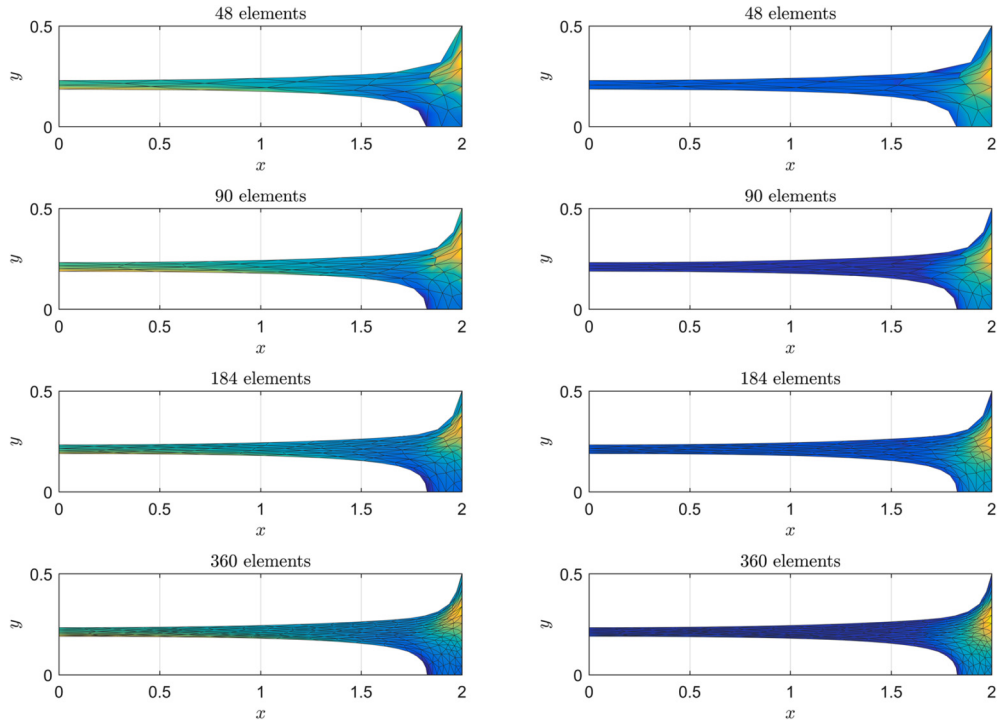
Fig. 19. The deformed configurations of a quarter of a block with a hole for $u = 1.5$ mm (*stretch* $= 4$) using H2c2d$\bar{2}$L1. Colors indicate values of the norm of stress $\|\boldsymbol{P}_h\|$ in the first column and the pressure p_h in the second column, where lighter colors correspond to larger values. (For interpretation of the references to color in this figure legend, the reader is referred to the web version of this article.)

Fig. 20. Three unstructured meshes for a square block with randomly distributed holes.
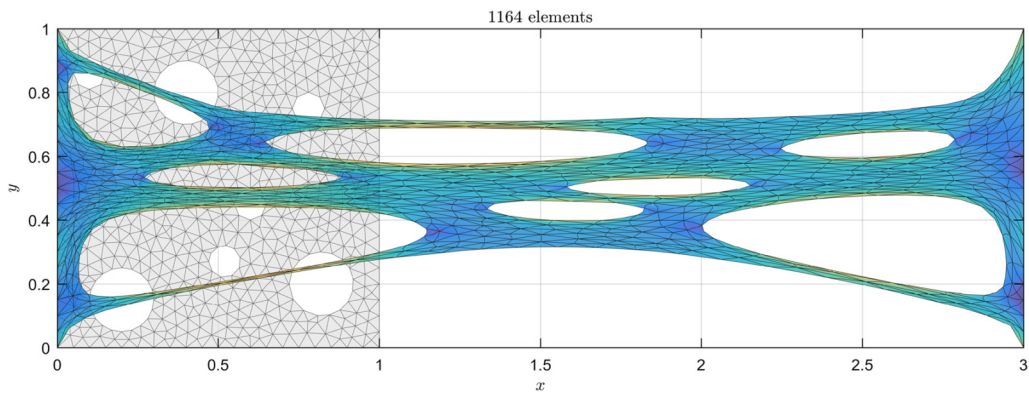
Fig. 21. The reference and deformed configurations of the block with randomly distributed holes for $u = 2$ mm (*stretch* $= 3$) obtained using H2c2d$\bar{2}$L1. Colors indicate values of the norm of displacement gradient $\|\boldsymbol{K}_h\|$, where lighter colors correspond to larger values such that max $\|\boldsymbol{K}_h\| = 5.5$ is indicated by yellow. (For interpretation of the references to color in this figure legend, the reader is referred to the web version of this article.)

Fig. 22. Stretching a block with randomly distributed holes: L^2-norms of displacement, displacement gradient, stress, and pressure versus the number of elements in the mesh. u in the legend stands for the horizontal displacement imposed at the right boundary. The dashed and solid lines are generated using H1c1d$\bar{1}$L0 and H2c2d$\bar{2}$L1, respectively.
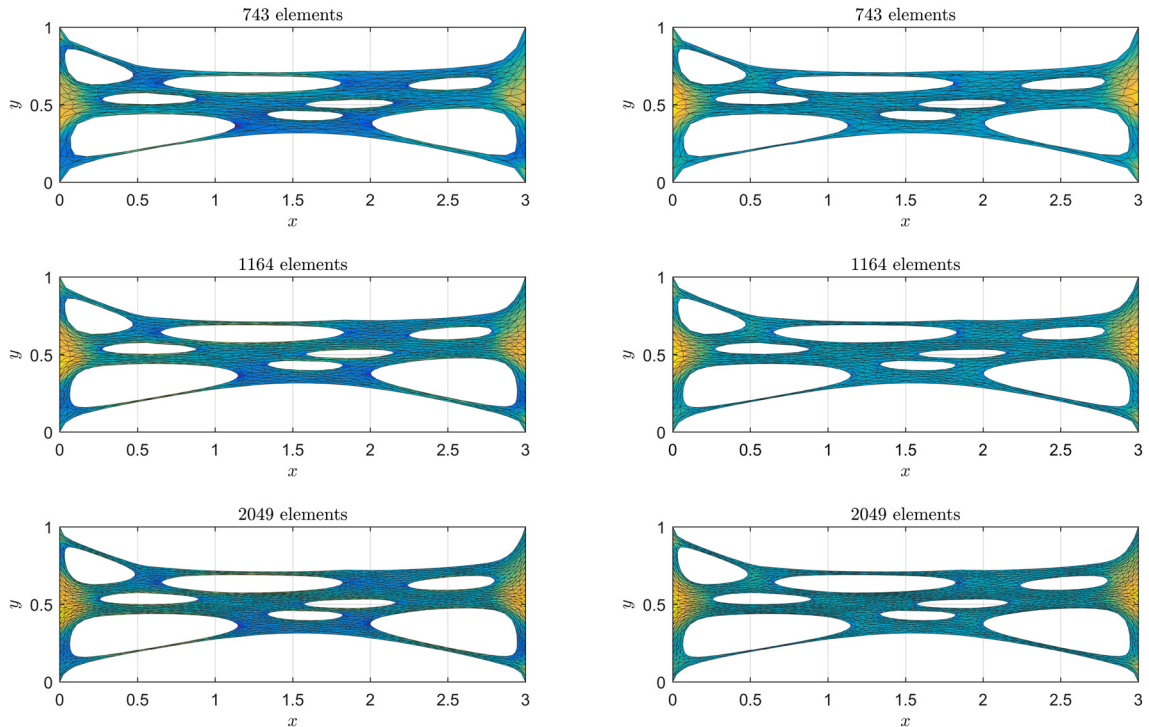

Fig. 23. The deformed configurations of the block for $u = 2$ mm (*stretch* $= 3$) using H2c2d$\bar{2}$L1. Colors indicate values of the norm of stress $\|\boldsymbol{P}_h\|$ in the first column and the pressure p_h in the second column, where lighter colors correspond to larger values. (For interpretation of the references to color in this figure legend, the reader is referred to the web version of this article.)

assign a different material model to the patch of elements within each inhomogeneity. Regardless of the refinement level of the generated mesh, CSFEMs naturally satisfy all the interface conditions of the heterogeneous solid at the discrete level.

As an application, we consider a square rubber block with edge length of 1 mm reinforced with 16 rigid circular particles with area fraction of 20% as it is shown in Fig. 24. The left and the right edges of the block are subjected to uniform traction $(-f, 0)$ and $(0, f)$, respectively, and the top and the bottom edges are traction free. We consider $\mu_1 = 1$ N/mm^2 for the rubber matrix and $\mu_2 = 1e5$ N/mm^2 for the rigid particles, and we use $C(J) = J - 1$ for both of them.

Fig. 25 shows the deformed configuration of the block for the tension load $f = 2.8$ N/mm^2 using H2c2d$\bar{2}$L1 and the mesh with 4428 elements given in Fig. 24. We can see that the stretch due to the imposed boundary tractions is larger than 2. In
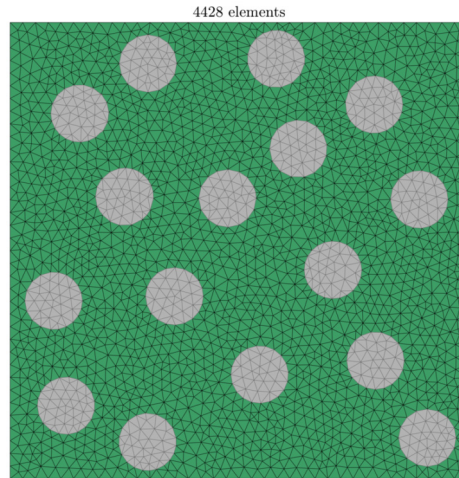
Fig. 24. An unstructured mesh for a square rubber block with 16 particles with 20% area fraction.
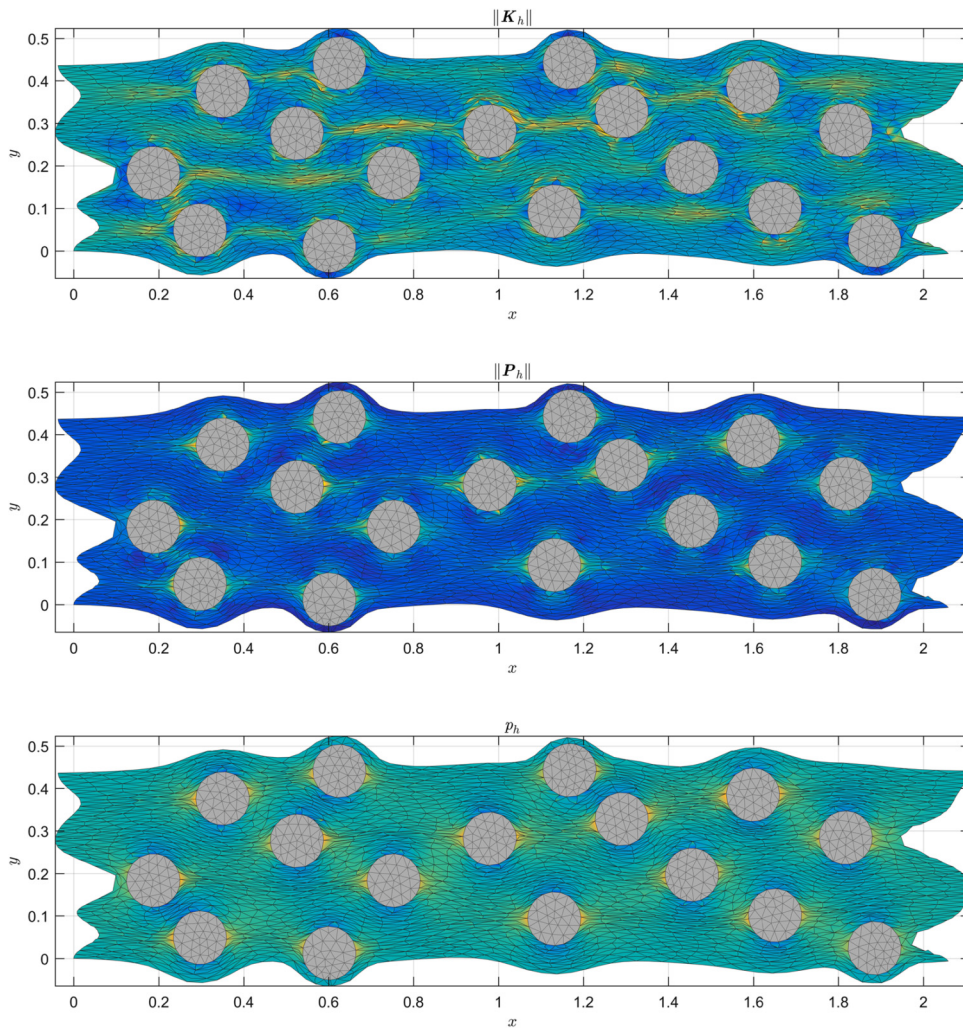

Fig. 25. The deformed configuration of the block for $f = 2.8$ N/mm^2 using H2c2d2L1 and the mesh with 4428 elements given in Fig. 24. Colors on the matrix indicate values of the norm of displacement gradient in the first plot, the norm of stress in the second plot, and pressure in the third plot with lighter colors corresponding to larger values. (For interpretation of the references to color in this figure legend, the reader is referred to the web version of this article.)
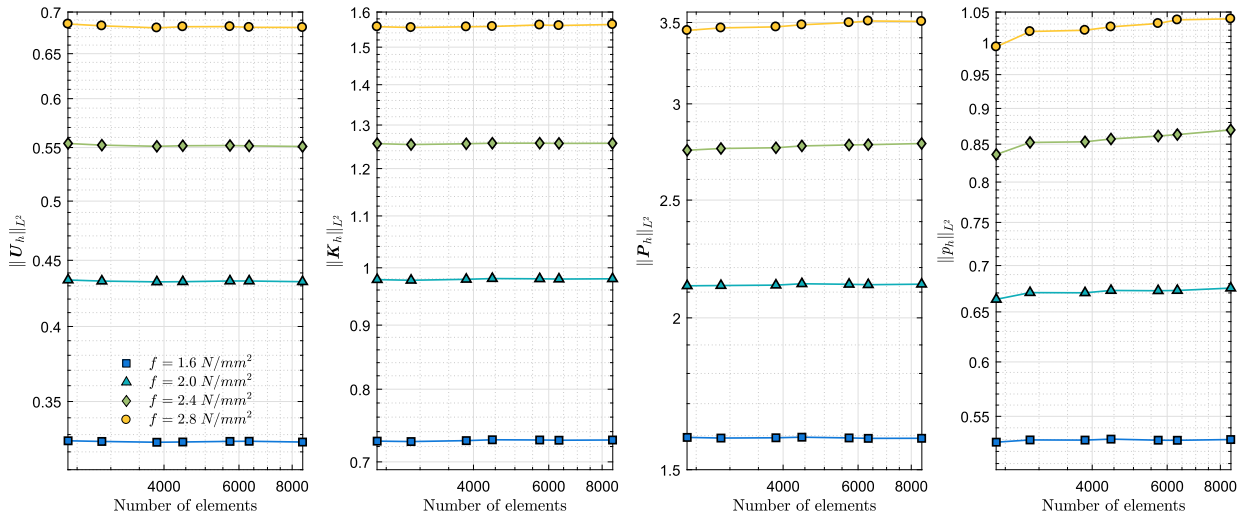
Fig. 26. Rubber reinforced with rigid particles: L^2-norms of displacement over the entire domain and L^2-norms of displacement gradient, stress, and pressure over the matrix versus the number of elements in the mesh. The results are generated by using H2c2d2̄L1.

the first plot, colors on the matrix indicate values of the norm of the displacement gradient $\|\boldsymbol{K}_h\|$. As one expects, $\boldsymbol{K}_h = \boldsymbol{0}$ everywhere in the rigid particles. Furthermore, we observe that the large values of $\|\boldsymbol{K}_h\|$ occur in the portion of the matrix between two rigid particles of almost same vertical positions that were close to one another before deformation. In the second plot, colors on the matrix indicate values of the norm of stress $\|\boldsymbol{P}_h\|$. As can be seen, those points of the matrix at the left and right sides of every particle have the large values of stress. The third plot shows the values of pressure p_h in the matrix. Everywhere in the particles, the computed value of p_h is almost $-\mu_2$. We observe that the positions of large values of pressure and stress in the matrix are almost the same; this is consistent with our observations of all the previous examples. Fig. 26 shows that H2c2d2̄L1 is convergent for different values of f.

5. Concluding remarks

We introduced a new class of mixed finite element methods for incompressible nonlinear elasticity – *compatible-strain mixed finite element methods* (CSFEMs). This work is an extension of [17] to incompressible nonlinear elasticity. Furthermore, this work improves [17] by providing a more practical description of the mixed formulations and the finite element approximations, especially, a more efficient way to calculate the shape functions. We derived a four-field mixed formulation from a Hu–Washizu type functional with the displacement $\boldsymbol{U}$, the displacement gradient $\boldsymbol{K}$, the first Piola–Kirchhoff stress tensor $\boldsymbol{P}$, and a pressure-like field p as the four independent unknowns. For solution spaces, we assumed $(\boldsymbol{U}, \boldsymbol{K}, \boldsymbol{P}, p) \in H^1(T\mathcal{B}) \times H^{\mathbf{c}}(\mathcal{B}) \times H^{\mathbf{d}}(\mathcal{B}) \times L^2(\mathcal{B})$, and to define the corresponding test spaces, we used the same Hilbert spaces. Next, we constructed some conforming finite element (piecewise polynomial) subspaces $V_{h,r}^1 \subset H^1(T\mathcal{B}_h)$, $\check{V}_{h,r}^{\mathbf{c}} \subset H^{\mathbf{c}}(\mathcal{B}_h)$, $\check{V}_{h,r}^{\mathbf{d}} \subset H^{\mathbf{d}}(\mathcal{B}_h)$, and $V_{h,r}^\ell \subset L^2(\mathcal{B}_h)$. Then, CSFEMs were obtained by replacing the solution and test spaces of the four-field mixed formulation with the generated finite element subspaces. Due to interelement continuities of these subspaces, regardless of the refinement level of the mesh, CSFEMs approximate a continuous displacement and satisfy both the Hadamard compatibility condition of displacement gradient and the continuity of traction on all the internal edges.

After solving several numerical examples, we observed that CSFEMs are robust and have good performance for different geometries and loadings. In particular, CSFEMs perform well in bending problems, do not result in an unphysical approximation of pressure even when using piecewise constant polynomials, and do not suffer from numerical artifacts such as locking, checkerboarding of pressure, or hourglass-type instabilities. In capturing the nonlinear effects, we observed that CSFEMs remain stable up to very large strains and provide an accurate approximation of stress as an independent variable. Moreover, as we demonstrated, CSFEMs provide an efficient framework for modeling inhomogeneous solids undergoing large deformations.

In future communications, we will extend CSFEMs to 3D compressible and incompressible nonlinear elasticity by using $H^{\mathbf{c}}$ and $H^{\mathbf{d}}$-conforming tetrahedral elements. Moreover, we will investigate the applicability of CSFEMs in modeling nonlinear solids with distributed finite eigenstrains. Eigenstrains are created due to a host of anelastic phenomena in solids such as defects [38], thermal strains [39], biological growth [40], swelling [41], and the presence of inclusions and inhomogeneities [42,43]. In particular, we will use the geometric formulation of anelasticity, in which all the anelastic effects are buried into the material manifold. In this approach, if one can build a material manifold (where the body is stress-free by construction), then the anelasticity problem is transformed to a classical nonlinear elasticity problem provided that the nontrivial geometry of the material manifold is taken into consideration properly.

Acknowledgements

References

[1] O.A. Ladyzhenskaya, The Mathematical Theory of Viscous Incompressible Flow, Gordon and Breach Science Publishers, New York, 1969.
[2] I. Babuška, The finite element method with Lagrangian multipliers, Numer. Math. 20 (1973) 179–192.
[3] F. Brezzi, On the existence, uniqueness and approximation of saddle-point problems arising from Lagrange multipliers, RAIRO. Anal. Numér. (1974) 129–151.
[4] D.N. Arnold, F. Brezzi, M. Fortin, A stable finite element for the Stokes equations, Calcolo 21 (4) (1984) 337–344.
[5] C. Taylor, P. Hood, A numerical solution of the Navier–Stokes equations using the finite element technique, Comput. Fluids 1 (1) (1973) 73–100.
[6] R.E. Nickell, R.I. Tanner, B. Caswell, The solution of viscous incompressible jet and free-surface flows using finite-element methods, J. Fluid Mech. 65 (1) (1974) 189–206.
[7] M. Bercovier, O. Pironneau, Error estimates for finite element method solution of the Stokes problem in the primitive variables, Numer. Math. 33 (2) (1979) 211–224.
[8] M. Crouzeix, P.-A. Raviart, Conforming and nonconforming finite element methods for solving the stationary Stokes equations I, Rev. Fr. Autom. Inform. Rech. Opér. Math. 7 (R3) (1973) 33–75.
[9] F. Auricchio, L. da Veiga Beirao, C. Lovadina, A. Reali, R.L. Taylor, P. Wriggers, Approximation of incompressible large deformation elastic problems: some unresolved issues, Comput. Mech. 52 (2013) 1153–1167.
[10] H. Chi, C. Talischi, O. Lopez-Pamies, G.H. Paulino, Polygonal finite elements for finite elasticity, Int. J. Numer. Methods Eng. 101 (4) (2015) 305–328.
[11] T.J.R. Hughes, L.P. Franca, M. Balestra, A new finite element formulation for computational fluid dynamics: V. Circumventing the Babuška–Brezzi condition: a stable Petrov–Galerkin formulation of the Stokes problem accommodating equal-order interpolations, Comput. Methods Appl. Mech. Eng. 59 (1) (1986) 85–99.
[12] L.P. Franca, T.J.R. Hughes, A.F.D. Loula, I. Miranda, A new family of stable elements for nearly incompressible elasticity based on a mixed Petrov–Galerkin finite element formulation, Numer. Math. 53 (1) (1988) 123–141.
[13] J.C. Simo, R.L. Taylor, K.S. Pister, Variational and projection methods for the volume constraint in finite deformation elasto-plasticity, Comput. Methods Appl. Mech. Eng. 51 (1–3) (1985) 177–208.
[14] J.C. Simo, F. Armero, Geometrically non-linear enhanced strain mixed methods and the method of incompatible modes, Int. J. Numer. Methods Eng. 33 (1992) 1413–1449.
[15] J.A. Weiss, B.N. Maker, S. Govindjee, Finite element implementation of incompressible, transversely isotropic hyperelasticity, Comput. Methods Appl. Mech. Eng. 135 (1–2) (1996) 107–128.
[16] B.P. Lamichhane, A mixed finite element method for non-linear and nearly incompressible elasticity based on biorthogonal systems, Int. J. Numer. Methods Eng. 79 (7) (2009) 870–886.
[17] A. Angoshtari, M. Faghih Shojaei, A. Yavari, Compatible-strain mixed finite element methods for 2D compressible nonlinear elasticity, Comput. Methods Appl. Mech. Eng. 313 (2017) 596–631.
[18] A. Angoshtari, A. Yavari, Differential complexes in continuum mechanics, Arch. Ration. Mech. Anal. 216 (2015) 193–220.
[19] A. Angoshtari, A. Yavari, Hilbert complexes of nonlinear elasticity, Z. Angew. Math. Phys. 67 (6) (2016) 143.
[20] D.N. Arnold, R. Winther, Mixed finite elements for elasticity, Numer. Math. 92 (2002) 401–419.
[21] D.N. Arnold, R.S. Falk, R. Winther, Mixed finite element methods for linear elasticity with weakly imposed symmetry, Math. Comput. 76 (260) (2007) 1699–1723.
[22] P. Hauret, F. Hecht, A discrete differential sequence for elasticity based upon continuous displacements, SIAM J. Sci. Comput. 35 (1) (2013) B291–B314.
[23] A. Pechstein, J. Schöeberl, Tangential-displacement and normal–normal-stress continuous mixed finite elements for elasticity, Math. Models Methods Appl. Sci. 21 (08) (2011) 1761–1782.
[24] A. Yavari, Compatibility equations of nonlinear elasticity for non-simply-connected bodies, Arch. Ration. Mech. Anal. 209 (2013) 237–253.
[25] P.G. Ciarlet, The Finite Element Method for Elliptic Problems, North-Holland Publishing Co., Amsterdam, 1978.
[26] A. Ern, J. Guermond, Theory and Practice of Finite Elements, Springer-Verlag, New York, 2004.
[27] J.C. Nédélec, Mixed finite elements in $\mathbb{R}^3$, Numer. Math. 35 (3) (1980) 315–341.
[28] J.C. Nédélec, A new family of mixed finite elements in $\mathbb{R}^3$, Numer. Math. 50 (1986) 57–81.
[29] P.A. Raviart, J.M. Thomas, A mixed finite element method for 2nd order elliptic problems, in: Mathematical Aspects of Finite Element Methods, Proc. Conf., Consiglio Naz. delle Ricerche (C.N.R.), Rome, 1975, in: Lecture Notes in Mathematics, vol. 606, Springer, Berlin, 1977, pp. 292–315.
[30] F. Brezzi, J. Douglas Jr., L.D. Marini, Two families of mixed finite elements for second order elliptic problems, Numer. Math. 47 (1985) 217–235.
[31] D.N. Arnold, R.S. Falk, R. Winther, Geometric decompositions and local bases for spaces of finite element differential forms, Comput. Methods Appl. Mech. Eng. 198 (2009) 1660–1672.
[32] P. Solin, K. Segeth, I. Dolezel, Higher-Order Finite Element Methods, Chapman & Hall/CRC, 2004.
[33] F. Fuentes, B. Keith, L. Demkowicz, S. Nagaraj, Orientation embedded high order shape functions for the exact sequence elements of all shapes, Comput. Math. Appl. 70 (4) (2015) 353–458.
[34] M. Rognes, R.C. Kirby, A. Logg, Efficient assembly of $H(\mathrm{div})$ and $H(\mathrm{curl})$ conforming finite elements, E-prints arXiv, arXiv:1205.3085, 2012.
[35] A. Angoshtari, A. Yavari, The weak compatibility equations of nonlinear elasticity and the insufficiency of the Hadamard jump condition for non-simply connected bodies, Contin. Mech. Thermodyn. 28 (5) (2016) 1347–1359.
[36] D. Boffi, F. Brezzi, M. Fortin, Mixed Finite Element Methods and Applications, vol. 44, Springer, 2013.
[37] J.L. Ericksen, Deformations possible in every isotropic, incompressible, perfectly elastic body, Z. Angew. Math. Phys. 5 (6) (1954) 466–489.
[38] S. Sadik, A. Yavari, Small-on-large geometric anelasticity, Proc. R. Soc. Lond. A 472 (2195) (2016).
[39] A. Ozakin, A. Yavari, A geometric theory of thermal stresses, J. Math. Phys. 51 (3) (2010) 032902.
[40] A. Yavari, A geometric theory of growth mechanics, J. Nonlinear Sci. 20 (2010) 781–830.
[41] T.J. Pence, H. Tsai, Swelling-induced microchannel formation in nonlinear elasticity, IMA J. Appl. Math. 70 (1) (2005) 173–189.
[42] A. Golgoon, S. Sadik, A. Yavari, Circumferentially-symmetric finite eigenstrains in incompressible isotropic nonlinear elastic wedges, Int. J. Non-Linear Mech. 84 (2016) 116–129.
[43] A. Golgoon, A. Yavari, On the stress field of a nonlinear elastic solid torus with a toroidal inclusion, J. Elast. 128 (1) (2017) 115–145.